INVISIBILITY AND INVERSE PROBLEMS: THEORETICAL AND COMPUTATIONAL APPROACHES

by

Ray Gabriel Abney Fiallos

A dissertation submitted to the faculty of
The University of North Carolina at Charlotte
in partial fulfillment of the requirements
for the degree of Doctor of Philosophy in
Applied Mathematics

Charlotte

2025

Approved by:

_____
Dr. Gregory Gbur

_____
Dr. Loc Nguyen

_____
Dr. Xingjie Li

_____
Dr. Taufiquar Khan

ABSTRACT

RAY GABRIEL ABNEY FIALLOS. Invisibility and Inverse Problems: Theoretical and Computational Approaches. (Under the direction of DR. GREGORY GBUR)

This dissertation presents new theoretical and computational advancements in the study of wave propagation, focusing on invisibility and inverse problems. The research is divided into three main parts, each addressing a distinct but significant challenge in mathematical physics.

Chapter 2 develops a theoretical framework for nonradiating orbital motions, a phenomenon where wave sources move within a bounded domain without emitting detectable radiation. This study extends classical results on nonradiating sources by constructing explicit time-dependent solutions that satisfy strict boundary conditions to suppress outward radiation. Using Fourier series expansions and Green's formulae, we derive families of sources that exhibit motion while remaining undetectable. Numerical simulations validate these theoretical findings, and we discuss potential experimental realizations in structured wave systems, such as surface plasmons.

Chapter 3 explores invisibility techniques for scattering problems, specifically the design of nonscattering scatterers. We analyze wave interactions with specially engineered structures that prevent scattered waves from revealing the presence of an object. We construct mathematical models demonstrating how material properties can be adjusted to achieve near-perfect invisibility. The chapter further provides computational validations illustrating the feasibility of these invisibility mechanisms in practical scenarios, with implications for the nonuniqueness of the inverse source problem and for wave-based imaging.

In Chapter 4, we shift focus to inverse problems for parabolic equations, where the goal is to reconstruct unknown coefficients using limited boundary data. We introduce a Carleman-Picard iteration method, a globally convergent algorithm that combines

Carleman estimates, quasi-reversibility techniques, and a reduced-dimensional representation to enhance stability and accuracy. Unlike traditional optimization methods that rely on initial approximations and are susceptible to local minima, the proposed approach ensures robust recovery of zero-order coefficients in parabolic partial differential equations. Numerical experiments confirm the effectiveness of this method in practical applications, including bioheat transfer modeling, geophysical exploration, and non-destructive testing.

Through rigorous mathematical derivations and extensive numerical analyses, this dissertation contributes to the broader understanding of wave manipulation, invisibility theory, and inverse problems. The results have potential applications in electromagnetic and acoustic cloaking, wave-based sensing, medical imaging, and material characterization, advancing the theoretical foundations and computational tools for solving complex wave phenomena.

DEDICATION

I would like to dedicate this dissertation to my parents, Eloida and David Abney; and also to Ivan, to Mimi and Mia, and to all of the other members of my family. I would also like to dedicate this dissertation to my friends, especially my Grigg Hall friends among others. And I would like to dedicate this to my teachers, who built me up.

ACKNOWLEDGEMENTS

I would like to acknowledge Drs. Gbur and Nguyen, my doctoral advisors, for all of their help in helping me get this dissertation done. I would like to acknowledge the help of the Department of Mathematics and Statistics and the Department of Physics and Optical Science for their teaching assistantships that supported me. I would like to acknowledge the support from Dr. Nguyen's NSF grant DMS-2208159 and FRG at UNC Charlotte, Fund No. 111272. And I also would like to acknowledge Drs. McGoff, Safronov, Molchanov, Chen, and Vainberg for their help in helping me prepare for both parts of the qualifying exam.

TABLE OF CONTENTS

PREFACE

In this dissertation, I discuss invisibility and inverse problems. I discuss topics that I know would interest the militaries of the various imperialist powers of this world. However, I would like to make it absolutely clear to the reader that the goal of this dissertation is to explore invisibility and inverse problems in the general. Nothing written in this dissertation was written with the intention of helping any military anywhere.

However, if I ever do any sort of work with any military of any bourgeois country, it may be in something in inverse problems along the lines of helping develop math to clear mines and unexploded ordinance. Among other countries, France, Laos, and, especially these days, Palestine still have a big problem with unexploded ordinance; and I would be willing to work with anyone who wants to help clean up hidden explosives in these countries or anywhere else. Otherwise, if the militaries of the imperialist powers of this world want scientists to help them dominate over other countries, they would be wasting their time looking to me because I'm not the one.

My job is to be a scientist for the good of all mankind. My job is to do neat things and discover neat things in mathematics and in physics. To any students—mine or otherwise—considering a career in mathematics or the sciences in general, don't compromise your morals to please any teacher or employer, or to advance your career.

—RGAF

CHAPTER 1: INTRODUCTION

This dissertation is structured into three main parts:

1. **Invisibility for Sources**: The first part explores invisibility in the context of wave-like equations, focusing on the design of nonradiating sources that do not emit detectable waves. By ensuring that the emitted fields remain confined and do not propagate outward, we achieve effective source invisibility.

2. **Invisibility for Objects**: The second part investigates techniques to render objects undetectable by constructing nonscattering scatterers that prevent wave reflections, thereby concealing the presence of an object.

3. **Inverse Problems for Parabolic Equations**: The third part shifts focus to inverse problems, particularly in the setting of parabolic equations. Here, we develop mathematical and computational techniques to detect and reconstruct hidden objects from limited measurements.

While the first two parts seek to suppress wave interactions to achieve invisibility, the third part takes the opposite goal, aiming to recover missing information from external observations. The interplay between these two areas highlights fundamental challenges in mathematical physics. This dissertation provides both theoretical insights and computational methodologies to advance the study of invisibility and inverse problems.

1.1 Nonradiating Orbital Motions

The study of nonradiating sources has been a long-standing topic in wave physics, particularly in electromagnetics, acoustics, and quantum mechanics. In the early

1900's, physicists concerned themselves with, among other topics, the structure of an atom. What physicists wanted to know in these days was how electrons could orbit and not emit any radiation. Thus, in 1910, Paul Ehrenfest published [23]. In his paper, he said that although point charges must radiate when accelerating, an extended distribution of electric charge could be constructed that could oscillate and still not radiate.

Some years later, in his 1933 paper [80], George Schott showed how it is possible for a uniformly charged shell of radius a to move about in an arbitrary, periodic orbit of period T and not radiate, where a and T are related by the equation

$$a = \frac{mcT}{2}, \tag{1.1}$$

where m is an integer and c is the speed of light. However, due to equation (1.1), the orbit of this shell will be very small, well within the radius of the shell. Thus, Schott's shell's "orbit" will be more of a wobbling sort of motion rather than anything similar to the moon going around the earth.

Schott went on to write more papers concerning charged spheres that spin or orbit, like [81, 82, 83, 84]. From this later work, the most significant result was that a charged sphere might also self-oscillate without external force. From this result, Bohm and Weinstein in 1948 in [10] came up with more classes of nonradiating distributions. And Goedecke in 1964 in [31] developed a more general theory of radiationless motions. And finally, the 1989 paper [26] written by Gamliel, Kim, Nachman, and Wolf gave conditions whereby a source is a nonradiating source. The result of [26] is instrumental to our work and results in Chapters 2 and 3.

The study of nonradiating sources is important for a couple of reasons, among others: First, as Friedlander, Devaney, Wolf, Bleistein, and Cohen showed in their work back in the 70's (see [25] by Friedlander, [22] by Devaney and Wolf, and [9] by Bleistein and Cohen), there is a connection between monochromatic nonradiating sources and

the nonuniqueness of the inverse source problem, which is the type of inverse problem where one wants to determine the structure of a source from its radiation pattern. Obviously, if nonradiating sources do not radiate, it is impossible to determine the properties of any particular nonradiating source from radiation measurements. With this said, the existence of nonradiating sources implies the nonuniqueness of the inverse source problem. Secondly, nonradiating sources can exist in a variety of wave systems, from gravitational wave systems [62] to vibrating strings [66]. In fact, [36] considers nonradiating anapoles a candidate for dark matter. So nonradiating sources may answer some very fundamental questions about our universe.

This dissertation contributes to this evolving field of nonradiating sources by establishing a theoretical framework for nonradiating orbital motions, a phenomenon where wave sources move within a bounded region without emitting detectable radiation. While conventional wave sources typically generate propagating waves extending beyond their origin, we demonstrate that carefully designed sources can remain nonradiating, ensuring that no energy escapes beyond their confined domain. This has direct implications for wave-based cloaking.

Our approach begins with the mathematical formulation of nonradiating sources within the framework of wave-like equations. We construct time-dependent solutions that satisfy strict boundary conditions, effectively preventing outward radiation. Using analytical techniques such as Fourier series expansions and Green's formulae, we derive explicit examples of nonradiating orbiting sources, where wave energy circulates within an annular region without radiating externally.

To validate our theoretical findings, we perform numerical simulations to compute the resulting fields and confirm their nonradiating nature. These simulations illustrate that such sources can be systematically designed to follow predefined orbital trajectories while maintaining their invisibility. Furthermore, we discuss potential experimental realizations, particularly in surface wave systems, where structured light

beams could be utilized to create similar nonradiating excitations.

1.2 Invisible Objects: Theoretical Models and Numerical Validation

An object is invisible if it does not radiate or scatter waves, see [28, 30, 38]. This effect is achieved by designing structures that control how waves interact with an object, preventing them from scattering in a way that would reveal its presence. The idea of invisibility has been a subject of interest for centuries, but it was only in recent decades that rigorous mathematical and physical frameworks were developed to realize invisibility in practical settings.

In 1975, Milton Kerker introduced the concept of nonscattering scatterers in his pioneering work [40], describing the first objects that could be considered truly "invisible" in the sense that they do not scatter incident light. Kerker examined specific ellipsoidal core-shell structures, where the core possessed a higher refractive index than the surrounding medium, while the shell had a lower refractive index than the background. These objects were assumed to be subwavelength-sized, satisfying the Rayleigh scattering criterion, ensuring that their interaction with light was governed primarily by dipole radiation.

A major breakthrough in cloaking, a form of invisibility, emerged with the advent of transformation optics, introduced by Pendry, Schurig, and Smith in their influential paper on electromagnetic cloaking [77]. They demonstrated that by designing metamaterials with spatially varying permittivity and permeability, light waves could be guided around an object as if it were absent, effectively rendering it invisible to an external observer. This approach was inspired by earlier theoretical work by Greenleaf et al. [32], which explored invisibility in the context of conductivity equations.

Simultaneously, an alternative cloaking method known as scattering cancellation was proposed by Alù and Engheta [5]. Their approach utilized plasmonic materials to induce destructive interference, thereby eliminating scattered waves and achieving invisibility for specific frequencies. Unlike transformation optics, which demands

intricate material engineering, scattering cancellation offers a more straightforward and practical means of achieving cloaking in certain applications.

Further developments include multifrequency cloaking [63, 65, 67], cloaking for acoustic and water waves [19, 90], and active cloaking [33, 76], where external sources or metamaterials are used to cancel scattered waves dynamically. These ideas have been extended to various wave systems, including elastodynamics, acoustics, and quantum mechanics.

While cloaking technologies continue to advance, challenges remain, such as bandwidth limitations, material losses, and the difficulty of achieving perfect cloaking for all frequencies and angles. Nonetheless, the field has provided deep insights into wave manipulation and continues to inspire applications in biomedical imaging and wave-based computing.

Of course, while the big topic in invisibility these days seems to be about cloaking, which is why we discuss cloaking so much in this section, the second part of this dissertation concerns invisibility more generally. In the second part of this dissertation, we explore the theoretical and numerical construction of objects that are invisible from multiple directions, extending previous work on nonscattering scatterers. While perfect invisibility from all directions is theoretically impossible, as established by Habashy and Wolf [88], it is feasible to design objects that are undetectable from a finite number of prescribed directions. Our work builds on the seminal results of Devaney [21], who showed how to construct scattering potentials that render an object invisible along specific directions, and Gbur [29], who further refined these techniques.

We develop a mathematical framework using what we refer to in this dissertation as the "Devaney operator," which allows us to systematically generate scattering potentials for objects that are invisible from multiple directions. By applying this operator iteratively, we construct objects with an increasing number of invisible directions. Our study confirms that as the number of directions of invisibility increases,

the maximum power radiated by the scattered field decreases, effectively making the object practically invisible in most cases.

To validate our theoretical findings, we conduct numerical simulations for six different objects whose scattering potentials are based on a polynomial and for another six different objects whose scattering potentials are based on the bump function. Each object is designed to be invisible from a different number of prescribed directions. Using Green's formula techniques, we compute the scattered fields and analyze the power radiated as a function of the incident wave direction. Our results show that objects with more invisible directions radiate significantly less power, reinforcing the effectiveness of our approach.

Our study on nonscattering scatterers contributes to the broader study of wave manipulation and inverse scattering problems, offering insights into the controlled design of invisible structures. The findings have potential applications in the nonuniqueness of the inverse scattering problem and in wave-based imaging, where selective invisibility can be strategically exploited.

1.3 Inverse Problems for Parabolic Partial Differential Equations

This dissertation explores inverse problems alongside invisibility, highlighting their conceptual opposition. While in Chapters 2 and 3 we concern ourselves with constructing objects that cannot be seen, in Chapter 4 we do the opposite and seek to reconstruct hidden information from observed data. Inverse problems for partial differential equations (PDEs) arise in diverse scientific and engineering fields, including medical imaging, geophysics, non-destructive testing, and remote sensing. Unlike direct problems, where the governing PDE and input data are known, inverse problems involve determining unknown parameters or unknown sources based on limited or indirect observations.

The investigation of coefficient inverse problems for parabolic PDEs has a rich history, deeply rooted in mathematical physics. Hadamard [34] introduced the concept

of well-posedness, highlighting that many inverse problems are inherently ill-posed, meaning that solutions may not exist, may lack uniqueness, or may be highly sensitive to small variations in data. To address these challenges, Tikhonov [86] developed regularization techniques, leading to the widely adopted Tikhonov regularization method, which remains a fundamental approach for numerically stabilizing and solving inverse problems. However, a significant drawback of the methods based on Tikhonov regularization is the presence of multiple local minima in the Tikhonov cost functional, which can cause solutions to become trapped rather than converging to the global minimizer. To address this issue, recent research has focused on globally convergent methods that eliminate the need for an initial approximation, thereby reducing the risk associated with local minima. Three prominent globally convergent approaches include:

1. the Carleman convexification method, first introduced in [49] by Klibanov and Ioussoupova;

2. the Carleman contraction principle method, first developed in [57] by Le and Nguyen;

3. the Carleman-Newton method, first proposed in [60] by Le, Nguyen, and Tran.

While each of these methods is effective, this dissertation adopts the second approach due to its lower computational cost and its simpler implementation.

Building on these advancements, this dissertation extends the Carleman contraction principle method to address an inverse coefficient problem in parabolic equations with limited boundary data. Specifically, we focus on reconstructing the zero-order coefficient in a parabolic equation, a critical task in applications such as bioheat transfer, geophysics, and non-destructive testing.

To extend the applicability of the Carleman contraction principle method [57] to cases with limited data, we incorporate the reduced dimensional approach, originally

introduced in [35]. This approach reformulates the inverse problem into a system of one-dimensional nonlinear equations, utilizing the polynomial-exponential basis expansion introduced in [48]. This transformation not only simplifies the problem but also improves computational efficiency. Since we do not explicitly construct a contraction map in our approach, we refer to this modified method as the Carleman-Picard method to distinguish it from the original version in [57].

We provide a rigorous proof of convergence for the Carleman-Picard method, further establishing the reliability and effectiveness of our iterative scheme in accurately reconstructing the unknown coefficient.

To validate our approach, we perform numerical simulations to evaluate its accuracy and robustness, even in the presence of noisy data. The results demonstrate that the Carleman-Picard iteration successfully reconstructs the zero-order coefficient in parabolic equations using only partial boundary data, making it a practical and computationally efficient solution for real-world applications. This study advances the broader field of inverse problems for PDEs by introducing a globally convergent and stable methodology for solving nonlinear inverse problems.

CHAPTER 2: NONRADIATING ORBITAL MOTIONS

The material of this chapter comes from [3], an article based on [2] that was published in May 2023 in *Physical Review A*. In this chapter, we discuss nonradiating orbital motions. We show how it is possible to create nonradiating sources that can orbit about the center of an annulus and be whatever shape we want them to be, and we also discuss about how one could possibly create an experimental setup demonstrating nonradiating orbital motions.

2.1 Introduction

When a driving force is applied to a closed region, one would expect waves to propagate away from the closed region where the driving force is being applied. However, this does not necessarily have to happen. It is possible for a driving force to be applied to a closed region and for the resulting waves to stay within the closed region. When this happens, the driving force becomes a nonradiating source, and the field created by the driving force becomes what is known as a nonpropagating excitation.

A major inspiration for the work of this chapter and of the works [2, 3] is the article [66], written by Dylan Moses, Choon How Gan, and Gregory Gbur, which discusses how to create nonpropagating excitations in 1D. In this chapter, we create a nonpropagating excitation in 2D that is the product of two other functions created according to the results of [66]. And then we put this nonpropagating excitation through the wave equation to determine the corresponding nonradiating source. The field and source are both time dependent and we make them orbit about the center of an annulus.

The work of this chapter is important for a few reasons. In this chapter, we

demonstrate how it is theoretically possible to construct 2D nonradiating sources that can orbit about an annulus and be whatever shape we want them to be, and we discuss one way one could create an experimental setup demonstrating nonradiating sources that orbit. We consider 2D nonradiating orbiting sources because it is mathematically easier to consider than 3D nonradiating orbiting sources. In particular, the 2D case is ideal for studying nonradiating sources experimentally. For instance, it might be possible to excite surface waves on a metal plate. And finally, while 1D and 3D nonradiating sources have been studied, 2D nonradiating sources have not been studied very much, with the exceptions of [2, 27].

2.2 An Important Theorem Concerning Nonradiating Sources

Before we proceed, we must introduce a theorem that is not only important for the material of this chapter, but also for that of Chapter 3. This theorem comes from [26], where its proof can also be found; and it concerns the conditions that must be met in order for us to have a nonradiating source.

Theorem 2.2.1. *Let $q(\mathbf{r})$ be a bounded, nonradiating source distribution of finite support, and let $u(\mathbf{r})$ be the field that $q(\mathbf{r})$ generates. Then $u(\mathbf{r})$ and $q(\mathbf{r})$ are related by the inhomogeneous Helmholtz equation*

$$(\nabla^2 + k^2)u(\mathbf{r}) = -4\pi q(\mathbf{r}), \tag{2.1}$$

with the boundary conditions

$$u(\mathbf{r}) = \partial_{\mathbf{n}} u(\mathbf{r}) = 0 \text{ for } \mathbf{r} \in \partial D, \tag{2.2}$$

where $k > 0$ is a constant, D is the domain of our source, ∂D is the boundary of D, and $\partial_{\mathbf{n}}$ denotes differentiation along the outward normal, where $\mathbf{n}$ is the unit normal vector pointing away from ∂D.

2.3 Theory of Nonradiating Orbital Motions

Our nonradiating sources $Q(\mathbf{r},t)$ and our fields $U(\mathbf{r},t)$ are related by the wave equation

$$\nabla^2 U(\mathbf{r},t) - \frac{1}{c^2}U_{tt}(\mathbf{r},t) = -4\pi Q(\mathbf{r},t), \tag{2.3}$$

where c is the speed of our wave and $\mathbf{r} = (r,\theta) \in \mathbb{R}^2$. We start off with *monochromatic* fields and sources. We have our field $U(\mathbf{r},t) = u(\mathbf{r},\omega)e^{-i\omega t}$, where $u(\mathbf{r},\omega)$ satisfies the Helmholtz equation

$$\nabla^2 u(\mathbf{r},\omega) + k^2 u(\mathbf{r},\omega) = -4\pi q(\mathbf{r},\omega), \tag{2.4}$$

where $k = \omega/c$ is our wave number. Naturally, our nonradiating source will be of the form $Q(\mathbf{r},t) = q(\mathbf{r},\omega)e^{-i\omega t}$.

Now, we want our nonradiating source, and thus our field, to orbit the center of an annulus of inner radius a and outer radius b. And we want to restrict our nonradiating source to a sector of this annulus bounded by the angles ϕ and ψ. Thus, our nonradiating source is restricted to the set

$$S = \{(r,\theta) : a \le r \le b \text{ and } \phi \le \theta \le \psi\}. \tag{2.5}$$

From Theorem 2.2.1, in order for $Q(\mathbf{r},t)$ to be a nonradiating source, the field $U(\mathbf{r},t)$ must satisfy a pair of boundary conditions. Namely, for a nonradiating source restricted to a region S, $u(\mathbf{r},\omega)$ must satisfy the boundary conditions

$$u(\mathbf{r},\omega) = \partial_{\mathbf{n}} u(\mathbf{r},\omega) = 0 \text{ for all } \mathbf{r} \in \partial S. \tag{2.6}$$

Thus, from Theorem 2.2.1, $u(\mathbf{r},\omega)$ must satisfy the boundary conditions

$$u(a,\theta,\omega) = u(b,\theta,\omega) = 0, \qquad u_r(a,\theta,\omega) = u_r(b,\theta,\omega) = 0, \tag{2.7}$$

$$u(r,\phi,\omega) = u(r,\psi,\omega) = 0, \qquad u_\theta(r,\phi,\omega) = u_\theta(r,\psi,\omega) = 0. \tag{2.8}$$

One way to create a $u(\mathbf{r},\omega)$ that satisfies our boundary conditions is to make $u(\mathbf{r},\omega)$

the product of two functions. Thus, we start off with $u(\mathbf{r}) = v(r)w(\theta)$. Thus,

$$v(r) = \begin{cases} c_m(r-K)^m + c_{m+2}(r-K)^{m+2} + c_{m+4}(r-K)^{m+4} & r \in [a,b] \\ 0 & \text{otherwise,} \end{cases} \tag{2.9}$$

where $m \in \mathbb{N}_0$, where $K = (a+b)/2$, and where

$$c_m = c_{m+4}\frac{(a-b)^4}{16}, \quad c_{m+2} = -c_{m+4}\frac{(a-b)^2}{2}, \quad c_{m+4} = 1. \tag{2.10}$$

v satisfies the boundary conditions

$$v(a) = v(b) = 0, \quad v'(a) = v'(b) = 0, \tag{2.11}$$

where the primes indicate derivatives with respect to r. In our calculations, we take $m = 0, 2$. And similarly,

$$w(\theta) = \begin{cases} d_n(\theta-H)^n + d_{n+2}(\theta-H)^{n+2} + d_{n+4}(\theta-H)^{n+4} & \theta \in [\phi,\psi] \\ 0 & \text{otherwise,} \end{cases} \tag{2.12}$$

where $n \in \mathbb{N}_0$, where $H = (\phi+\psi)/2$, and where

$$d_n = d_{n+4}\frac{(\phi-\psi)^4}{16}, \quad d_{n+2} = -d_{n+4}\frac{(\phi-\psi)^2}{2}, \quad d_{n+4} = 1. \tag{2.13}$$

And w satisfies the boundary conditions

$$w(\phi) = w(\psi) = 0, \quad w'(\phi) = w'(\psi) = 0, \tag{2.14}$$

where the primes indicate derivatives with respect to θ. In our calculations, we take $n = 0, 2$. The inspiration for these two functions $v(r)$ and $w(\theta)$ comes from [66].

Taking the Fourier series of $w(\theta)$, we get

$$w^F(\theta) = \sum_{p=-\infty}^{\infty} \left(\frac{1}{2\pi} \int_{\phi}^{\psi} w(\theta') e^{-ip\theta'} d\theta' \right) e^{ip\theta}. \tag{2.15}$$

Now, to have a nonradiating source that orbits, we need to make $w^F(\theta)$ a function of

both θ and t. Thus, replacing θ with $\theta - \omega_0 t$ in the equation above, we get

$$\begin{aligned} w^{TF}(\theta, t) &= \sum_{p=-\infty}^{\infty} \left(\frac{1}{2\pi} \int_{\phi}^{\psi} w(\theta') e^{-ip\theta'} d\theta' \right) e^{ip(\theta - \omega_0 t)} \\ &= \sum_{p=-\infty}^{\infty} \left[\left(\frac{1}{2\pi} \int_{\phi}^{\psi} w(\theta') e^{-ip\theta'} d\theta' \right) e^{ip\theta} \right] e^{-ip\omega_0 t}, \end{aligned} \tag{2.16}$$

the time-dependent Fourier series of $w(\theta)$. Thus, we have our field $U(\mathbf{r}, t) = v(r) w^{TF}(\theta, t)$. It orbits the center of our annulus at an angular frequency ω_0 with a period $T = 2\pi/\omega_0$.

We have that

$$\begin{aligned} U(\mathbf{r}, t) &= v(r) w^{TF}(\theta, t) \\ &= \sum_{p=-\infty}^{\infty} \left[v(r) \left(\frac{1}{2\pi} \int_{\phi}^{\psi} w(\theta') e^{-ip\theta'} d\theta' \right) e^{ip\theta} \right] e^{-ip\omega_0 t} \\ &= \sum_{p=-\infty}^{\infty} u(\mathbf{r}, p\omega_0) e^{-ip\omega_0 t}. \end{aligned} \tag{2.17}$$

Thus, our field $U(\mathbf{r}, t)$ is a *multifrequency* field with frequencies $p\omega_0$, where $p \in \mathbb{Z}$; our field $U(\mathbf{r}, t)$ is the sum of many *monochromatic* fields of the form $u(\mathbf{r}, \omega) e^{-i\omega t}$. Every term of our summation in (2.17) satisfies the boundary conditions needed for us to have a nonradiating source. And when we put $U(\mathbf{r}, t)$ through the wave equation, we get our nonradiating source $Q(\mathbf{r}, t)$.

2.4 Examples and Observations

Here, we consider a few examples. Now, in all of our examples, except where otherwise stated, $c = 1.5 \times 10^{10}$ cm s^{-1}, $a = 2$ cm and $b = 3$ cm, and $m = 0, 2$ and $n = 0, 2$. Now, when our nonradiating source moves about our annulus, we want it to have a speed $v = c/1000$ at the outer edge of our annulus. The circumference of our annulus is $C = 2\pi b$. Therefore, our angular frequency is

$$\omega_0 = \frac{c}{1000b}. \tag{2.18}$$

With $b = 3$ cm, our angular frequency usually amounts to 5×10^6 rad s^{-1}.

In our simulations, we first analytically calculate the fields $U(\mathbf{r},t) = v(r)\Re[w^{TF}(\theta,t)]$. The function $w^{TF}(\theta,t)$ is complex-valued. So we need to take the real part of $w^{TF}(\theta,t)$ to make $U(\mathbf{r},t)$ real-valued. The wave equation in polar coordinates is

$$Q(\mathbf{r},t) = -\frac{1}{4\pi}\left[wv_{rr}^{TF} + \frac{1}{r}v_r w^{TF} + \frac{1}{r^2}vw_{\theta\theta}^{TF} - \frac{1}{c^2}vw_{tt}^{TF}\right]. \tag{2.19}$$

We put our field $U(\mathbf{r},t)$ through our wave equation to get our nonradiating source $Q(\mathbf{r},t)$. Thus, we get the graphs in Figures 2.1 and 2.2.

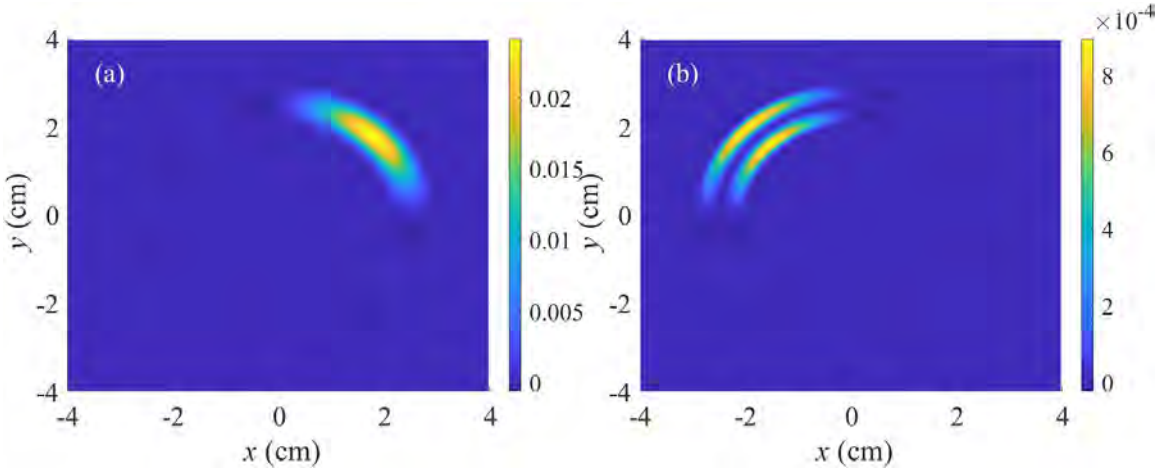

Figure 2.1: Two fields $U(\mathbf{r},t)$. In (a), we have $m = n = 0$ and $t = 0$. In (b), we have $m = 2$, $n = 0$, and $t = T/4$, where T is our period. In both figures $\phi = 0$ and $\psi = \pi/2$.

To confirm that our functions $Q(\mathbf{r},t)$ are, in fact, nonradiating sources, we can calculate $u(\mathbf{r},\omega)$ from $q(\mathbf{r},\omega)$, frequency by frequency, using a Green's formula

$$u(\mathbf{r},\omega) = \int_D q(\mathbf{r}',\omega)G(|\mathbf{r}-\mathbf{r}'|,\omega)\,d^2\mathbf{r}', \tag{2.20}$$

where D is the domain of integration and

$$G(|\mathbf{r}-\mathbf{r}'|,\omega) = i\pi H_0^{(1)}(k|\mathbf{r}-\mathbf{r}'|), \tag{2.21}$$

where $H_0^{(1)}$ is the Hankel function of the first kind.

When $p = 0$, we get $G(|\mathbf{r}-\mathbf{r}'|,0) = -2\ln(|\mathbf{r}-\mathbf{r}'|)$, the Green's function for Poisson's

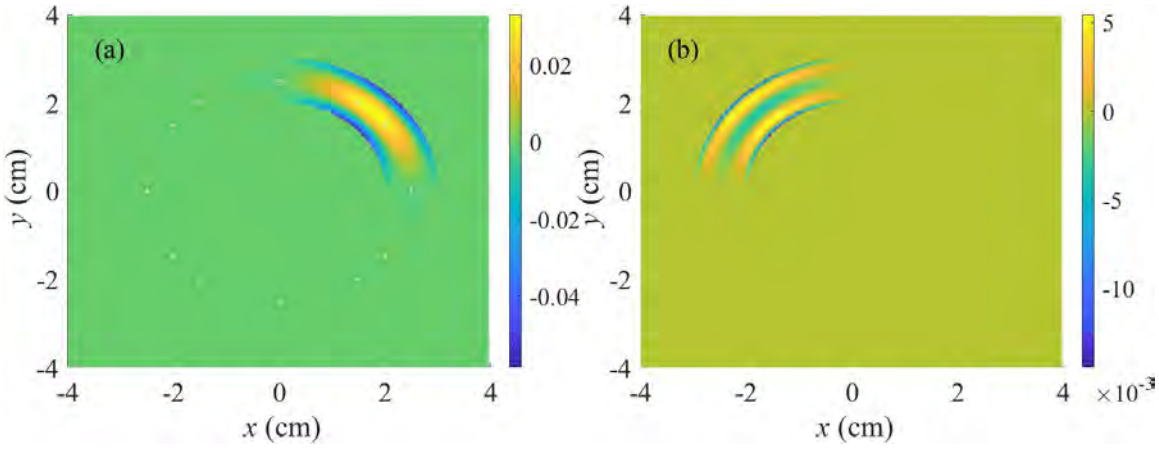

Figure 2.2: Two nonradiating sources $Q(\mathbf{r}, t)$. Figures (a) and (b) correspond with (a) and (b) of Figure 2.1.

equation, which blows up whenever $|\mathbf{r} - \mathbf{r}'| = 0$. Thus, to compute $u(\mathbf{r}, 0)$, we use a Fourier transform approach. Thus,

$$u(\mathbf{r}, 0) = 4\pi \int_D \frac{\tilde{q}(\mathbf{K}, 0)}{K^2 + i\epsilon} e^{i\mathbf{K}\cdot\mathbf{r}} d^2\mathbf{K}. \tag{2.22}$$

This comes from the direct Fourier transform of the Poisson equation. ϵ is a small ($\sim 10^{-6}$) regularization parameter. The Fourier transform of q and the inverse Fourier transform can be done with fast Fourier transforms. Altogether,

$$\begin{aligned} U(\mathbf{r}, t) = 4\pi &\int_D \frac{\tilde{q}(\mathbf{K}, 0)}{K^2 + i\epsilon} e^{i\mathbf{K}\cdot\mathbf{r}} d^2\mathbf{K} \\ &+ \sum_{p\neq 0} e^{-ip\omega_0 t} \int_D q(\mathbf{r}', p\omega_0) G(|\mathbf{r} - \mathbf{r}'|, p\omega_0)\, d^2\mathbf{r}'. \end{aligned} \tag{2.23}$$

We calculate this version of $U(\mathbf{r}, t)$ numerically. In Figure 2.3, using equation (2.23) with the domain of integration $D = [-4, 4] \times [-4, 4]$, we reconstruct the $U(\mathbf{r}, t)$ of Figure 2.1b.

Finally, since $U(\mathbf{r}, t)$ only has to satisfy certain boundary conditions (which do not depend on the physical size of the system) for $Q(\mathbf{r}, t)$ to be nonradiating, we can have our nonradiating source be as large or as small as we want, as Figure 2.4 illustrates.

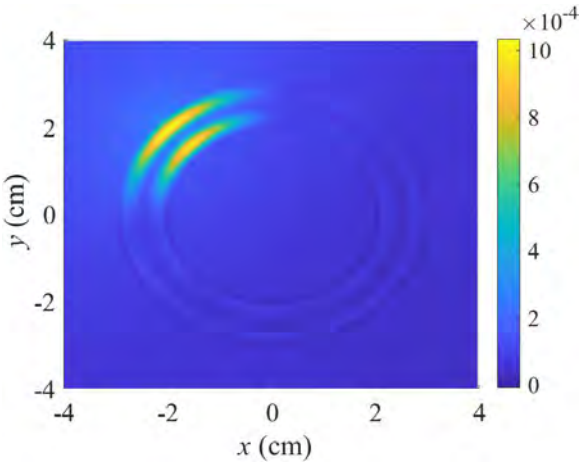

Figure 2.3: $U(\mathbf{r}, t)$ at $t = T/4$ reconstructed using the Green's formulas and the Fourier transform. Our graph here agrees very well with the graph of Figure 2.1b.

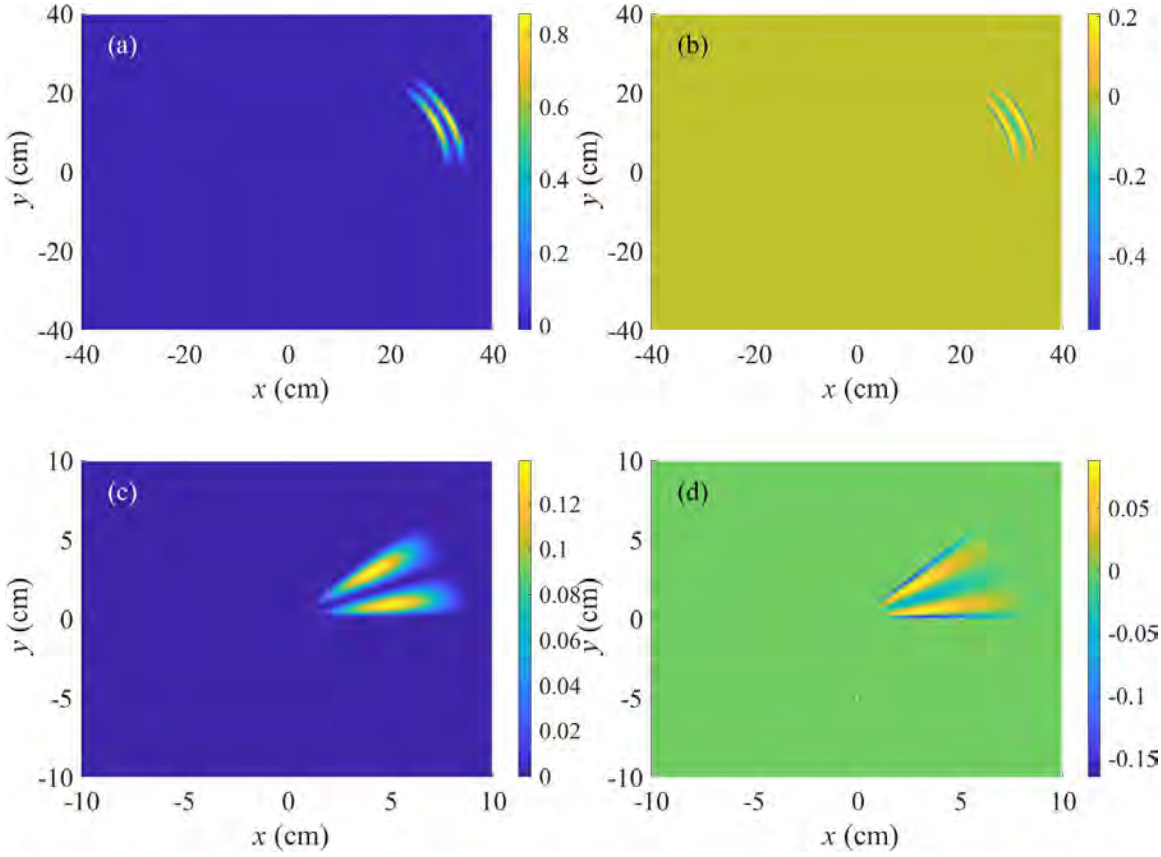

Figure 2.4: In (a) and (b), we have $m = 2$, $a = 30$ cm, $b = 35$ cm, $\phi = 0$, $\psi = \pi/4$, and $t = 0$. In (c) and (d), we have $m = 0$, $n = 2$, $a = 1$ cm, $b = 9$ cm, $\phi = 0$, $\psi = \pi/4$, and $t = 0$. The left column represents fields and the right column represents sources.

2.5 Nonradiating Orbital Motions and Surface Waves

Up to this point, there have been very few experimental demonstrations of nonradiating sources. Nonradiating anapoles are one sort of nonradiating source where the fields of an electric dipole and a toroidal dipole destructively interfere. There have been some experiments done with nonradiating anapoles, as outlined in [24] and [64]. But these nonradiating anapoles are not the same kind of nonradiating sources described in our paper. What we would like to see is if it is possible to create an experimental demonstration that results in the same sort of nonradiating sources described in our paper.

Since we are concerned with two-dimensional nonradiating sources, we could use surface waves, like surface plasmons, to demonstrate nonradiating sources. In the Otto or Kretschmann configuration, an evanescent wave is used to excite a metal surface, producing propagating surface plasmons. We could have a structured beam of light that matches one of our nonradiating sources to generate an evanescent spot on a metal surface. Our structured light beam would be a nonradiating source if the surface plasmons stay in the area that is being excited by the structured light beam. And our structured light beam would be an *orbiting* nonradiating source if we also move it across the surface in a circle over and over.

Let ω_c be the carrier frequency of our structured beam of light. Then the field resulting from our nonradiating source can be written as

$$U(\mathbf{r}, t) = U_0(\mathbf{r}, t)\cos(\omega_c t), \tag{2.24}$$

where $U_0(\mathbf{r}, t)$ is a field of the kind of nonradiating source previously described that orbits with a frequency of ω_0. When we substitute equation (2.24) into equation

(2.19), we get

$$Q(\mathbf{r},t) = Q_0(\mathbf{r},t)\cos(\omega_c t) - \frac{1}{4\pi}\frac{\omega_c^2}{c^2}U_0(\mathbf{r},t)\cos(\omega_c t) + \frac{1}{4\pi}\frac{2\omega_c}{c^2}\partial_t U_0(\mathbf{r},t)\sin(\omega_c t), \tag{2.25}$$

where $Q_0(\mathbf{r},t)$ is the result of putting $U_0(\mathbf{r},t)$ through the wave equation. And we consider two simulations, one with a carrier frequency of $\omega_c = 600 \times 10^6$ rad s^{-1} and one with $\omega_c = 600 \times 10^{12}$ rad s^{-1}. In both cases, we have $m = n = 2$.

For the low frequency case with $\omega_c = 600 \times 10^6$ rad s^{-1}, our carrier frequency is comparable to the orbital frequency $\omega_0 = 5 \times 10^6$ rad s^{-1}. In our simulation, we plot the square of our field $I(\mathbf{r},t) = |U(\mathbf{r},t)|^2$ and the square of our source $P(\mathbf{r},t) = |Q(\mathbf{r},t)|^2$ at $t = 0$. In our simulation, we find that the last two terms of equation (2.25) contribute very little to $Q(\mathbf{r},t)$, which indicates that we could just have

$$Q(\mathbf{r},t) \approx Q_0(\mathbf{r},t)\cos(\omega_c t). \tag{2.26}$$

Thus, in our low frequency case, as our field and source go about the center of our annulus, they flash on and off. Figure 2.5 shows the results of our low frequency case.

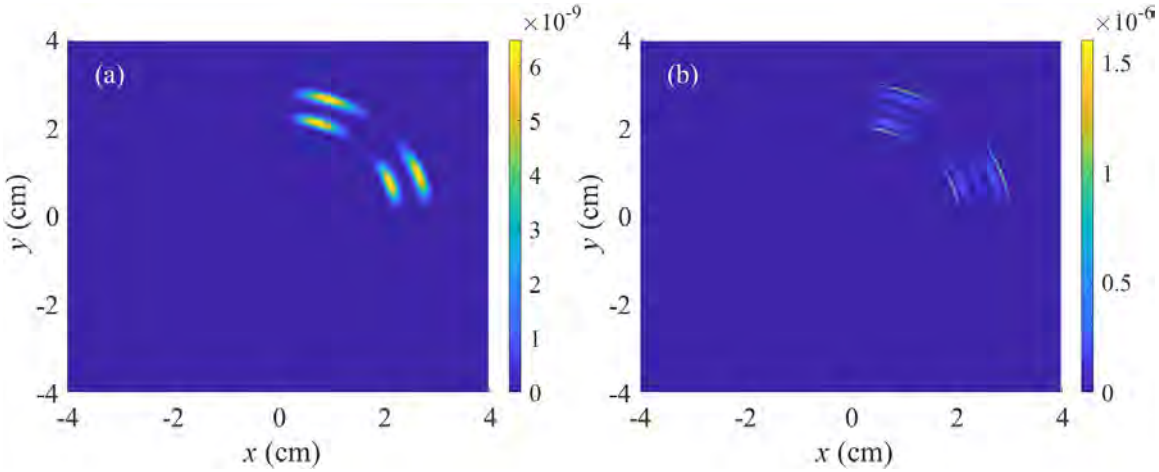

Figure 2.5: The results of our low frequency simulation. In (a) we have the plot of the square of our field $I(\mathbf{r},t)$, and in (b) we have the plot of the square of our source $P(\mathbf{r},t)$.

For the high frequency case with $\omega_c = 600 \times 10^{12}$ rad s^{-1}, our carrier frequency is about in the range of visible light. Since experiments will only measure the average over many cycles of the carrier frequency, in this simulation, we calculate the cycle averages of $U(\mathbf{r}, t)$ and $Q(\mathbf{r}, t)$. For a period of $T = 2\pi/\omega_c$ and two functions $A(t)$ and $B(t)$, the cycle average of $A(t)$ and $B(t)$ is

$$\langle A(t)B(t)\rangle = \frac{1}{T}\int_0^T A(t)B(t)\,dt. \tag{2.27}$$

Thus, we calculate and plot the cycle averages

$$\begin{aligned}\langle I(\mathbf{r},t)\rangle &= \langle |U(\mathbf{r},t)|^2\rangle \\ &= \frac{1}{T}\int_0^T |U(\mathbf{r},t)|^2\,dt \\ &= \frac{1}{T}|U_0(\mathbf{r},t)|^2\int_0^T \cos^2(\omega_c t)\,dt \\ &= \frac{1}{2}|U_0(\mathbf{r},t)|^2,\end{aligned} \tag{2.28}$$

and

$$\begin{aligned}\langle P(\mathbf{r},t)\rangle &= \langle |Q(\mathbf{r},t)|^2\rangle \\ &= \frac{1}{T}\int_0^T |Q(\mathbf{r},t)|^2\,dt \\ &= \frac{1}{T}\int_0^T \left(Q_0(\mathbf{r},t)\cos(\omega_c t) - \frac{1}{4\pi}\frac{\omega_c^2}{c^2}U_0(\mathbf{r},t)\cos(\omega_c t)\right. \\ &\quad \left. + \frac{1}{4\pi}\frac{2\omega_c}{c^2}\partial_t U_0(\mathbf{r},t)\sin(\omega_c t)\right)^2 dt \\ &= \frac{1}{2}\left[Q_0(\mathbf{r},t) - \frac{1}{4\pi}\frac{\omega_c^2}{c^2}U_0(\mathbf{r},t)\right]^2 + \frac{1}{2}\left[\frac{1}{4\pi}\frac{2\omega_c}{c^2}\partial_t U_0(\mathbf{r},t)\right]^2.\end{aligned} \tag{2.29}$$

And in Figure 2.6, we see the results of our high frequency simulation.

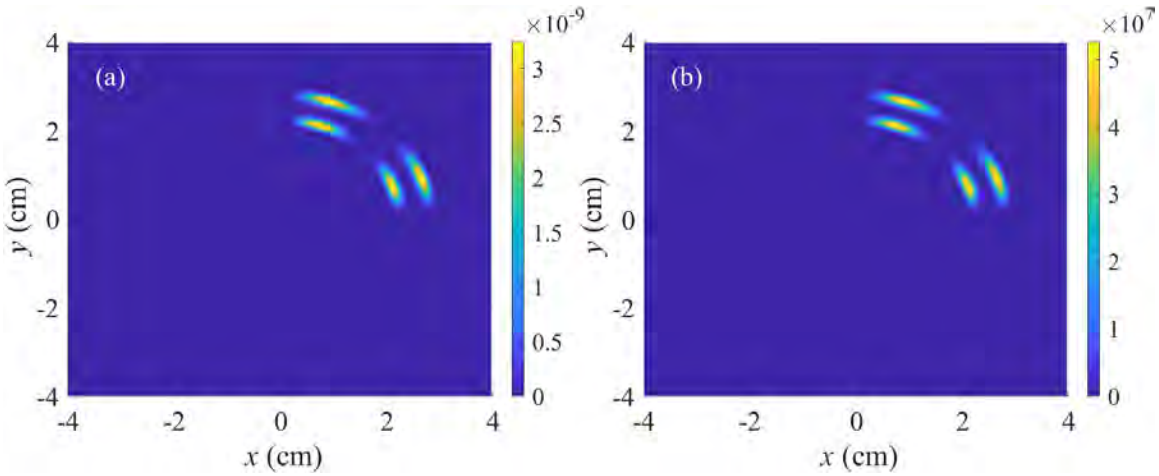

Figure 2.6: The results of our high frequency simulation. In (a) we have the plot of $\langle I(\mathbf{r},t)\rangle$, and in (b) we have the plot of $\langle P(\mathbf{r},t)\rangle$.

2.6 Conclusions

Thus, we have shown in this chapter how it is at least theoretically possible to construct nonradiating sources in 2D that can orbit, and that we can make these nonradiating sources to be of whatever shape and size we want them to be.

CHAPTER 3: CONSTRUCTION OF OBJECTS INVISIBLE FROM MULTIPLE DIRECTIONS

According to [88], it is impossible to create an object that is totally invisible from every direction, even in theory. However, it is at least theoretically possible to create objects that are invisible from a finite number of directions, and that is what we do in this chapter. The principal result of this chapter is that, the more directions of invisibility our objects have, the less power their scattered fields are able to radiate. Thus, we can create objects that are at least *practically* invisible from every direction.

3.1 Introduction

The inspiration for the material of this chapter comes from three papers: A. J. Devaney's 1978 paper [21], Emil Wolf and Tarek Habashy's 1993 paper [88], and Gregory Gbur's 2015 paper [29].

In [21], Devaney defines the inverse scattering problem as consisting of "determining the functional form of a scattering potential given the scattering matrix $A(k_0\mathbf{s}, k_0\mathbf{s}_0)$ for all directions $\mathbf{s}$ and one or more values of the wave vector $k_0\mathbf{s}_0$." He shows in his paper, among other things, that the inverse scattering problem defined in this way does not have a unique solution within the framework of the first Born approximation. In his paper, he shows how to construct scattering potentials for objects invisible from one or more directions. These scattering potentials are of the form

$$F(\mathbf{r}) = -(\nabla^2 + 2ik_0\mathbf{s}_0 \cdot \nabla)\phi(\mathbf{r}), \tag{3.1}$$

where $\mathbf{s}_0$ is a unit vector, where k_0 is a wave number, and where $\phi(\mathbf{r})$ is a continuous function of $\mathbf{r}$ with continuous first partial derivatives. Objects with scattering

potentials like in equation (3.1) are invisible going along the direction of $\mathbf{s}_0$. Thus, if, for a unit vector $\mathbf{s}$, a plane wave $\exp(ik_0\mathbf{s}\cdot\mathbf{r})$ is incident upon our object along a direction of invisibility $\mathbf{s}_0$, the wave will not be scattered. Devaney went on to say that a scattering potential $F'(\mathbf{r})$ for an object invisible from the directions $k_0\mathbf{s}_0$ *and* $k_0'\mathbf{s}_0'$ could be created if we have

$$F'(\mathbf{r}) = (\nabla^2 + 2ik_0'\mathbf{s}_0'\cdot\nabla)(\nabla^2 + 2ik_0\mathbf{s}_0\cdot\nabla)\phi(\mathbf{r}). \tag{3.2}$$

Thus, to construct an object invisible from the directions of the unit vectors $\mathbf{s}_1,\ldots,\mathbf{s}_N$, we can have a scattering potential of the form

$$F(\mathbf{r}) = (\nabla^2 + 2ik_0\mathbf{s}_N\cdot\nabla)\cdots(\nabla^2 + 2ik_0\mathbf{s}_2\cdot\nabla)(\nabla^2 + 2ik_0\mathbf{s}_1\cdot\nabla)\phi(\mathbf{r}). \tag{3.3}$$

Building on Devaney's work in [21], Habashy and Wolf show in [88] that the inverse scattering problem has a unique solution if measurements are taken from an infinite number of directions of incidence of the incident wave. However, they also show in their paper that "within the accuracy of the first-order Born approximation there are no bodies that are invisible for all directions of incidence," not even those bodies whose scattering potentials are of the form shown in equation (3.3).

And in [29], Gbur creates several invisible objects, "directly from the defining wave equation," that are invisible in one direction but not others. He gives the exact scattering potential for such objects, invisible along the direction of the unit vector $\hat{\mathbf{s}}_0$, which are of the form

$$F(\mathbf{r}) = -\frac{1}{4\pi}\frac{\nabla^2 U_{\text{loc}}(\mathbf{r}) + 2ik\hat{\mathbf{s}}_0\cdot\nabla U_{\text{loc}}(\mathbf{r})}{1 + U_{\text{loc}}(\mathbf{r})}, \tag{3.4}$$

which bears some resemblance to equation (3.1). In equation (3.4), $U_{\text{loc}}(\mathbf{r})$ is a complex-valued function satisfying the boundary conditions of Theorem 2.2.1.

Although Devaney demonstrated the possibility of objects invisible from more than one direction, he never calculated the behavior of his invisible objects in his paper [21],

and neither did he generate any examples of such objects. In this chapter, using the results of [21, 29, 88], we create objects that are totally invisible from a finite number of directions and practically invisible from all other directions. The principal results of this chapter are the graphs of Figure 3.5, which show that, the more directions of invisibility an invisible object of ours has, the less power their scattered fields will radiate when a plane wave is incident upon our invisible object between directions of invisibility.

3.2 Deriving the Devaney Operator

In this chapter, we refer to the operator of equation (3.1) as the Devaney operator. In his derivation of the Devaney operator in [21], Devaney started off with the first Born approximation in 3D. However, the results of this chapter are in 2D. Thus, it would be good for us, following the steps outlined in [21], and starting off with the first Born approximation in 2D, to show how the Devaney operator is derived.

Let $U(\mathbf{r})$ be a scalar field, $V(\mathbf{r})$ a scattering potential potential, and k_0 a wave number. Thus, we have

$$(\nabla^2 + k_0^2)U(\mathbf{r}) = -4\pi V(\mathbf{r})U(\mathbf{r}). \tag{3.5}$$

In the case of weak scattering, we approximate $U(\mathbf{r})$ with the first Born approximation

$$U(\mathbf{r}) \approx U_i(\mathbf{r}) + \int_E i\pi H_0^{(1)}(k_0|\mathbf{r} - \mathbf{r}'|)V(\mathbf{r}')U_i(\mathbf{r})\, d^2\mathbf{r}', \tag{3.6}$$

where E denotes our finite scattering area, and where

$$U_i(\mathbf{r}) = U_0 \exp(ik_0\hat{\mathbf{s}}_0 \cdot \mathbf{r}) \tag{3.7}$$

is our plane wave of amplitude U_0, where $\hat{\mathbf{s}}_0$ is a unit vector. We have that

$$H_p^{(1)}(z) \approx \sqrt{\frac{2}{\pi z}} \exp\left(i\left(z - \frac{\pi p}{2} - \frac{\pi}{4}\right)\right). \tag{3.8}$$

Thus,

$$H_0^{(1)}(z) \approx \sqrt{\frac{2}{\pi z}} \exp\left(i\left(z - \frac{\pi}{4}\right)\right) = \sqrt{\frac{2}{\pi z}} \exp\left(-\frac{i\pi}{4}\right) \exp\left(iz\right) \tag{3.9}$$

so that

$$\begin{aligned} H_0^{(1)}(k_0|\mathbf{r}-\mathbf{r}'|) &\approx \sqrt{\frac{2}{\pi k_0|\mathbf{r}-\mathbf{r}'|}} \exp\left(-\frac{i\pi}{4}\right) \exp\left(ik_0|\mathbf{r}-\mathbf{r}'|\right) \\ &\approx \sqrt{\frac{2}{\pi k_0 r}} \exp\left(-\frac{i\pi}{4}\right) \exp\left(i(k_0 r - k\hat{\mathbf{s}}\cdot\mathbf{r}')\right) \\ &= \sqrt{\frac{2}{\pi k_0 r}} \exp\left(ik_0 r - \frac{i\pi}{4}\right) \exp(-ik_0\hat{\mathbf{s}}\cdot\mathbf{r}') \end{aligned} \tag{3.10}$$

for the unit vector $\hat{\mathbf{s}}$. Thus, as $k_0 r \to \infty$, we get from equation (3.6)

$$\begin{aligned} U(\mathbf{r}) &\approx U_i(\mathbf{r}) + \int_E \sqrt{\frac{2}{\pi k_0 r}} \exp\left(ik_0 r - \frac{i\pi}{4}\right) \exp(-ik_0\hat{\mathbf{s}}\cdot\mathbf{r}') V(\mathbf{r}') U_i(\mathbf{r}')\, d^2\mathbf{r}' \\ &= U_i(\mathbf{r}) + \sqrt{\frac{2}{\pi k_0 r}} \exp\left(ik_0 r - \frac{i\pi}{4}\right) \int_E V(\mathbf{r}') U_i(\mathbf{r}') \exp(-ik_0\hat{\mathbf{s}}\cdot\mathbf{r}')\, d^2\mathbf{r}' \\ &= U_i(\mathbf{r}) + \sqrt{\frac{2}{\pi k_0 r}} \exp\left(ik_0 r - \frac{i\pi}{4}\right) A_B(k_0\hat{\mathbf{s}}, k_0\hat{\mathbf{s}}_0), \end{aligned} \tag{3.11}$$

where

$$\begin{aligned} A_B(k_0\hat{\mathbf{s}}, k_0\hat{\mathbf{s}}_0) &= \int_E V(\mathbf{r}') U_i(\mathbf{r}') \exp(-ik_0\hat{\mathbf{s}}\cdot\mathbf{r}')\, d^2\mathbf{r}' \\ &= \int_E V(\mathbf{r}') \exp(ik_0\hat{\mathbf{s}}_0\cdot\mathbf{r}') \exp(-ik_0\hat{\mathbf{s}}\cdot\mathbf{r}')\, d^2\mathbf{r}' \end{aligned} \tag{3.12}$$

is our scattering matrix in the Born approximation.

The Fourier transform of our scattering potential $V(\mathbf{r})$ is

$$\tilde{V}(\mathbf{k}) = \int_E V(\mathbf{r}) \exp(-i\mathbf{k}\cdot\mathbf{r})\, d^2\mathbf{r}. \tag{3.13}$$

Thus, from equations (3.12) and (3.13), we get

$$A_B(k_0\hat{\mathbf{s}}, k_0\hat{\mathbf{s}}_0) = \tilde{V}[k_0(\hat{\mathbf{s}} - \hat{\mathbf{s}}_0)]. \tag{3.14}$$

Thus, the scattering matrix determines $\tilde{V}(\mathbf{k})$ for all $\mathbf{k}$ such that

$$\mathbf{k} = k_0(\hat{\mathbf{s}} - \hat{\mathbf{s}}_0). \tag{3.15}$$

In a scattering experiment, or, in the case of this chapter, in our simulations, when we use an incident plane wave $U_i(\mathbf{r})$ with a fixed wave vector $k_0\hat{\mathbf{s}}_0$, the values of $\mathbf{k}$ satisfying equation (3.15) lie on the surface defined by

$$\mathbf{k}\cdot\mathbf{k} = k^2 = 2k_0^2(1-\hat{\mathbf{s}}_0\cdot\hat{\mathbf{s}}). \tag{3.16}$$

What we want is a scattering potential $F(\mathbf{r})$ that produces a scattering matrix that vanishes for all $\hat{\mathbf{s}}$ but only one incident wave vector $k_0\hat{\mathbf{s}}_0$. The important thing to remember is that equation (3.14) holds when equation (3.15) holds. So when we construct a scattering potential $F(\mathbf{r})$ whose Fourier transform $\tilde{F}(\mathbf{k})$ vanishes for all $\mathbf{k}$ such that $\mathbf{k} = k_0(\hat{\mathbf{s}}-\hat{\mathbf{s}}_0)$, we construct a scattering potential whose scattering matrix vanishes for a fixed $k_0\hat{\mathbf{s}}_0$ and for all $\hat{\mathbf{s}}$.

Thus, we start off with

$$\tilde{F}(\mathbf{k}) = [k^2 - 2k_0^2(1-\hat{\mathbf{s}}_0\cdot\hat{\mathbf{s}})]\tilde{\phi}(\mathbf{k}), \tag{3.17}$$

where $\hat{\mathbf{s}}$ is as in equation (3.15). We choose $\tilde{\phi}(\mathbf{k})$ so that it has a Fourier transform $\phi(\mathbf{r})$ that is continuous with continuous first partial derivatives and is localized within E. Thus, with $k_0\hat{\mathbf{s}} = \mathbf{k} + k_0\hat{\mathbf{s}}_0$, equation (3.17) becomes

$$\begin{aligned}
\tilde{F}(\mathbf{k}) &= (k^2 - 2k_0^2(1-\hat{\mathbf{s}}_0\cdot\hat{\mathbf{s}}))\tilde{\phi}(\mathbf{k}) \\
&= (k^2 - 2k_0^2 + 2k_0\hat{\mathbf{s}}_0\cdot k_0\hat{\mathbf{s}})\tilde{\phi}(\mathbf{k}) \\
&= (k^2 - 2k_0^2 + 2k_0\hat{\mathbf{s}}_0\cdot(\mathbf{k}+k_0\hat{\mathbf{s}}_0))\tilde{\phi}(\mathbf{k}) \\
&= (k^2 + 2k_0\hat{\mathbf{s}}_0\cdot\mathbf{k})\tilde{\phi}(\mathbf{k}).
\end{aligned} \tag{3.18}$$

Thus, taking the inverse Fourier transform of $F(\mathbf{r})$, we get

$$F(\mathbf{r}) = \frac{1}{(2\pi)^2}\int \tilde{F}(\mathbf{k})\exp(i\mathbf{k}\cdot\mathbf{r})\,d^2\mathbf{k} = (\nabla^2 + 2ik_0\hat{\mathbf{s}}_0\cdot\nabla)\phi(\mathbf{r}). \tag{3.19}$$

And thus we have what we refer to in this chapter as the Devaney operator $\nabla^2 + 2ik_0\hat{\mathbf{s}}_0\cdot\nabla$.

Now, the last thing we need to do is to show that the Devaney operator works the way we want for it to, that it gives us a scattering matrix that vanishes. First, we want to substitute $F(\mathbf{r})$ for $V(\mathbf{r})$ in equation (3.12). Thus, we get

$$A_B(k_0\hat{\mathbf{s}}, k_0\hat{\mathbf{s}}_0) = -\int_E [(\nabla^2 + 2ik_0\hat{\mathbf{s}}_0 \cdot \nabla)\phi(\mathbf{r})] \exp(ik_0\hat{\mathbf{s}}_0 \cdot \mathbf{r}) \exp(-ik_0\hat{\mathbf{s}} \cdot \mathbf{r})\, d^2\mathbf{r}. \quad (3.20)$$

We have that

$$(\nabla^2 + k_0^2)[\phi(\mathbf{r}) \exp(ik_0\hat{\mathbf{s}}_0 \cdot \mathbf{r})] \equiv \exp(ik_0\hat{\mathbf{s}}_0 \cdot \mathbf{r})[\nabla^2 + 2ik_0\hat{\mathbf{s}}_0 \cdot \nabla]\phi(\mathbf{r}). \quad (3.21)$$

Thus, keeping in mind that

$$(\nabla^2 + k_0^2) \exp(-ik_0\hat{\mathbf{s}} \cdot \mathbf{r}) = 0, \quad (3.22)$$

when we substitute equation (3.21) into equation (3.20), we get

$$\begin{aligned} A_B(k_0\hat{\mathbf{s}}, k_0\hat{\mathbf{s}}_0) &= \int_E [\exp(ik_0\hat{\mathbf{s}}_0 \cdot \mathbf{r})(\nabla^2 + 2ik_0\hat{\mathbf{s}}_0 \cdot \nabla)\phi(\mathbf{r})] \exp(-ik_0\hat{\mathbf{s}} \cdot \mathbf{r})\, d^2\mathbf{r} \\ &= \int_E [(\nabla^2 + k_0^2)(\phi(\mathbf{r}) \exp(ik_0\hat{\mathbf{s}}_0 \cdot \mathbf{r}))] \exp(-ik_0\hat{\mathbf{s}} \cdot \mathbf{r})\, d^2\mathbf{r} \\ &= \int_E [\phi(\mathbf{r}) \exp(ik_0\hat{\mathbf{s}}_0 \cdot \mathbf{r})](\nabla^2 + k_0^2) \exp(-ik_0\hat{\mathbf{s}} \cdot \mathbf{r})\, d^2\mathbf{r} \\ &= 0. \end{aligned} \quad (3.23)$$

Thus, our scattering potential $F(\mathbf{r})$ gives us a scattering matrix $A_B(k_0\hat{\mathbf{s}}, k_0\hat{\mathbf{s}}_0)$ that identically equals zero, just as we wanted.

And from this point forward, for a unit vector $\hat{\mathbf{s}}$ and a wave number k, we denote the Devaney operator as

$$D[k\hat{\mathbf{s}}] = \nabla^2 + 2ik\hat{\mathbf{s}} \cdot \nabla. \quad (3.24)$$

3.3 Constructing Our Invisible Objects and Our Plan to Test Them

Now that we have our Devaney operator, we can use it to create the scattering potentials of some invisible objects. Let $E = \{\mathbf{r} = (r, \theta) \in \mathbb{R}^2 : 0 \leq r \leq r_0\} \subset \mathbb{R}^2$ be the area to which our invisible object is confined. Drawing from [29], we want a

function $U_{\text{loc}} : \mathbb{R}^2 \to \mathbb{C}$ such that $U_{\text{loc}}(\mathbf{r}) = 0$ for $\mathbf{r} \in \partial E$ and $\mathbf{r} \in \mathbb{R}^2 \setminus E$, and whose first partial derivatives are continuous on E. Let $\hat{\mathbf{s}}_1$ be a unit vector, and k a wave number. Thus, the scattering potential

$$F(\mathbf{r}) = D[k\hat{\mathbf{s}}_1]U_{\text{loc}}(\mathbf{r}) \tag{3.25}$$

will give us an object confined to E that is invisible along the direction of $\hat{\mathbf{s}}_1$. Now, say we want an object invisible along the directions of the unit vectors $\hat{\mathbf{s}}_1$ and $\hat{\mathbf{s}}_2$, with wave number k. Then, for this object, we have the scattering potential

$$F(\mathbf{r}) = D[k\hat{\mathbf{s}}_2]D[k\hat{\mathbf{s}}_1]U_{\text{loc}}(\mathbf{r}), \tag{3.26}$$

where $D[k\hat{\mathbf{s}}_1]U_{\text{loc}}(\mathbf{r})$ has first partial derivatives that are continuous on E, and where $U_{\text{loc}}(\mathbf{r})$ needs to be at least three times continuously differentiable on E since the operator $D[k\hat{\mathbf{s}}_2]D[k\hat{\mathbf{s}}_1]$ has four derivatives. Thus, say we want an object invisible along the directions of the unit vectors $\hat{\mathbf{s}}_1, \ldots, \hat{\mathbf{s}}_N$. Then we have the scattering potential

$$F(\mathbf{r}) = D[k\hat{\mathbf{s}}_N] \cdots D[k\hat{\mathbf{s}}_2]D[k\hat{\mathbf{s}}_1]U_{\text{loc}}(\mathbf{r}), \tag{3.27}$$

where $D[k\hat{\mathbf{s}}_{N-1}] \cdots D[k\hat{\mathbf{s}}_2]D[k\hat{\mathbf{s}}_1]U_{\text{loc}}(\mathbf{r})$ has first partial derivatives that are continuous on E, and where $U_{\text{loc}}(\mathbf{r})$ is at least $2N-1$ times continuously differentiable on E since the operator $D[k\hat{\mathbf{s}}_N] \cdots D[k\hat{\mathbf{s}}_2]D[k\hat{\mathbf{s}}_1]$ has $2N$ derivatives.

Next, we need $U_{\text{loc}}(\mathbf{r})$ to be such that $F(\mathbf{r})$ is the scattering potential of a nonscattering scatterer. For an object invisible only along the direction of the unit vector $\hat{\mathbf{s}}_1$, whose scattering potential is equation (3.25), recalling Theorem 2.2.1, we need for $U_{\text{loc}}(\mathbf{r})$ to satisfy the boundary conditions

$$U_{\text{loc}}(\mathbf{r}) = \partial_{\mathbf{n}} U_{\text{loc}}(\mathbf{r}) = 0 \text{ for } \mathbf{r} \in \partial E, \tag{3.28}$$

where $\mathbf{n}$ is the unit normal vector pointing outward from the boundary of E. But for an object invisible from the N directions of the unit vectors $\hat{\mathbf{s}}_1, \ldots, \hat{\mathbf{s}}_N$, whose

scattering potential is equation (3.27), we need $D[k\hat{\mathbf{s}}_{N-1}]\cdots D[k\hat{\mathbf{s}}_2]D[k\hat{\mathbf{s}}_1]U_{\text{loc}}(\mathbf{r})$ to satisfy the boundary conditions of Theorem 2.2.1, which means that we need $U_{\text{loc}}(\mathbf{r})$ to satisfy the boundary conditions

$$U_{\text{loc}}(\mathbf{r}) = \partial_{\mathbf{n}}U_{\text{loc}}(\mathbf{r}) = \partial_{\mathbf{n}}^2U_{\text{loc}}(\mathbf{r}) = \cdots = \partial_{\mathbf{n}}^{2N-1}U_{\text{loc}}(\mathbf{r}) = 0 \text{ for } \mathbf{r} \in \partial E. \tag{3.29}$$

We want $U_{\text{loc}}(\mathbf{r})$ defined according to the rule $U_{\text{loc}}(\mathbf{r}) = v(r) + iv(r)$, where

$$v(r) = \begin{cases} f(r) & r \in [-r_0, r_0], \\ 0 & \text{otherwise}, \end{cases} \tag{3.30}$$

where r_0 is the radius of our set E. In our simulations, we test for two kinds of $U_{\text{loc}}(\mathbf{r})$. The first kind of $U_{\text{loc}}(\mathbf{r})$ is m times continuously differentiable, and, taking inspiration from [66], $f(r)$ is a polynomial of the form

$$f(r) = \sum_{j=0}^{m+1} c_{n+2j} r^{n+2j} \tag{3.31}$$

with $m+2$ terms, where $n \in \mathbb{N}_0$. To find the coefficients c_{n+2j}, in our simulations, we set up and solve a system of equations. Since we want $U_{\text{loc}}(\mathbf{r})$ to be m times continuously differentiable, we need $v(r)$ to also be m times continuously differentiable. Thus, we will need $v(r)$ to satisfy

$$v(\pm r_0) = v'(\pm r_0) = \cdots = v^{(m)}(\pm r_0) = 0. \tag{3.32}$$

Then, setting up our system of equations consisting of $m+1$ equations

$$\begin{aligned} f(r_0) &= 0, \\ f'(r_0) &= 0, \\ &\vdots \\ f^{(m)}(r_0) &= 0, \end{aligned} \tag{3.33}$$

we solve for our coefficients $c_n, \ldots, c_{n+2m}$, where the last coefficient $c_{n+2(m+1)}$ is our free variable, which we put down as $c_{n+2(m+1)} = 1$. For an object with N directions

of invisibility, we need $m \geq 2N + 1$. And for the second kind of $U_{\text{loc}}(\mathbf{r})$, $v(r)$ is just simply the infinitely continuously differentiable bump function, defined as

$$v(r) = \begin{cases} \exp\left(\frac{1}{(r/r_0)^2 - 1}\right) & r \in (-r_0, r_0), \\ 0 & \text{otherwise.} \end{cases} \tag{3.34}$$

We want to test for the bump function because, since it is infinitely continuously differentiable, we can use this one function can give us a scattering potential for an object that is invisible in as many directions as we want.

In our simulations, we test for six different objects whose scattering potentials are based on a polynomial, and we test for another six objects whose scattering potentials are based on the bump function. Let R be the region containing the domain E of our invisible object. Now, the more times we apply the Devaney operator to a given $U_{\text{loc}}(\mathbf{r})$, the greater its $\max_{\mathbf{r}\in R} \Re[F(\mathbf{r})]$ and $\max_{\mathbf{r}\in R} \Im[F(\mathbf{r})]$ become. In fact, for a particular $U_{\text{loc}}(\mathbf{r})$, $\max_{\mathbf{r}\in R} \Re[F(\mathbf{r})]$ and $\max_{\mathbf{r}\in R} \Im[F(\mathbf{r})]$ increase by many orders of magnitude the more we apply the Devaney operator to $U_{\text{loc}}(\mathbf{r})$, and we do not want this affecting our results. Thus, we want to control for $\max_{\mathbf{r}\in R} \Re[F(\mathbf{r})]$ and $\max_{\mathbf{r}\in R} \Im[F(\mathbf{r})]$; that is, we want $\max_{\mathbf{r}\in R} \Re[F(\mathbf{r})]$ and $\max_{\mathbf{r}\in R} \Im[F(\mathbf{r})]$ to be roughly about the same for all of our objects for a given $U_{\text{loc}}(\mathbf{r})$. Thus, once we compute our scattering potentials $F(\mathbf{r})$, we then calculate our normalized scattering potentials

$$F_{\text{norm}}(\mathbf{r}) = \frac{F(\mathbf{r})}{\|F(\mathbf{r})\|_{L^1(R)}} \tag{3.35}$$

using the L^1 norm

$$\|F(\mathbf{r})\|_{L^1(R)} = \int_R |F(\mathbf{r})| \, d^2\mathbf{r}. \tag{3.36}$$

The wave going through our object is of the form

$$U_i(\mathbf{r}) = U_0 \exp(ik\hat{\mathbf{s}}_0 \cdot \mathbf{r}), \tag{3.37}$$

where $\hat{\mathbf{s}}_0 = \langle \cos\theta_i, \sin\theta_i \rangle$ is a unit vector pointing at the initial angle θ_i with respect

to the x-axis, indicating the direction in which our wave propagates. Our scattered field for our given scattering potential is given by the Green's formula

$$U_s(\mathbf{r}) = \int_R i\pi H_0^{(1)}(k|\mathbf{r}-\mathbf{r}'|)F_{\text{norm}}(\mathbf{r}')U_i(\mathbf{r}')\,d^2\mathbf{r}', \tag{3.38}$$

where $H_0^{(1)}$ is the Hankel function of the first kind.

Finally, for each of our objects, we want to see how much power their scattered fields radiate when we change the angle of incidence θ_i of $U_i(\mathbf{r})$. Thus, for a set of values of θ_i from 0° to 360°, we calculate our scattered field $U_s(\mathbf{r})$. And then we calculate the power radiated by our scattered field for a given incident angle θ_i according to the formula

$$P = \int_0^{2\pi} r|U_s(r,\theta')|^2\,d\theta' \tag{3.39}$$

for a fixed value of r. From these calculations, we get the total power P radiated by our scattered fields as a function of incident angle θ_i. And along each direction of invisibility, we should have $P = 0$.

Our goal is to see if the maximum power radiated by the scattered fields of each of our objects goes down the more directions of invisibility our objects have.

3.4 Our Simulations and Results

In our numerical experiments, we refer to as our "polynomial objects" those six objects whose scattering potentials are based on a polynomial, and we refer to as our "bump function objects" those other six objects whose scattering potentials are based on the bump function. In our numerical experiments, an object named Object 1 is invisible from one direction, an object named Object 2 is invisible from two directions, and so on so that an object named Object 6 is invisible from six directions.

The first thing we want to do for every object we test is do define our constants. In all of our experiments, we have $U_0 = 1$, we have the radius of our scatterer to be $r_0 = 1$, we have our wavelength to be $\lambda = 1$, and we have our wave number to be

$k = 2\pi/\lambda$. And we define all of our functions on the region $R = [-2, 2] \times [-2, 2]$. For the scattering potentials based on polynomials, we have $n = 0$, and we let $m = 11$ be the number of times continuously differentiable we want our $U_{\text{loc}}(\mathbf{r})$ to be. But for our scattering potentials based on the bump function, there is no need to define a number of times we want $U_{\text{loc}}(\mathbf{r})$ to be continuously differentiable as the bump function is infinitely many times continuously differentiable. We have one $U_{\text{loc}}(\mathbf{r})$ for all six of our polynomial objects and another $U_{\text{loc}}(\mathbf{r})$ for all six of our bump function objects.

Next, for each of our objects, we want to define our directions of invisibility. Object 1 in both the polynomial and bump function cases is invisible only from the direction $\theta = 0°$, or in the direction of the unit vector $\hat{\mathbf{s}}_1 = \langle 1, 0\rangle$. For the rest of the Objects 2 through 6, their directions of invisibility are evenly spaced so that the angle between directions of invisibility is $360°/N$, where N denotes the number of directions from which a particular object is invisible. All of our objects are invisible from $\theta = 0°$.

Next, for each of our objects, we want to create a scattering potential. First, we compute $v(r)$. For the $U_{\text{loc}}(\mathbf{r})$ based on a polynomial, we take our values r_0, n, and m and construct our system of equations (3.33) and solve it to find the coefficients of a polynomial suitable to be the $f(r)$ in our $v(r)$. But for our $U_{\text{loc}}(\mathbf{r})$ based on the bump function, we just to define $v(r)$ according to equation (3.34). Once we have our $U_{\text{loc}}(\mathbf{r})$, we apply the Devaney operator to it once for every direction our object is supposed to be invisible to give us our scattering potential $F(\mathbf{r})$, according to equation (3.27). It should be noted that the gradients and Laplacians in our Devaney operators are numerically calculated in our experiments using MATLAB's `grad` and `del2` functions, respectively.

And for each of our objects, once we have their scattering potentials, we normalize them according to equation (3.35) to get their corresponding $F_{\text{norm}}(\mathbf{r})$'s. Figure 3.1 shows the graphs of the real and imaginary parts of the normalized scattering po-

tentials for our odd numbered polynomial objects. And Figure 3.2 shows the graphs of the real and imaginary parts of the normalized scattering potentials for our odd numbered bump function objects. The red circles in these two figures, and in all of the rest of the figures of this chapter in which they appear, indicate ∂E, the boundaries of our invisible objects. What we can see from Figures 3.1 and 3.2 is that the $\Re[F_{\text{norm}}(\mathbf{r})]$'s and their corresponding $\Im[F_{\text{norm}}(\mathbf{r})]$'s are mirror images of each other.

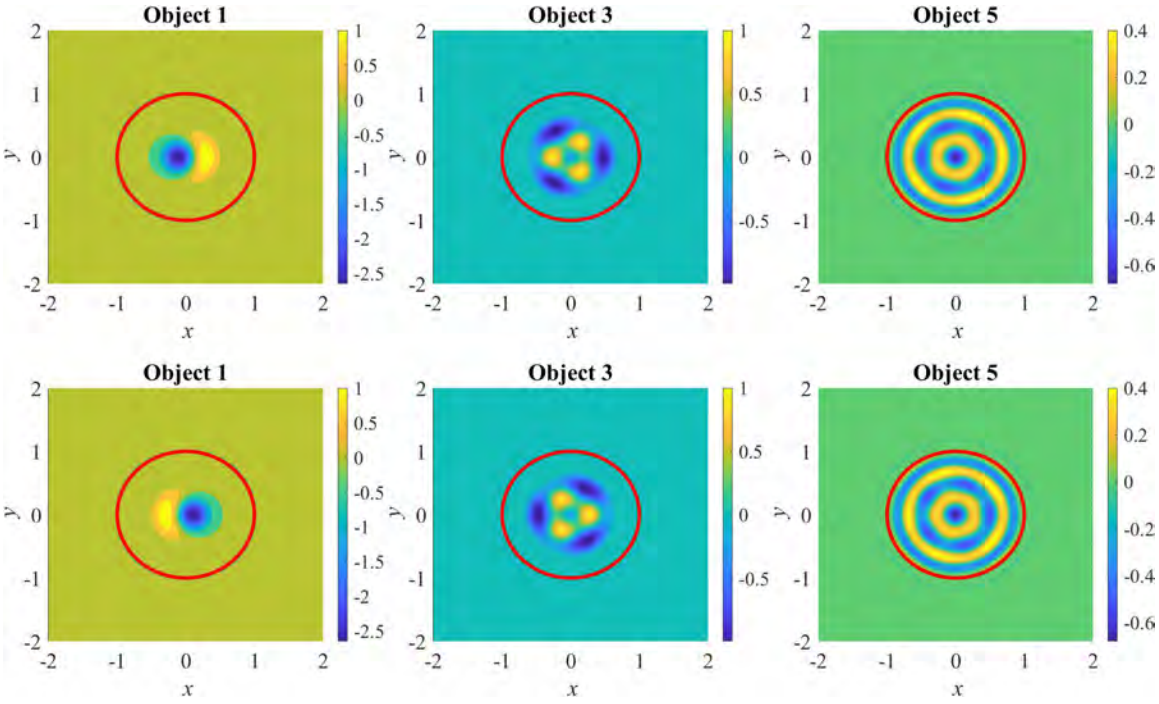

Figure 3.1: The graphs of $\Re[F_{\text{norm}}(\mathbf{r})]$ and $\Im[F_{\text{norm}}(\mathbf{r})]$ of the scattering potentials of our odd numbered polynomial objects. The top row is for real parts and the bottom row is for imaginary parts. The grainy rings we see around the edges of our objects are artifacts due to computational error. Our scattering potentials are symmetrical along the same directions that our objects are invisible.

Next, for each of our objects, and for each of the initial angles $\theta = 0°, 5°, \ldots, 360°$, we calculate our scattered field $U_s(\mathbf{r})$ using the Green's formula given in equation (3.38). The total power radiated for each scattered field is given by equation (3.39). Thus, for every initial angle $\theta = 0°, 5°, \ldots 360°$, we calculate P at $r = 2$ and get $P(\theta)$, the total power radiated as a function of initial angle θ. Figure 3.3 shows the

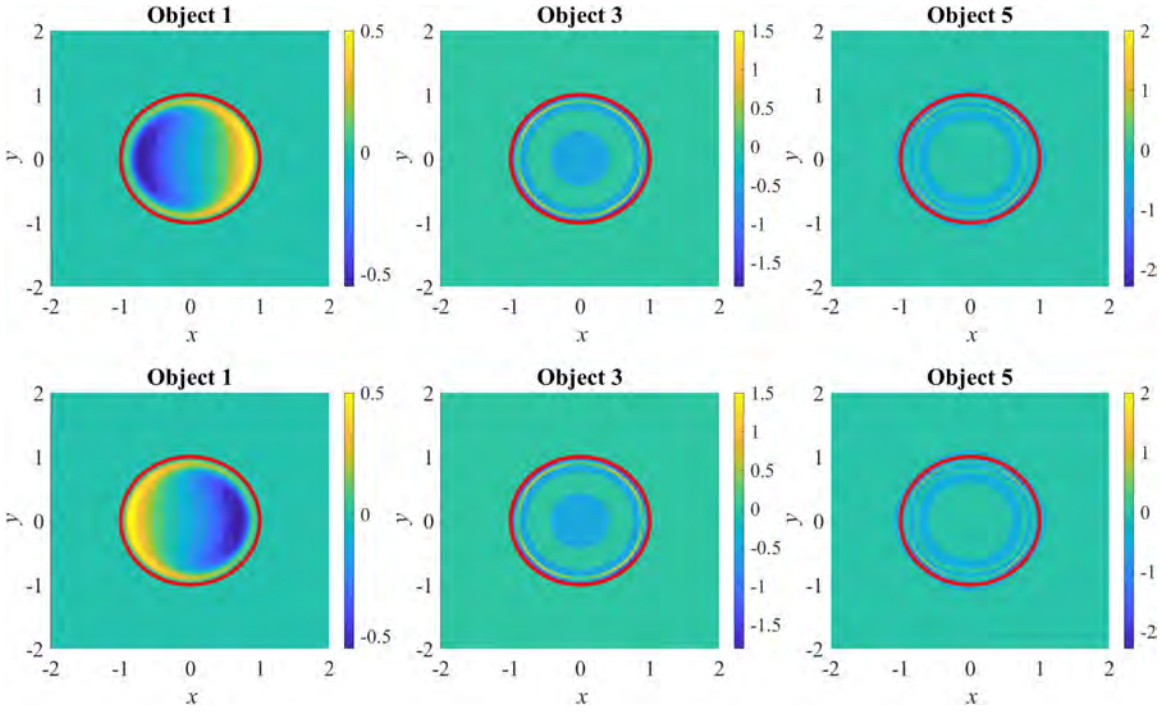

Figure 3.2: The graphs of $\Re[F_{\text{norm}}(\mathbf{r})]$ and $\Im[F_{\text{norm}}(\mathbf{r})]$ for the scattering potentials of our odd numbered bump function objects. Again, the top row is for the $\Re[F_{\text{norm}}(\mathbf{r})]$'s and the bottom row is for the $\Im[F_{\text{norm}}(\mathbf{r})]$'s.

graphs of $P(\theta)$ for each of our six polynomial objects. Now, due to computational error, for Objects 4, 5, and 6, we can see that the troughs of our graphs are not quite at zero like they should be considering that these troughs indicate directions of invisibility. And Figure 3.4 shows similar graphs for our bump function objects. And we have a similar issue with these graphs due to computational error as we do with our polynomial objects in Figure 3.3.

Having our functions $P(\theta)$ for all of our objects, we determine the maximum value of each $P(\theta)$ and get $P_{\max}(N)$, which is the maximum power radiated by our scattered fields as a function of N, the number of directions of invisibility. Figure 3.5 shows the graphs of $P_{\max}(N)$ for our polynomial objects and the graph of $P_{\max}(N)$ for our bump function objects. Our graphs in Figure 3.5 show that, the more directions of invisibility our objects have, the less power their scattered fields radiate when our plane wave U_i approaches our object between directions of invisibility. This effect is

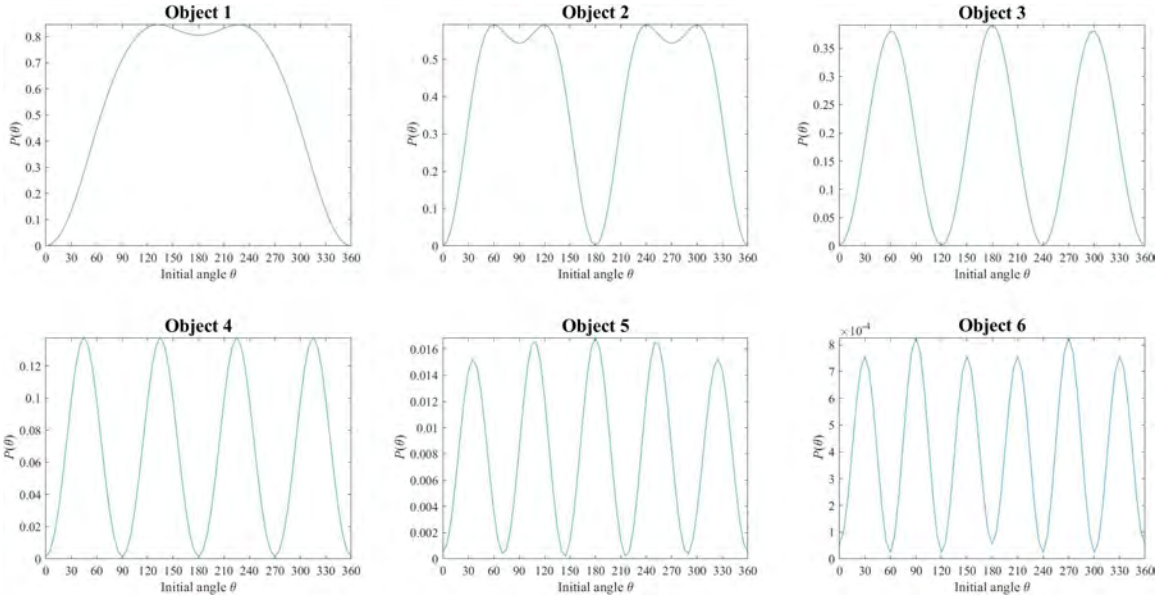

Figure 3.3: $P(\theta)$ for each of our six polynomial objects.

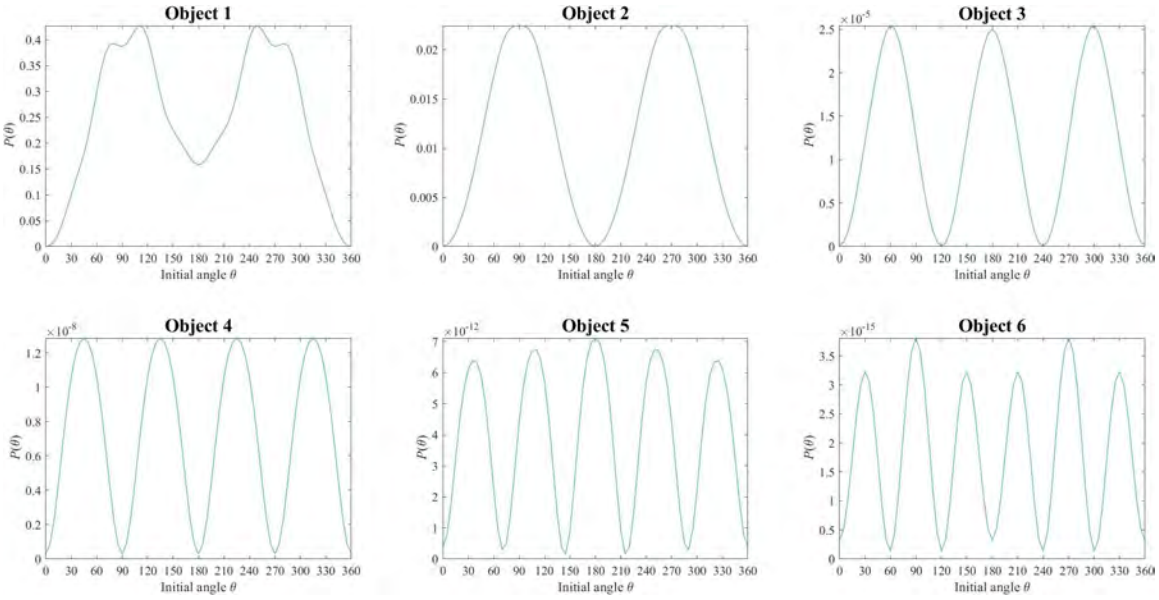

Figure 3.4: $P(\theta)$ for each of our six bump function objects.

even more pronounced for our bump function objects than it is for our polynomial objects.

Figure 3.6 demonstrates how our objects can be invisible in some directions but not in others. Figure 3.6 shows for Object 3 of the polynomial objects the real part

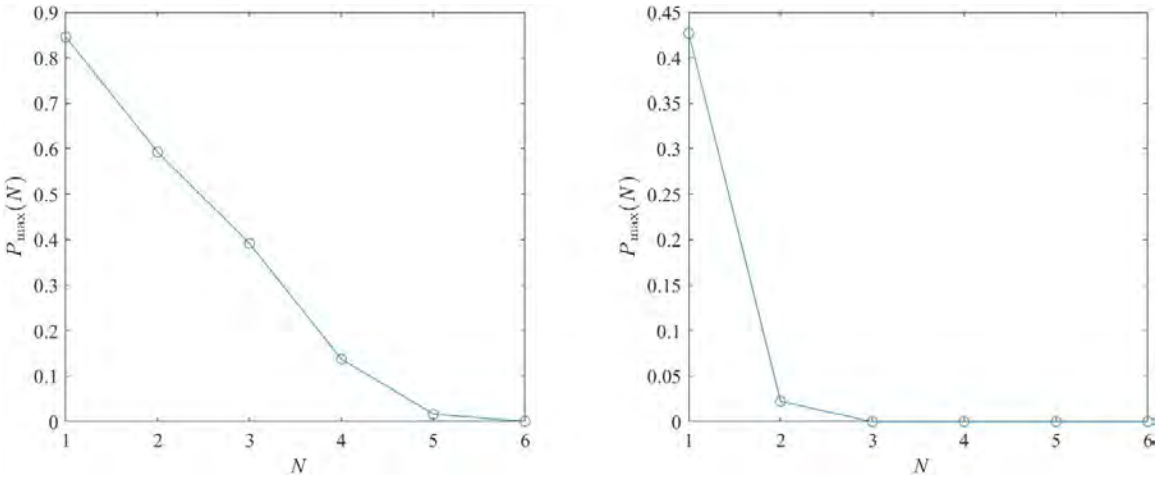

Figure 3.5: The graph of $P_{\max}(N)$ against N for all six of our objects. The graph on the left is for the polynomial objects, and the graph on the right is for the bump function objects. Note how for both the polynomial objects and the bump function objects $P_{\max}(N)$ decreases as N increases.

of the total field $U(\mathbf{r}) = U_i(\mathbf{r}) + U_s(\mathbf{r})$ with $U_i(\mathbf{r})$ going in two different directions.

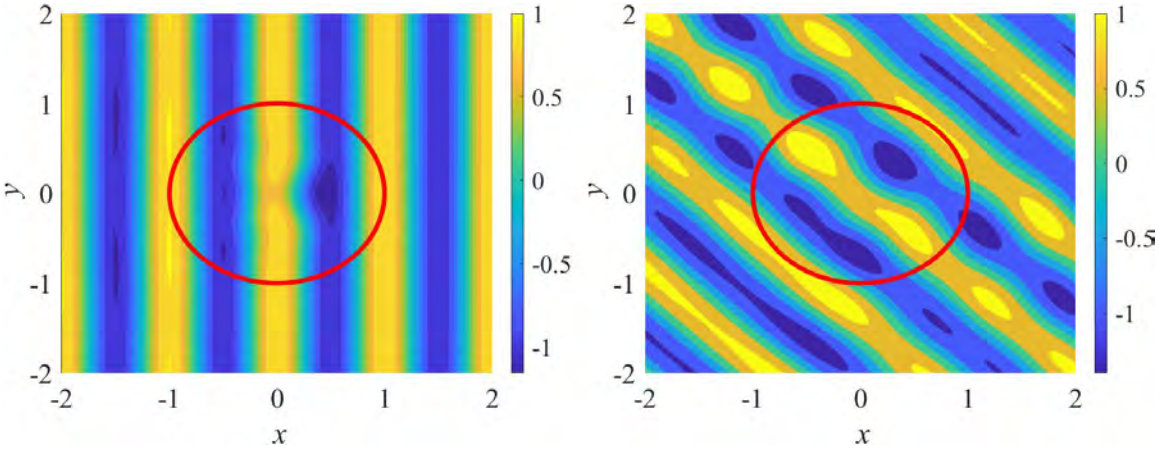

Figure 3.6: Plots of the real part of the total field $U(\mathbf{r}) = U_i(\mathbf{r}) + U_s(\mathbf{r})$ for Object 3 of the polynomial objects. Here, we have $U_i(\mathbf{r})$ going through Object 3 of the polynomial objects from two different angles. On the left, we have $U_i(\mathbf{r})$ going through Object 3 with an initial angle of $\theta = 0°$, which is along one of its directions of invisibility. Note how the waves pass clean through. On the right, we have $U_i(\mathbf{r})$ going through Object 3 with an initial angle of $\theta = 45°$, which is *not* along one of Object 3's directions of invisibility. Note how scattered our wave is.

And finally, Figure 3.7 shows $|U_s(\mathbf{r})|^2$ for all six of our polynomial with our incident wave $U_i(\mathbf{r})$ going along with an incident angle of $\theta = 0°$, and Figure 3.8 shows the

same thing but with all six of our bump function objects.

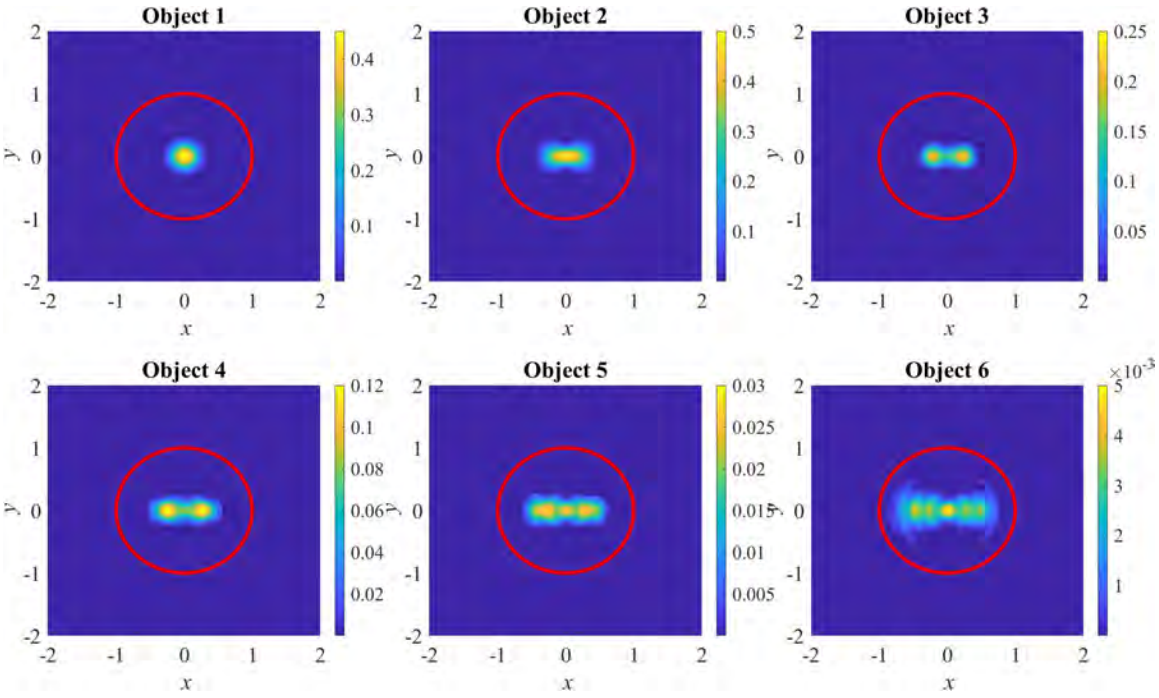

Figure 3.7: The graphs of $|U_s(\mathbf{r})|^2$ for all six of our polynomial objects. With all six of our objects, the incident angle of our wave $U_i(\mathbf{r})$ is $\theta = 0°$.

3.5 Conclusions

Thus, from our simulations and our data, we can make several conclusions: We can use the Devaney operator to create objects invisible from one or more directions. When a wave is incident from a direction different from one of our invisible object's directions of invisibility, the power radiated by that object's scattered field decreases the more directions of invisibility our object has. Thus, if we want to make an object that is *practically* invisible, we do not need for it to be invisible from *every* direction. Instead it would suffice for our object to be invisible from only a few directions. For one of our polynomial objects, it would be enough to make it invisible from four or five directions. And for a bump function object, two directions of invisibility is enough.

So, as potential follow-ups to this work, we can also see what happens when we use

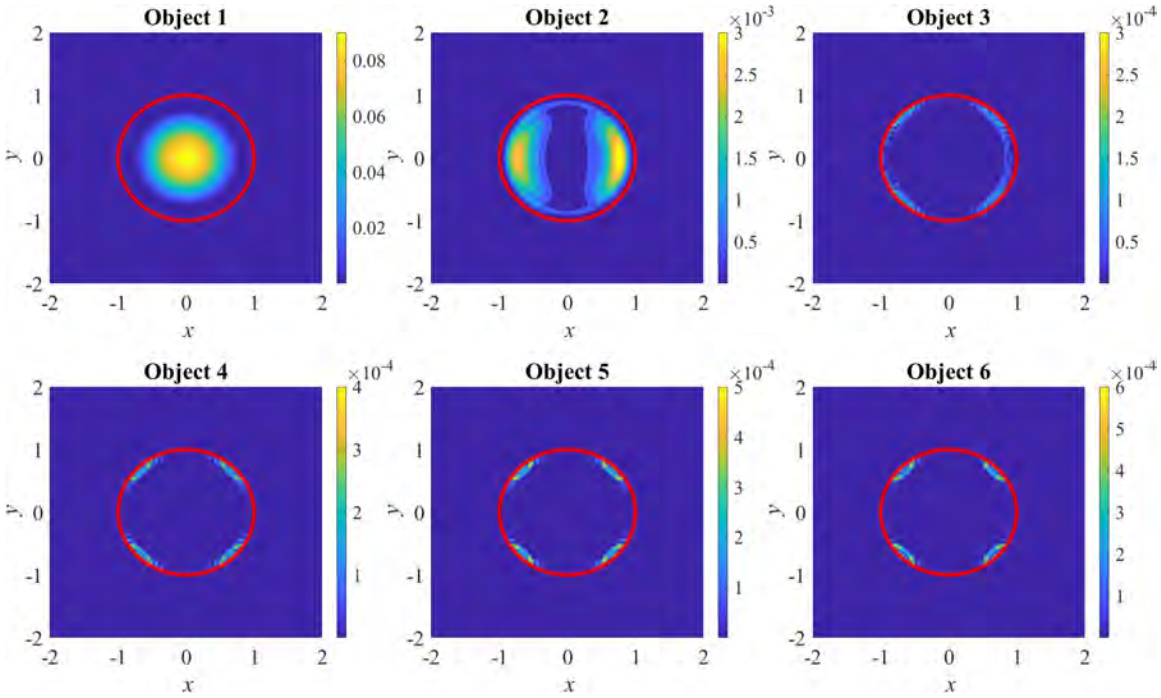

Figure 3.8: The graphs of $|U_s(\mathbf{r})|^2$ for all six of our bump function objects. With all six of our objects, the incident angle of our wave $U_i(\mathbf{r})$ is $\theta = 0°$.

non-weak scatterers, or scatterers beyond the Born approximation, or what happens when $F(\mathbf{r})$ is real-valued.

CHAPTER 4: A CARLEMAN-PICARD APPROACH FOR RECONSTRUCTING ZERO-ORDER COEFFICIENTS IN PARABOLIC EQUATIONS WITH LIMITED DATA

The content of this chapter is reproduced from [4] with permission from the authors/publisher.

We propose a globally convergent computational technique for the nonlinear inverse problem of reconstructing the zero-order coefficient in a parabolic equation using partial boundary data. This technique is called the "reduced dimensional method." Initially, we use the polynomial-exponential basis to approximate the inverse problem as a system of 1D nonlinear equations. We then employ a Picard iteration based on the quasi-reversibility method and a Carleman weight function. We will rigorously prove that the sequence derived from this iteration converges to the accurate solution for that 1D system without requesting a good initial guess of the true solution. The key tool for the proof is a Carleman estimate. We will also show some numerical examples.

4.1 Introduction

Let $d \geq 2$ be the spatial dimension. We aim to solve a coefficient inverse problem for the following initial value problem

$$\begin{cases} u_t(\mathbf{x},t) &= \Delta u(\mathbf{x},t) + c(\mathbf{x})u(\mathbf{x},t) \quad (\mathbf{x},t) \in \mathbb{R}^d \times (0,\infty), \\ u(\mathbf{x},0) &= p(\mathbf{x}) \qquad\qquad\qquad\qquad \mathbf{x} \in \mathbb{R}^d. \end{cases} \tag{4.1}$$

More precisely, we propose a globally convergent method to solve the following inverse problem.

Problem 4.1.1. *Let R and T be two positive numbers. Define $\Omega = (-R, R)^d$, and*

$$\Gamma = \{\mathbf{x} = (\mathbf{x}', z) : \mathbf{x}' = (x_1, \ldots, x_{d-1}), |x_i| < R, i = 1, \ldots, d-1, z = \pm R\} \subset \partial\Omega. \tag{4.2}$$

Assume that $|p| > 0$ in $\overline{\Omega}$. Given the boundary measurements

$$f(\mathbf{x}, t) = u(\mathbf{x}, t) \text{ and } g(\mathbf{x}, t) = u_z(\mathbf{x}, t) \tag{4.3}$$

for all $(\mathbf{x}, t) \in \Gamma \times (0, T)$, compute the coefficient $c(\mathbf{x})$, for $\mathbf{x} \in \Omega$.

Problem 4.1.1 boasts countless real-world applications. Consider a scenario where the internal points of the medium Ω remain inaccessible. By recording partial boundary data of the function u, specifically the heat and heat flux, over a designated time frame and by resolving Problem 4.1.1, one can identify the coefficient $c(\mathbf{x})$, $\mathbf{x} \in \Omega$. This allows the medium to be examined without causing any damage to it. An important example can be drawn from bioheat transfer, where the coefficient $c(\mathbf{x})$ signifies blood perfusion. Understanding this coefficient is vital for determining the temperature of blood coursing through tissue, as highlighted in [17]. However, the uniqueness of Problem 4.1.1, especially when data collection is limited to a specific subset of $\partial\Omega$, remains an open area and is explored within the reduced dimensional framework. Variations of Problem 4.1.1, with some internal data assumed to be known, have been addressed in [8, 15, 78]. Additionally, the uniqueness can be found in [37] when provided with the Dirichlet to Neuman map. This chapter assumes the uniqueness of Problem 4.1.1. Another topic of interest is the inverse challenge of retrieving other coefficients, such as diffusion or initial conditions, based on the final time measurements or boundary measurements for parabolic equations. This is an intriguing and critical issue, with theoretical findings and computational methods elaborated in [1, 52, 55, 57, 61, 68, 79, 87].

Inverse problems of computing the coefficients for parabolic equations have been ex-

tensively explored. To the authors' knowledge, the widely-used technique for resolving such issues is the optimal control approach; see the important works [11, 16, 17, 41, 89] and other cited references. The researchers in [11] employed the optimal control method with a preconditioner to achieve high-quality numerical calculations of thermal conductivity. However, a significant limitation of this technique is the necessity for a reliable initial estimation of the true solution, which is not consistently accessible. We would like to particularly highlight the convexification method, as described in [6, 47, 50, 54]. This approach addresses the challenge of obtaining an initial guess. The studies in [6, 47, 50, 54] suggested to minimize some Carleman weighted strictly convex functionals. When minimized, the minimizers of these functionals produce the solution to the problem at hand. Other worthy mentions are [70] and [75], which respectively present alternative approaches to address Problem 4.1.1 by iteratively solving a Picard-like approximation and its linearization. The approaches above consider the full boundary observation. Unlike this, our contribution is introducing a fresh technique that does not rely on prior insights into the actual coefficient and requests only partial observation.

Our approach to addressing Problem 4.1.1 is split into two phases. In the initial phase, drawing inspiration from [70, 75], we eliminate the unknown coefficient $c(\mathbf{x})$ from (4.1). By this, we obtain a partial differential equation. The equation that emerges from this phase is a complicated one, which involves both nonlocal and nonlinear terms. On the other hand, the boundary condition of the solution is only provided on $\Gamma \subsetneq \partial\Omega$. As of now, there is no established numerical method to address it. During the subsequent phase, we transform this equation into a system of nonlinear ordinary differential equations. This transformation is guided by truncating the Fourier series with respect to a special basis introduced in paper [74]. This basis is named the polynomial-exponential basis. It is the high-dimensional version of the 1D polynomial-exponential basis originally introduced in [48]. We then

deploy a predictor-corrector strategy to solve this nonlinear system. Within this framework, the preliminary approximation of the true solution is derived without any prior understanding. Subsequently, the resolution to Problem 4.1.1 is achieved. The corrector stage in this procedure is executed using the quasi-reversibility method and a Carleman weight function. The quasi-reversibility method was first introduced by Lattès and Lions in [53] for numerical solutions of ill-posed problems for partial differential equations. It has been studied intensively since then, see e.g., [7, 12, 13, 14, 18, 20, 39, 51, 45, 69, 73]. A survey on this method can be found in [46]. A question arises immediately whether or not the iteration led by the predictor-corrector procedure above converges. We will rigorously prove this important result. The proof is motivated by the one in [55, 57, 71]. However, its advantage is that we can relax a technical condition in those papers about the smoothness of the noise. That means the noise model in this chapter is more realistic than in the earlier publications.

This chapter is organized as follows. In Section 4.2, we introduce our approximation dimensional model that leads to the dimensional reduction approach. In Section 4.3, we establish a 1D Carleman estimate. Section 4.4 is for the algorithm and the proof of its convergence. In Section 4.5, we present our numerical study. Section 4.6 is for concluding remarks.

4.2 The Reduced Dimension Model

Define

$$v(\mathbf{x}, t) = u_t(\mathbf{x}, t) \text{ for all } (\mathbf{x}, t) \in \Omega \times (0, T). \tag{4.4}$$

Then, by differentiating both sides of the differential equation in (4.1) with respect to t, we obtain

$$v_t(\mathbf{x}, t) = \Delta v(\mathbf{x}, t) + c(\mathbf{x})v(\mathbf{x}, t) \text{ for all } (\mathbf{x}, t) \in \Omega \times (0, T). \tag{4.5}$$

Since $u(\mathbf{x}, 0) = p(\mathbf{x})$, we have

$$v(\mathbf{x}, 0) = u_t(\mathbf{x}, 0) = \Delta u(\mathbf{x}, 0) + c(\mathbf{x})u(\mathbf{x}, 0) = \Delta p(\mathbf{x}) + c(\mathbf{x})p(\mathbf{x}) \text{ for all } \mathbf{x} \in \Omega. \quad (4.6)$$

Recall the assumption that $|p(\mathbf{x})| > 0$ for $\mathbf{x} \in \overline{\Omega}$. Due to (4.6)

$$c(\mathbf{x}) = \frac{v(\mathbf{x}, 0) - \Delta p(\mathbf{x})}{p(\mathbf{x})} \text{ for all } \mathbf{x} \in \Omega. \quad (4.7)$$

Plugging $c(\mathbf{x})$, computed in (4.7), into (4.5) gives

$$v_t(\mathbf{x}, t) = \Delta v(\mathbf{x}, t) + \frac{v(\mathbf{x}, 0) - \Delta p(\mathbf{x})}{p(\mathbf{x})} v(\mathbf{x}, t) \text{ for all } (\mathbf{x}, t) \in \Omega \times (0, T). \quad (4.8)$$

Equation (4.8) is nonlinear and nonlocal. A theory to solve it is not yet available. We propose the following dimensional reduction approach to solve it in an approximation context.

Remark 4.2.1. *The change of variable in* (4.4) *and the elimination of* c *to derive equation* (4.8) *were adopted in [70, 75].*

For each $n \in \mathbb{N}$, define $\phi_n(t) = t^{n-1}e^t$ for all $t \in (0, T)$ and $\Phi_n(x) = x^{n-1}e^x$ for all $x \in (-R, R)$. The sets $\{\phi_n\}_{n\geq 1}$ and $\{\Phi_n\}_{n\geq 1}$ are complete in $L^2(0, T)$ and $L^2(-R, R)$ respectively. Applying the Gram-Schmidt orthonormalization process on these two sets, we obtain orthonormal bases $\{\psi_n\}$ and $\{\Psi_n\}$ of $L^2(0, T)$ and $L^2(-R, R)$, respectively. For each multi-index $\mathbf{n} = (n_1, \ldots, n_{d-1}, n_t) \in \mathbb{N}^d$, define the d-dimensional tensor-valued function $\mathbf{P_n}$ as

$$\mathbf{P_n}(\mathbf{x}', t) = \Psi_{n_1}(x_1) \ldots \Psi_{n_{d-1}}(x_{d-1})\psi_{n_t}(t)$$

for all $\mathbf{x}' = (x_1, \ldots, x_{d-1}) \in (-R, R)^{d-1}, t \in (0, T)$. It is obvious that the set $\{\mathbf{P_n} : \mathbf{n} \in \mathbb{N}^d\}$ is an orthonormal basis of the space $L^2(\Omega' \times (0, T))$. We name this basis the polynomial-exponential basis. The 1D version of the polynomial-exponential basis was introduced in [48], and the higher dimension version was defined in [74].

Remark 4.2.2. *The one-dimensional version of the polynomial-exponential basis was*

employed to solve a list of inverse problems, including nonlinear inverse problems with simulated and experimental data [42, 43, 44, 56, 58, 70, 75] and linear inverse problems [59, 72, 75, 85].

From now on, for all $\mathbf{x} \in \Omega$ we write $\mathbf{x} = (\mathbf{x}', z) \in \Omega' \times \mathbb{R}$, where $\mathbf{x}' \in \Omega' := (-R, R)^{d-1}$ consists of the first $d-1$ coordinates and $z \in (-R, R)$ is the last coordinate of $\mathbf{x}$. Then, by expanding the function $v(\mathbf{x}', z, t)$ using the basis $\{\mathbf{P}_\mathbf{n} : \mathbf{n} \in \mathbb{N}^d\}$, we can approximate the function $v(\mathbf{x}', z, t)$ as follows

$$\begin{aligned} v(\mathbf{x}', z, t) &= \sum_{\mathbf{n}\in\mathbb{N}^d} v_\mathbf{n}(z)\mathbf{P}_\mathbf{n}(\mathbf{x}', t) \simeq \sum_{\mathbf{n}\leqq\mathbf{N}} v_\mathbf{n}(z)\mathbf{P}_\mathbf{n}(\mathbf{x}', t) \\ &= \sum_{n_1=1}^{N_1} \cdots \sum_{n_{d-1}=1}^{N_{d-1}} \sum_{n_t=1}^{N_t} v_{(n_1,\ldots,n_{d-1},n_t)}(z)\Psi_{n_1}(x_1)\ldots\Psi_{n_{d-1}}(x_{d-1})\psi_{n_t}(t) \end{aligned} \tag{4.9}$$

for $(\mathbf{x}', z, t) \in \Omega' \times (-R, R) \times (0, T)$, where $\mathbf{N} = (N_1, \ldots, N_{d-1}, N_t)$ represents a cut-off vector and

$$v_\mathbf{n}(z) = \int_{\Omega'\times(0,T)} v(\mathbf{x}', z, t)\mathbf{P}_\mathbf{n}(\mathbf{x}', t)d\mathbf{x}'dt. \tag{4.10}$$

The values of the cut-off numbers $N_1, \ldots, N_{d-1}$, and N_t will be chosen based on the given data in (4.3). See Section 4.5.2 and Figure 4.1 for an illustration of a suitable choice of these numbers. In (4.9) and hereafter, we understand $\mathbf{n} \leqq \mathbf{N}$ by the statement that

$$\begin{gathered} \mathbf{n} = (n_1, \ldots, n_{d-1}, n_t) \leqq \mathbf{N} = (N_1, \ldots, N_{d-1}, N_t) \\ \text{is equivalent to} \\ 1 \leq n_1 \leq N_1, \ldots, 1 \leq n_{d-1} \leq N_{d-1}, \text{ and } 1 \leq n_t \leq N_t. \end{gathered} \tag{4.11}$$

We assume that the approximation (4.9) is valid. Plugging (4.9) into (4.8) gives

$$\begin{aligned}
&\sum_{\mathbf{n}\leqq\mathbf{N}} v_{\mathbf{n}}(z)\frac{\partial \mathbf{P}_{\mathbf{n}}(\mathbf{x}',t)}{\partial t} \\
&\qquad = \sum_{\mathbf{n}\leqq\mathbf{N}} v_{\mathbf{n}}''(z)\mathbf{P}_{\mathbf{n}}(\mathbf{x}',t) + \sum_{\mathbf{n}\leqq\mathbf{N}} v_{\mathbf{n}}(z)\Delta_{\mathbf{x}'}\mathbf{P}_{\mathbf{n}}(\mathbf{x}',t) \\
&\qquad + \frac{1}{p(\mathbf{x})}\Big(\sum_{\mathbf{n}\leqq\mathbf{N}} v_{\mathbf{n}}(z)\mathbf{P}_{\mathbf{n}}(\mathbf{x}',0) - \Delta p(\mathbf{x})\Big)\sum_{\mathbf{n}\leqq\mathbf{N}} v_{\mathbf{n}}(z)\mathbf{P}_{\mathbf{n}}(\mathbf{x}',t)
\end{aligned} \tag{4.12}$$

for all $(\mathbf{x}', z, t) \in \Omega' \times (-R, R) \times (0, T)$. For each multi-index $\mathbf{m} \leqq \mathbf{N}$, we multiply $\mathbf{P}_{\mathbf{m}}(\mathbf{x}', t)$ to both sides of (4.12), and then integrate the resulting equation over $\Omega' \times (0, T)$ to get

$$\begin{aligned}
&\sum_{\mathbf{n}\leqq\mathbf{N}} v_{\mathbf{n}}(z)\int_{\Omega'\times(0,T)} \frac{\partial \mathbf{P}_{\mathbf{n}}(\mathbf{x}',t)}{\partial t}\mathbf{P}_{\mathbf{m}}(\mathbf{x}',t)d\mathbf{x}'dt \\
&\qquad = \sum_{\mathbf{n}\leqq\mathbf{N}} v_{\mathbf{n}}''(z)\int_{\Omega'\times(0,T)} \mathbf{P}_{\mathbf{n}}(\mathbf{x}',t)\mathbf{P}_{\mathbf{m}}(\mathbf{x}',t)d\mathbf{x}'dt \\
&\qquad + \sum_{\mathbf{n}\leqq\mathbf{N}} v_{\mathbf{n}}(z)\int_{\Omega'\times(0,T)} \Delta_{\mathbf{x}'}\mathbf{P}_{\mathbf{n}}(\mathbf{x}',t)\mathbf{P}_{\mathbf{m}}(\mathbf{x}',t)d\mathbf{x}'dt \\
&\qquad + \frac{1}{p(\mathbf{x})}\Big(\sum_{\mathbf{n}\leqq\mathbf{N}} v_{\mathbf{n}}(z)\mathbf{P}_{\mathbf{n}}(\mathbf{x}',0) - \Delta p(\mathbf{x})\Big) \\
&\qquad \times \int_{\Omega'\times(0,T)} \sum_{\mathbf{n}\leqq\mathbf{N}} v_{\mathbf{n}}(z)\mathbf{P}_{\mathbf{n}}(\mathbf{x}',t)\mathbf{P}_{\mathbf{m}}(\mathbf{x}',t)d\mathbf{x}'dt
\end{aligned} \tag{4.13}$$

for all $z \in (-R, R)$. Defining

$$s_{\mathbf{mn}} = -\int_{\Omega'\times(0,T)} \frac{\partial \mathbf{P}_{\mathbf{n}}(\mathbf{x}',t)}{\partial t}\mathbf{P}_{\mathbf{m}}(\mathbf{x}',t)d\mathbf{x}'dt + \int_{\Omega'\times(0,T)} \Delta_{\mathbf{x}'}\mathbf{P}_{\mathbf{n}}(\mathbf{x}',t)\mathbf{P}_{\mathbf{m}}(\mathbf{x}',t)d\mathbf{x}'dt$$

and

$$\mathbf{F}_{\mathbf{m}}([v_{\mathbf{n}}(z)]_{\mathbf{n}\leqq\mathbf{N}}) = \frac{1}{p(\mathbf{x})}\Big(\sum_{\mathbf{n}\leqq\mathbf{N}} v_{\mathbf{n}}(z)\mathbf{P}_{\mathbf{n}}(\mathbf{x}',0) - \Delta p(\mathbf{x})\Big)v_{\mathbf{m}}(z), \tag{4.14}$$

we obtain from (4.13) that

$$v_{\mathbf{m}}''(z) + \sum_{\mathbf{n}\leqq\mathbf{N}} s_{\mathbf{mn}}v_{\mathbf{n}}(z) + \mathbf{F}_{\mathbf{m}}([v_{\mathbf{n}}(z)]_{\mathbf{n}\leqq\mathbf{N}}) = 0 \tag{4.15}$$

for all $z \in (-R, R)$ and for all $\mathbf{m} \leqq \mathbf{N}$, see (4.11) for the definition of $\leqq$. Coupling

all equations (4.15) for $\mathbf{m} \leqq \mathbf{N}$ forms a system second-order ordinary differential equations for the d-dimensional valued tensor $\mathbf{v}(z) = [v_{\mathbf{n}}(z)]_{\mathbf{n}\leqq\mathbf{N}}$, $z \in (-R, R)$. The Cauchy boundary conditions for the tensor $\mathbf{v}$ can be derived from (4.3), (4.4), and (4.10), read as

$$\mathbf{v}(\pm R) = [v_{\mathbf{n}}(\pm R)]_{\mathbf{n}\leqq\mathbf{N}} = \Big[\int_{\Omega'\times(0,T)} f_t(\mathbf{x}', \pm R, t)\mathbf{P}_{\mathbf{n}}(\mathbf{x}', t)dt\Big]_{\mathbf{n}\leqq\mathbf{N}} \tag{4.16}$$

and

$$\mathbf{v}'(\pm R) = [v'_{\mathbf{n}}(\pm R)]_{\mathbf{n}\leqq\mathbf{N}} = \Big[\int_{\Omega'\times(0,T)} g_t(\mathbf{x}', \pm R, t)\mathbf{P}_{\mathbf{n}}(\mathbf{x}', t)dt\Big]_{\mathbf{n}\leqq\mathbf{N}}. \tag{4.17}$$

Combining (4.15), (4.16), and (4.17), we obtain a system of Cauchy problems for $\mathbf{v} = [v_{\mathbf{n}}(z)]_{\mathbf{n}\leqq\mathbf{N}}$

$$\begin{cases} v''_{\mathbf{m}}(z) + \sum_{\mathbf{n}\leqq\mathbf{N}} s_{\mathbf{mn}} v_{\mathbf{n}}(z) + \mathbf{F}_{\mathbf{m}}(\mathbf{v}) = 0 & z \in (-R, R), \\ v_{\mathbf{m}}(z) = P_{\mathbf{m}}(z) & z = \pm R, \\ v'_{\mathbf{m}}(z) = Q_{\mathbf{m}}(z) & z = \pm R, \end{cases} \qquad \text{for } \mathbf{m} \leqq \mathbf{N}, \tag{4.18}$$

where

$$P_{\mathbf{m}}(z) = \int_{\Omega'\times(0,T)} f_t(\mathbf{x}', z, t)\mathbf{P}_{\mathbf{m}}(\mathbf{x}', t)d\mathbf{x}'dt, \tag{4.19}$$

$$Q_{\mathbf{m}}(z) = \int_{\Omega'\times(0,T)} g_t(\mathbf{x}', z, t)\mathbf{P}_{\mathbf{m}}(\mathbf{x}', t)d\mathbf{x}'dt. \tag{4.20}$$

Introduce the "tensor multiplication" operator

$$\mathcal{S} :: \mathbf{v} = \Big[\sum_{\mathbf{n}\leqq\mathbf{N}} s_{\mathbf{mn}} v_{\mathbf{n}}\Big]_{\mathbf{m}\leqq\mathbf{N}}$$

and the notations

$$\mathcal{F}(\mathbf{v}) = [\mathbf{F}_{\mathbf{m}}(\mathbf{v})]_{\mathbf{m}\leqq\mathbf{N}},$$

$$\mathcal{P}(z) = [P_{\mathbf{m}}(z)]_{\mathbf{m}\leqq\mathbf{N}}, \quad z = \pm R,$$

$$\mathcal{Q}(z) = [Q_{\mathbf{m}}(z)]_{\mathbf{m}\leqq\mathbf{N}}, \quad z = \pm R.$$

We shorten the coupling system in (4.18) as

$$\begin{cases} \mathbf{v}''(z) + \mathcal{S} :: \mathbf{v}(z) + \mathcal{F}(\mathbf{v}(z)) = 0 & z \in (-R, R), \\ \mathbf{v}(z) = \mathcal{P}(z) & z = \pm R, \\ \mathbf{v}'(z) = \mathcal{Q}(z) & z = \pm R. \end{cases} \tag{4.21}$$

Remark 4.2.3. *Computing the values of* $\mathbf{v}$ *and* $\mathbf{v}'$ *at* $z = \pm R$ *in* (4.16), (4.17), *and* (4.21) *requires us to differentiate the given data* f *and* g *with respect to the time* t. *This task is not trivial, especially when the data are corrupted by noise. We employ the new differentiating technique in [74], in which we approximate the data by eliminating their high-frequency terms from the Fourier expansion of the given data with respect to the polynomial-exponential basis before differentiating. It was numerically shown in [74] that computing derivatives using this new technique is more accurate than the conventional ones; say the finite difference, the cubic spline, and the Tikhonov optimization methods.*

Remark 4.2.4. *The first key point of our dimension reduction approach lies in the derivation of the approximation model* (4.21), *a system of first-order ODEs along the* $z-$*axis. The approximation model* (4.21) *involves*

$$|\mathbf{N}| = |(N_1, \ldots, N_{d-1}, N_t)| = N_t \prod_{i=1}^{d-1} N_i \tag{4.22}$$

equations versus the same numbers of unknown entries of $\mathbf{v} = [v_{\mathbf{m}}]_{\mathbf{m} \leqq \mathbf{N}}$. *This allows for the computation of the tensor-valued function* $\mathbf{v}(z)$ *for* $z \in (-R, R)$, *and subsequently the function* $v(\mathbf{x}', z, t)$ *for all* $(\mathbf{x}', z, t) \in \Omega' \times (-R, R) \times (0, T)$. *The solution* $c(\mathbf{x})$, $\mathbf{x} \in \Omega$, *to Problem 4.1.1 can be computed via the knowledge of* v *and the reconstruction formula* (4.7). *However, this convenience comes with a trade-off. The truncation in* (4.8) *makes system* (4.21) *not exact. It should be considered as an approximation context for Problem 4.1.1. Studying the behavior of* (4.21) *when all cut-off numbers* $N_2, \ldots, N_d, N_t$ *tend towards* ∞ *presents a significant challenge. We*

do not cover this complex topic, which prioritizes computational aspects. In exchange, we will show that our dimension reduction method is acceptable in numerics. It can quickly deliver reliable solutions since we have transferred a high dimensional problem into a problem along the $z-$axis, which is a 1D problem.

As noted in Remark 4.2.4, once the system of ODEs in (4.21) with Cauchy boundary data is solved, the computed solution to Problem 4.1.1 follows. However, this task is challenging since (4.21) is nonlinear. There are several methods to solve nonlinear systems of ODEs. The conventional approach is based on optimization. For example, one can solve (4.21) by minimizing the least squares cost functional

$$J_{\text{lsq}}(\mathbf{v}) = \int_{-R}^{R} \left|\mathbf{v}''(z) + \mathcal{S} :: \mathbf{v} + \mathcal{F}(\mathbf{v})\right|^2 dz + \text{a regularization term} \tag{4.23}$$

subject to the endpoint condition in (4.21) and then accepting the minimizer as the computed solution. This method is effective when a good initial guess of (4.21) is given because J_{lsq} might have multiple local minima. The challenge is that such an initial guess is not always available in practical applications. Consequently, the optimization approach is not deemed suitable for solving (4.21). There are three approaches to solve (4.21) without requesting a good initial guess, all based on Carleman estimates.

1. *The Carleman convexification method.* The key of the Carleman convexification method is to include a Carleman weight function; e.g., $W_\lambda(z) = e^{-\lambda z}$, $\lambda > 1$, to the least squares cost functional in (4.23). That means one can minimize the Carleman weighted functional

$$J_{\text{conv}}(\mathbf{v}) = \int_{-R}^{R} W_\lambda(z)\left|\mathbf{v}''(z) + \mathcal{S} :: \mathbf{v} + \mathcal{F}(\mathbf{v})\right|^2 dz + \text{a regularization term},$$

subject to the boundary conditions in (4.21) where $\mathbf{v} = [v_{\mathbf{m}}]_{\mathbf{m} \leqq \mathbf{N}}$. One can prove that J_{conv} is uniformly convex in any bounded subset of the functional space containing the desired solution provided that λ is sufficiently large. Also, the unique minimizer is close to the true solution to (4.21). The original con-

vexification method was first introduced in [49], with subsequent results found in [6, 44, 50, 58]. Despite its efficacy in producing reliable numerical solutions, the convexification method has a high computational cost.

2. *The Carleman contraction method.* The contraction method for solving (4.21) primarily starts with an initial function $\mathbf{v}^{(0)} = [v^{(0)}_{\mathbf{m}}]_{\mathbf{m}\leqq\mathbf{N}}$. Note that $\mathbf{v}^{(0)}$ might be far away from the true solution to (4.21). From this point, given that $\mathbf{v}^{(k)} = [v^{(k)}_{\mathbf{m}}]_{\mathbf{m}\leqq\mathbf{N}}$, $k \geq 0$, is known, we compute $\mathbf{v}^{(k+1)} = [v^{(k+1)}_{\mathbf{m}}]_{\mathbf{m}\leqq\mathbf{N}}$ as the "Carleman-regularized" solution to

$$\begin{cases} \mathbf{v}^{(k+1)''}(z) + \mathcal{S} :: \mathbf{v}^{(k+1)}(z) + \mathcal{F}(\mathbf{v}^{(k)}(z)) = 0 & z \in (-R, R), \\ \mathbf{v}(z) = \mathcal{P}(z) & z = \pm R, \\ \mathbf{v}'(z) = \mathcal{Q}(z) & z = \pm R. \end{cases} \tag{4.24}$$

By Carleman-regularized solution, we mean $\mathbf{v}^{(k+1)}$ is the minimizer of

$$J^{(k)}(\mathbf{v}) = \int_{-R}^{R} W_\lambda(z)\left|\mathbf{v}''(z) + \mathcal{S} :: \mathbf{v} + \mathcal{F}(\mathbf{v}^{(k)})\right|^2 dz + \text{a regularization term}$$

subject to the boundary conditions in (4.21). The choice of λ, $W_\lambda(z)$, and the regularization term will be specified later. The procedure to compute $\mathbf{v}^{(k+1)}$ above involves the combination of the quasi-reversibility method [53] and an appropriate Carleman estimated, as in [55, 57, 71]. Thanks to the presence of the Carleman weight function $W_\lambda(z)$, one can follow the arguments in [55, 57, 71] to prove the convergence of the constructed sequence $\left\{\mathbf{v}^{(k)}\right\}_{k\geq 0}$ to the true solution to (4.21).

3. *The Carleman-Newton method.* The Carleman-Newton method is similar to the Carleman contraction method. Given an initial solution $\mathbf{v}^{(0)}$ that can be chosen arbitrary, we find $\mathbf{v}^{(1)}$ as the Carleman regularized solution to the linearization of (4.21) about $\mathbf{v}^{(0)}$. We refer the reader to [1, 60] for details and the rigorous proof of the convergence due to the Carleman-Newton method.

Among the three methods mentioned above, we will choose the second approach; i.e., we will establish a 1D analog of the Carleman contraction method to solve (4.21). This choice is appropriate due to the global convergence, the rapid rate of convergence, and the simplicity of the computational implementation. In the previous two sentences, we mentioned "analog" because $\mathcal{F}$ does not satisfy the Lipschitz condition in [71], which requires some modification in analysis.

In the next section, we establish a Carleman estimate, which plays an important role in proving the convergence of the Carleman contraction method.

4.3 A 1D-Carleman Estimate

Let $z_0 < -R$ be a fixed number. We have the lemma.

Lemma 4.3.1. *There is a number $\lambda_0 > 1$ and a constant $C > 0$ depending only on R and z_0 such that for all functions $w \in C^2([-R, R])$, we have*

$$\begin{aligned}\int_{-R}^{R} e^{2\lambda(z-z_0)^{-2}}|w''(z)|^2dz \geq & -Ce^{2\lambda(R-z_0)^{-2}}(\lambda^3|w(R)|^2 + \lambda|w'(R)|^2)\\ & - Ce^{2\lambda(-R-z_0)^{-2}}(\lambda^3|w(-R)|^2 + \lambda|w'(-R)|^2)\\ & + C\lambda^3\int_{-R}^{R} e^{2\lambda(z-z_0)^{-2}}|w(z)|^2dz\\ & + C\lambda\int_{-R}^{R} e^{2\lambda(z-z_0)^{-2}}|w'(z)|^2dz\end{aligned} \tag{4.25}$$

provided that $\lambda \geq \lambda_0$.

Proof. Step 1. Define

$$y(z) = e^{\lambda(z-z_0)^{-2}}w(z) \text{ or equivalently } w(z) = e^{-\lambda(z-z_0)^{-2}}y(z) \tag{4.26}$$

for all $z \in [-R, R]$. We have

$$w'(z) = e^{-\lambda(z-z_0)^{-2}}\left[2\lambda(z-z_0)^{-3}y(z) + y'(z)\right] \tag{4.27}$$

and

$$w''(z) = e^{-\lambda(z-z_0)^{-2}} \left[2\lambda(z-z_0)^{-6}[2\lambda - 3(z-z_0)^2]y(z) + 4\lambda(z-z_0)^{-3}y'(z) + y''(z)\right] \tag{4.28}$$

for all $z \in [-R, R]$. Thus,

$$\begin{aligned} & e^{2\lambda(z-z_0)^{-2}}|w''(z)|^2 \\ &\qquad = \left[2\lambda(z-z_0)^{-6}[2\lambda - 3(z-z_0)^2]y(z) + 4\lambda(z-z_0)^{-3}y'(z) + y''(z)\right]^2 \\ &\qquad \geq 16\lambda^2(z-z_0)^{-9}[2\lambda - 3(z-z_0)^2]y(z)y'(z) + 8\lambda(z-z_0)^{-3}y'(z)y''(z) \\ &\qquad = 8\lambda^2(z-z_0)^{-9}[2\lambda - 3(z-z_0)^2]\frac{d}{dz}|y(z)|^2 + 4\lambda(z-z_0)^{-3}\frac{d}{dz}|y'(z)|^2 \end{aligned}$$

for all $z \in [-R, R]$. Here, we have used the inequality $(a+b+c)^2 \geq 2ab + 2bc$. Thus,

$$\begin{aligned} & (z-z_0)^8 e^{2\lambda(z-z_0)^{-2}}|w''(z)|^2 \\ &\qquad \geq 8\lambda^2(z-z_0)^{-1}[2\lambda - 3(z-z_0)^2]\frac{d}{dz}|y(z)|^2 + 4\lambda(z-z_0)^5\frac{d}{dz}|y'(z)|^2 \end{aligned} \tag{4.29}$$

for all $z \in [-R, R]$. By the product rule in differentiation $ab' = (ab)' - a'b$, we have

$$\begin{aligned} & (z-z_0)^8 e^{2\lambda(z-z_0)^{-2}}|w''(z)|^2 \\ &\qquad \geq \frac{d}{dz}\left[8\lambda^2(z-z_0)^{-1}[2\lambda - 3(z-z_0)^2]|y(z)|^2\right] \\ &\qquad - |y(z)|^2\frac{d}{dz}\left[8\lambda^2(z-z_0)^{-1}[2\lambda - 3(z-z_0)^2]\right] \\ &\qquad + \frac{d}{dz}\left[4\lambda(z-z_0)^5|y'(z)|^2\right] - |y'(z)|^2\frac{d}{dz}\left[4\lambda(z-z_0)^5\right] \end{aligned} \tag{4.30}$$

for all $z \in [-R, R]$. Rearranging terms in (4.30) and simplifying the resulting inequality, we get

$$\begin{aligned} & (z-z_0)^8 e^{2\lambda(z-z_0)^{-2}}|w''(z)|^2 \\ &\qquad \geq \frac{d}{dz}\left[8\lambda^2(z-z_0)^{-1}[2\lambda - 3(z-z_0)^2]|y(z)|^2 + 4\lambda(z-z_0)^5|y'(z)|^2\right] \\ &\qquad + \left[16\lambda^3(z-z_0)^{-2} + 24\lambda^2\right]|y(z)|^2 - 20\lambda|y'(z)|^2(z-z_0)^4 \end{aligned} \tag{4.31}$$

for all $z \in [-R, R]$. Integrating (4.31) over $[-R, R]$ and noting that $\lambda^3 \gg \lambda^2 \gg \lambda$ as λ gets large, we can find a number $\lambda_0 > 1$ and a generic constant $C > 0$, both of which depend only on z_0 and R, such that

$$\begin{aligned}\int_{-R}^{R} e^{2\lambda(z-z_0)^{-2}}|w''(z)|^2dz& \\ &\geq -C(\lambda^3|y(R)|^2 + \lambda|y'(R)|^2) - C(\lambda^3|y(-R)|^2 + \lambda|y'(-R)|^2) \\ &+ C\lambda^3\int_{-R}^{R}|y(z)|^2dz - C\lambda\int_{-R}^{R}|y'(z)|^2dz.\end{aligned} \tag{4.32}$$

for all $\lambda \geq \lambda_0$.

Step 2. Recall from (4.26) that $y(z) = e^{\lambda(z-z_0)^{-2}}w(z)$. We have

$$y'(z) = e^{\lambda(z-z_0)^{-2}}[-2\lambda(z-z_0)^{-3}w(z) + w'(z)].$$

Thus, by the inequality $-(a+b)^2 \geq -2(a^2+b^2)$, we have

$$-|y'(z)|^2 \geq -2e^{2\lambda(z-z_0)^{-2}}\left[4\lambda^2(z-z_0)^{-6}|w(z)|^2 + |w'(z)|^2\right] \tag{4.33}$$

for all $z \in [-R, R]$. Combining (4.32) and (4.33) and recalling that C is a generic constant depending only on z_0 and R, we have

$$\begin{aligned}\int_{-R}^{R} e^{2\lambda(z-z_0)^{-2}}|w''(z)|^2dz& \\ &\geq -Ce^{2\lambda(R-z_0)^{-2}}(\lambda^3|w(R)|^2 + \lambda|w'(R)|^2) \\ &- Ce^{2\lambda(-R-z_0)^{-2}}(\lambda^3|w(-R)|^2 + \lambda|w'(-R)|^2) \\ &+ C\lambda^3\int_{-R}^{R}e^{2\lambda(z-z_0)^{-2}}|w(z)|^2dz - C\lambda\int_{-R}^{R}e^{2\lambda(z-z_0)^{-2}}|w'(z)|^2dz.\end{aligned} \tag{4.34}$$

Step 3. Using the inequality $2ab \leq a^2 + b^2$, we have

$$\begin{aligned}\int_{-R}^{R} e^{2\lambda(z-z_0)^{-2}}\frac{d}{dz}|w'(z)|^2dz &= 2\int_{-R}^{R}e^{2\lambda(z-z_0)^{-2}}w'(z)w''(z)dz \\ &\leq \int_{-R}^{R}e^{2\lambda(z-z_0)^{-2}}|w'(z)|^2dz + \int_{-R}^{R}e^{2\lambda(z-z_0)^{-2}}|w''(z)|^2dz.\end{aligned}$$

Thus, recalling that $ab' = (ab)' - ba'$, we have

$$\begin{aligned}
&\int_{-R}^{R} e^{2\lambda(z-z_0)^{-2}}|w''(z)|^2dz \\
&\qquad \geq \int_{-R}^{R} e^{2\lambda(z-z_0)^{-2}}\frac{d}{dz}|w'(z)|^2dz - \int_{-R}^{R} e^{2\lambda(z-z_0)^{-2}}|w'(z)|^2dz \\
&\qquad = \int_{-R}^{R} \frac{d}{dz}\Big[e^{2\lambda(z-z_0)^{-2}}|w'(z)|^2\Big]dz - \int_{-R}^{R} |w'(z)|^2\frac{d}{dz}e^{2\lambda(z-z_0)^{-2}}dz \\
&\qquad - \int_{-R}^{R} e^{2\lambda(z-z_0)^{-2}}|w'(z)|^2dz.
\end{aligned}$$

As a result,

$$\begin{aligned}
&\int_{-R}^{R} e^{2\lambda(z-z_0)^{-2}}|w''(z)|^2dz \\
&\quad \geq -C\left[e^{2\lambda(R-z_0)^{-2}}|w'(R)|^2 + e^{2\lambda(-R-z_0)^{-2}}|w'(-R)|^2\right] \\
&\quad + 2\lambda\int_{-R}^{R}(z-z_0)^{-3}e^{2\lambda(z-z_0)^{-2}}|w'(z)|^2dz - \int_{-R}^{R} e^{2\lambda(z-z_0)^{-2}}|w'(z)|^2dz.
\end{aligned} \tag{4.35}$$

Adding (4.34) and (4.35) and recalling that $\lambda \geq \lambda_0 \gg 1$, we obtain (4.25).

□

4.4 A Picard-like iteration to solve (4.21)

In this section, we employ the Carleman estimate in Lemma 4.3.1 to construct a sequence that converges to the solution to (4.21), provided that this true solution exists. We consider the circumstance that the boundary data $\mathcal{P}$ and $\mathcal{Q}$ of (4.21) contain noise. Let $\mathcal{P}^*$ and $\mathcal{Q}^*$ be the unknown exact values of the boundary data $\mathcal{P}$ and $\mathcal{Q}$, respectively. Let $\mathbf{v}^*$ be the solution to (4.21) with $\mathcal{P}$ and $\mathcal{Q}$ being replaced by $\mathcal{P}^*$ and $\mathcal{Q}^*$, respectively. That means, $\mathbf{v}^*$ solves

$$\begin{cases}
\mathbf{v}^{*\prime\prime}(z) + \mathcal{S} :: \mathbf{v}^*(z) + \mathcal{F}(\mathbf{v}^*(z)) = 0 & z \in (-R, R), \\
\mathbf{v}^*(z) = \mathcal{P}^*(z) & z = \pm R, \\
\mathbf{v}^{*\prime}(z) = \mathcal{Q}^*(z) & z = \pm R.
\end{cases} \tag{4.36}$$

In this section, we assume the existence of the solution $\mathbf{v}^*$ to (4.36). We now consider the case when noise is introduced to the data. Let $\delta > 0$ be the noise level. That

means,

$$\max_{z\in\{-R,R\}} \left\{|\mathcal{P}(z)-\mathcal{P}^*(z)|, |\mathcal{Q}(z)-\mathcal{Q}^*(z)|\right\} < \delta. \tag{4.37}$$

Remark 4.4.1 (Noise model)**.** *In this section, for simplicity, we assume that noise is introduced into the indirect data $\mathcal{P}(\pm R)$ and $\mathcal{Q}(\pm R)$ as in* (4.37) *rather than to the direct data, f and g. This assumption serves theoretical purposes only. In our computational study, we study the more realistic case where the direct data f^* and g^* are impacted by noise as in* (4.63) *and* (4.64)*. Recall that the entries $P_{\mathbf{m}}(\pm R)$ and $Q_{\mathbf{m}}(\pm R)$ of indirect data $\mathcal{P}(\pm R)$ and $\mathcal{Q}(\pm R)$ are computed by the knowledge of the derivatives of f and g via* (4.19) *and* (4.20)*. Given that differentiating noisy data presents significant challenges and can greatly amplify errors, even minor noise in f and g can lead to substantial inaccuracies in $P_{\mathbf{m}}(\pm R)$ and $Q_{\mathbf{m}}(\pm R)$. To address this issue, we employ a novel differentiation approach as presented in [74], in which the data f and g are replaced by appropriately truncated Fourier expansions with respect to a special basis of L^2. The primary goal of this truncation is to eliminate the high-frequency oscillatory components of the noise, thereby enhancing the stability of the differentiation process. This method has been demonstrated to have superior stability compared to traditional methods like finite difference, cubic splines, or the Tikhonov regularization technique, see [74] for more details.*

Consider the space of admissible solutions

$$H = \left\{\boldsymbol{\varphi} = [\varphi_{\mathbf{m}}]_{\mathbf{m}\leqq\mathbf{N}} : \varphi_{\mathbf{m}} \in H^2(-R,R) \text{ for all } \mathbf{m}\leqq\mathbf{N}\right\} = H^2(-R,R)^{|\mathbf{N}|}$$

where $|\mathbf{N}|$ is as in (4.22). Fix an arbitrary large number $M>0$, define the closed ball in H

$$B_M = \{\boldsymbol{\varphi} : \|\boldsymbol{\varphi}\|_{H^2(-R,R)^{|\mathbf{N}|}} \leq M\}. \tag{4.38}$$

For each $\mathbf{v} \in B_M$, define the functional

$$\begin{aligned} J_{\mathbf{v}}^{(\lambda,\epsilon)}(\boldsymbol{\varphi}) = &\int_{-R}^{R} e^{2\lambda(z-z_0)^{-2}} \left| \boldsymbol{\varphi}'' + \mathcal{S} :: \boldsymbol{\varphi} + \mathcal{F}(\mathbf{v}) \right|^2 dz \\ &+ \lambda^4 e^{2\lambda(R-z_0)^{-2}} \left| \boldsymbol{\varphi}(R) - \mathcal{P}(R) \right|^2 + \lambda^4 e^{2\lambda(-R-z_0)^{-2}} \left| \boldsymbol{\varphi}(-R) - \mathcal{P}(-R) \right|^2 \\ &+ \lambda^4 e^{2\lambda(R-z_0)^{-2}} \left| \boldsymbol{\varphi}'(R) - \mathcal{Q}(R) \right|^2 + \lambda^4 e^{2\lambda(-R-z_0)^{-2}} \left| \boldsymbol{\varphi}'(-R) - \mathcal{Q}(-R) \right|^2 \\ &+ \epsilon \|\boldsymbol{\varphi}\|^2_{H^2(-R,R)^{|\mathbf{N}|}} \end{aligned} \tag{4.39}$$

for all $\boldsymbol{\varphi}$ where $\lambda \geq \lambda_0$ and $\epsilon > 0$ will be chosen later. For all $\mathbf{v} \in B_M$, the functional $J_{\mathbf{v}}^{(\lambda,\epsilon)}$ is uniformly convex in the closed and convex set B_M of H. It has a unique minimizer. We define the map $\Phi^{(\lambda,\epsilon)} : B_M \to B_M$ that sends $\mathbf{v}$ to such a minimizer. More precisely,

$$\Phi^{(\lambda,\epsilon)}(\mathbf{v}) = \underset{\varphi \in B_M}{\arg\min}\, J_{\mathbf{v}}^{(\lambda,\epsilon)}(\boldsymbol{\varphi}) \text{ for all } \mathbf{v} \in B_M. \tag{4.40}$$

We define the sequence $\{\mathbf{v}^{(k)}\}_{k\geq 0}$ as follows:

$$\begin{cases} \mathbf{v}^{(0)} \text{ chosen arbitrarily in } B_M \\ \mathbf{v}^{(k+1)} = \Phi^{(\lambda,\epsilon)}(\mathbf{v}^{(k)}) \quad k \geq 0. \end{cases} \tag{4.41}$$

The following theorem guarantees the convergence of the sequence $\{\mathbf{v}^{(k)}\}_{k\geq 0}$ to $\mathbf{v}^*$.

Theorem 4.4.1. *Let M be a large number such that both $\mathbf{v}^*$ and $\mathbf{v}^{(0)}$ are in B_M. Let λ_0 be the number in Lemma 4.3.1. Then, there exists $\lambda_1 > \lambda_0$ depending only on M,*

p, N, R, and $[\mathbf{P}_{\mathbf{m}\leq\mathbf{N}}]$ *such that*

$$\begin{aligned}\int_{-R}^{R} e^{2\lambda(z-z_0)^{-2}}|\mathbf{v}^{(k+1)}-\mathbf{v}^*|^2dz \leq \left(\frac{C}{\lambda^3}\right)^{k+1}&\int_{-R}^{R} e^{2\lambda(z-z_0)^{-2}}|\mathbf{v}^{(0)}-\mathbf{v}^*|^2dz\\ &+\frac{C/\lambda^3}{1-C/\lambda^3}\Big[\lambda^4 e^{2\lambda(R-z_0)^{-2}}|\mathcal{P}(R)-\mathcal{P}^*(R))|^2\\ &+\lambda^4 e^{2\lambda(-R-z_0)^{-2}}|\mathcal{P}(-R)-\mathcal{P}^*(-R)|^2\\ &+\lambda^4 e^{2\lambda(R-z_0)^{-2}}|\mathcal{Q}(R)-\mathcal{Q}^*(R)|^2\\ &+\lambda^4 e^{2\lambda(-R-z_0)^{-2}}|\mathcal{Q}(-R)-\mathcal{Q}^*(-R)|^2\\ &+\epsilon\|\mathbf{v}^*\|^2_{H^2(-R,R)^{|\mathbf{N}|}}\Big]\end{aligned} \tag{4.42}$$

for all $\lambda \geq \lambda_1$, $k \geq 0$. *Here,* C *is a positive constant depending only on* R *and* z_0.

Remark 4.4.2. *Theorem 4.4.1 and its proof are stated and proved using similar arguments in [55, 57, 71]. However, we still need some important modifications:*

1. *The nonlinearity* $\mathcal{F}$ *in [55, 57, 71] needs to satisfy the Lipschitz condition. However, the function* $\mathcal{F}$ *in the current work does not meet this requirement. To address this issue, it is necessary to confine the computational domain to a bounded set* B_M *for an arbitrarily large number* M. *Within this bounded domain, the Lipschitz condition is automatically satisfied.*

2. *In [55, 57], the analysis of noise was not explored, whereas it was somewhat examined in [71]. By "somewhat," it means that in [71], a technical condition had to be imposed. The noise in the Dirichlet observations and the noise in the Neumann measurements are not independent. Specifically, it was assumed that the noise in the Dirichlet observation is the trace of a function, and the noise in the Neumann measurement needs to be the trace of that function's normal derivative. Given that this circumstance is somewhat impractical, we opt to relax it in the present research.*

Proof of Theorem 4.4.1. In the proof, we will employ the dot product

$$\boldsymbol{\varphi} \cdot \mathbf{h} = \sum_{\mathbf{m} \leqq \mathbf{N}} \varphi_{\mathbf{m}} h_{\mathbf{m}}$$

for all $\boldsymbol{\varphi} = [\varphi_{\mathbf{m}}]_{\mathbf{m} \leq \mathbf{N}}$ and $\mathbf{h} = [h_{\mathbf{m}}]_{\mathbf{m} \leq \mathbf{N}}$ in H. Fix $k \geq 0$. Set

$$\mathbf{h} = \mathbf{v}^{(k+1)} - \mathbf{v}^*.$$

Since $\mathbf{v}^{(k+1)}$ is the minimizer of $J^{\lambda,\epsilon}_{\mathbf{v}^{(k)}}$ in B_M and $\mathbf{v}^*$ is in the interior of B_M, we have

$$\begin{aligned}
&\int_{-R}^{R} e^{2\lambda(z-z_0)^{-2}} \big(\mathbf{v}^{(k+1)\prime\prime}(z) + \mathcal{S} :: \mathbf{v}^{(k+1)}(z) + \mathcal{F}(\mathbf{v}^{(k)})\big) \cdot \big(\mathbf{h}''(z) + \mathcal{S} :: \mathbf{h}(z)\big) dz \\
&\quad + \lambda^4 e^{2\lambda(R-z_0)^{-2}} (\mathbf{v}^{(k+1)}(R) - \mathcal{P}(R)) \cdot \mathbf{h}(R) \\
&\quad + \lambda^4 e^{2\lambda(-R-z_0)^{-2}} (\mathbf{v}^{(k+1)}(-R) - \mathcal{P}(-R)) \cdot \mathbf{h}(-R) \\
&\quad + \lambda^4 e^{2\lambda(R-z_0)^{-2}} (\mathbf{v}^{(k+1)\prime}(R) - \mathcal{Q}(R)) \cdot \mathbf{h}'(R) \\
&\quad + \lambda^4 e^{2\lambda(-R-z_0)^{-2}} (\mathbf{v}^{(k+1)\prime}(-R) - \mathcal{Q}(-R)) \cdot \mathbf{h}'(-R) \\
&\quad + \epsilon \langle \mathbf{v}^{(k+1)}, \mathbf{h} \rangle_{H^2(-R,R)^{|\mathbf{N}|}} \leq 0.
\end{aligned} \tag{4.43}$$

On the other hand, since $\mathbf{v}^*$ is the true solution to (4.36), we have

$$\begin{aligned}
&\int_{-R}^{R} e^{2\lambda(z-z_0)^{-2}} \left(\mathbf{v}^{*\prime\prime}(z) + \mathcal{S} :: \mathbf{v}^*(z) + \mathcal{F}(\mathbf{v}^*)\right) \cdot \left(\mathbf{h}''(z) + \mathcal{S} :: \mathbf{h}(z)\right) dz \\
&\quad + \lambda^4 e^{2\lambda(R-z_0)^{-2}} (\mathbf{v}^*(R) - \mathcal{P}^*(R)) \cdot \mathbf{h}(R) \\
&\quad + \lambda^4 e^{2\lambda(-R-z_0)^{-2}} (\mathbf{v}^*(-R) - \mathcal{P}^*(-R)) \cdot \mathbf{h}(-R) \\
&\quad + \lambda^4 e^{2\lambda(R-z_0)^{-2}} (\mathbf{v}^{*\prime}(R) - \mathcal{Q}^*(R)) \cdot \mathbf{h}'(R) \\
&\quad + \lambda^4 e^{2\lambda(-R-z_0)^{-2}} (\mathbf{v}^{*\prime}(-R) - \mathcal{Q}^*(-R)) \cdot \mathbf{h}'(-R) \\
&\quad + \epsilon \langle \mathbf{v}^*, \mathbf{h} \rangle_{H^2(-R,R)^{|\mathbf{N}|}} \\
&\quad = \epsilon \langle \mathbf{v}^*, \mathbf{h} \rangle_{H^2(-R,R)^{|\mathbf{N}|}}.
\end{aligned} \tag{4.44}$$

Subtracting (4.43) from (4.44) gives

$$\begin{aligned}
&\int_{-R}^{R} e^{2\lambda(z-z_0)^{-2}}\big(\mathbf{v}^{(k+1)''}(z)-\mathbf{v}^{*''}(z)+\mathcal{S}::(\mathbf{v}^{(k+1)}(z)-\mathbf{v}^{*''}(z))\\
&\quad+\mathcal{F}(\mathbf{v}^{(k)})-\mathcal{F}(\mathbf{v}^{*})\big)\cdot\big(\mathbf{h}''(z)+\mathcal{S}::\mathbf{h}(z)\big)dz\\
&\quad+\lambda^4 e^{2\lambda(R-z_0)^{-2}}(\mathbf{v}^{(k+1)}(R)-\mathbf{v}^{*}(R))\cdot\mathbf{h}(R)\\
&\quad+\lambda^4 e^{2\lambda(-R-z_0)^{-2}}(\mathbf{v}^{(k+1)}(-R)-\mathbf{v}^{*}(-R))\cdot\mathbf{h}(-R)\\
&\quad+\lambda^4 e^{2\lambda(R-z_0)^{-2}}(\mathbf{v}^{(k+1)'}(R)-\mathbf{v}^{*'}(R))\cdot\mathbf{h}'(R)\\
&\quad+\lambda^4 e^{2\lambda(-R-z_0)^{-2}}(\mathbf{v}^{(k+1)'}(-R)-\mathbf{v}^{*'}(-R))\cdot\mathbf{h}'(-R)\\
&\quad+\epsilon\langle\mathbf{v}^{(k+1)}-\mathbf{v}^{*},\mathbf{h}\rangle_{H^2(-R,R)^{|\mathbf{N}|}}\\
&\quad\le\lambda^4 e^{2\lambda(R-z_0)^{-2}}(\mathcal{P}(R)-\mathcal{P}^{*}(R))\cdot\mathbf{h}(R)\\
&\quad+\lambda^4 e^{2\lambda(-R-z_0)^{-2}}(\mathcal{P}(-R)-\mathcal{P}^{*}(-R))\cdot\mathbf{h}(-R)\\
&\quad+\lambda^4 e^{2\lambda(R-z_0)^{-2}}(\mathcal{Q}(R)-\mathcal{Q}^{*}(R))\cdot\mathbf{h}'(R)\\
&\quad+\lambda^4 e^{2\lambda(-R-z_0)^{-2}}(\mathcal{Q}(-R)-\mathcal{Q}^{*}(-R))\cdot\mathbf{h}'(-R)\\
&\quad-\epsilon\langle\mathbf{v}^{*},\mathbf{h}\rangle_{H^2(-R,R)^{|\mathbf{N}|}}.
\end{aligned}\tag{4.45}$$

Recalling $\mathbf{h}=\mathbf{v}^{(k+1)}-\mathbf{v}^{*}$, we have

$$\begin{aligned}
&\int_{-R}^{R} e^{2\lambda(z-z_0)^{-2}}\big|\mathbf{h}''(z)+\mathcal{S}::\mathbf{h}(z)\big|^2dz\\
&\quad+\lambda^4 e^{2\lambda(R-z_0)^{-2}}|\mathbf{h}(R)|^2+\lambda^4 e^{2\lambda(-R-z_0)^{-2}}|\mathbf{h}(-R)|^2\\
&\quad+\lambda^4 e^{2\lambda(R-z_0)^{-2}}|\mathbf{h}'(R)|^2+\lambda^4 e^{2\lambda(-R-z_0)^{-2}}|\mathbf{h}'(-R)|^2+\epsilon\|\mathbf{h}\|^2_{H^2(-R,R)^{|\mathbf{N}|}}\\
&\quad\le-\int_{-R}^{R} e^{2\lambda(z-z_0)^{-2}}\big(\mathcal{F}(\mathbf{v}^{(k)})-\mathcal{F}(\mathbf{v}^{*})\big)\cdot\big(\mathbf{h}''(z)+\mathcal{S}::\mathbf{h}(z)\big)dz\\
&\quad+\lambda^4 e^{2\lambda(R-z_0)^{-2}}(\mathcal{P}(R)-\mathcal{P}^{*}(R))\cdot\mathbf{h}(R)\\
&\quad+\lambda^4 e^{2\lambda(-R-z_0)^{-2}}(\mathcal{P}(-R)-\mathcal{P}^{*}(-R))\cdot\mathbf{h}(-R)\\
&\quad+\lambda^4 e^{2\lambda(R-z_0)^{-2}}(\mathcal{Q}(R)-\mathcal{Q}^{*}(R))\cdot\mathbf{h}'(R)\\
&\quad+\lambda^4 e^{2\lambda(-R-z_0)^{-2}}(\mathcal{Q}(-R)-\mathcal{Q}^{*}(-R))\cdot\mathbf{h}'(-R)-\epsilon\langle\mathbf{v}^{*},\mathbf{h}\rangle_{H^2(-R,R)^{|\mathbf{N}|}}.
\end{aligned}\tag{4.46}$$

Rearranging terms (4.46) and using the inequality $|ab| \leq \frac{1}{2}(a^2+b^2)$, we have

$$\begin{aligned}
&\int_{-R}^{R} e^{2\lambda(z-z_0)^{-2}} \left|\mathbf{h}''(z) + \mathcal{S} :: \mathbf{h}(z)\right|^2 dz \\
&\quad + \lambda^4 e^{2\lambda(R-z_0)^{-2}} |\mathbf{h}(R)|^2 + \lambda^4 e^{2\lambda(-R-z_0)^{-2}} |\mathbf{h}(-R)|^2 \\
&\quad + \lambda^4 e^{2\lambda(R-z_0)^{-2}} |\mathbf{h}'(R)|^2 + \lambda^4 e^{2\lambda(-R-z_0)^{-2}} |\mathbf{h}'(-R)|^2 + \epsilon \|\mathbf{h}\|^2_{H^2(-R,R)^{|\mathbf{N}|}} \\
&\quad \leq - \int_{-R}^{R} e^{2\lambda(z-z_0)^{-2}} \left|\mathcal{F}(\mathbf{v}^{(k)}) - \mathcal{F}(\mathbf{v}^*)\right|^2 dz \\
&\quad + \lambda^4 e^{2\lambda(R-z_0)^{-2}} |\mathcal{P}(R) - \mathcal{P}^*(R))|^2 + \lambda^4 e^{2\lambda(-R-z_0)^{-2}} |\mathcal{P}(-R) - \mathcal{P}^*(-R)|^2 \\
&\quad + \lambda^4 e^{2\lambda(R-z_0)^{-2}} |\mathcal{Q}(R) - \mathcal{Q}^*(R)|^2 + \lambda^4 e^{2\lambda(-R-z_0)^{-2}} |\mathcal{Q}(-R) - \mathcal{Q}^*(-R)|^2 \\
&\quad + \epsilon \|\mathbf{v}^*\|^2_{H^2(-R,R)^{|\mathbf{N}|}}.
\end{aligned} \tag{4.47}$$

Apply the inequality $(a+b)^2 \geq \frac{1}{2}a^2 - b^2$ for the first term of (4.47). We have

$$\begin{aligned}
&\frac{1}{2}\int_{-R}^{R} e^{2\lambda(z-z_0)^{-2}} \left|\mathbf{h}''(z)\right|^2 dz \\
&\quad + \lambda^4 e^{2\lambda(R-z_0)^{-2}} |\mathbf{h}(R)|^2 + \lambda^4 e^{2\lambda(-R-z_0)^{-2}} |\mathbf{h}(-R)|^2 \\
&\quad + \lambda^4 e^{2\lambda(R-z_0)^{-2}} |\mathbf{h}'(R)|^2 + \lambda^4 e^{2\lambda(-R-z_0)^{-2}} |\mathbf{h}'(-R)|^2 + \epsilon \|\mathbf{h}\|^2_{H^2(-R,R)^{|N|}} \\
&\quad \leq 2\int_{-R}^{R} e^{2\lambda(z-z_0)^{-2}} |\mathcal{S} :: \mathbf{h}|^2 dz - \int_{-R}^{R} e^{2\lambda(z-z_0)^{-2}} \left|\mathcal{F}(\mathbf{v}^{(k)}) - \mathcal{F}(\mathbf{v}^*)\right|^2 dz \\
&\quad + \lambda^4 e^{2\lambda(R-z_0)^{-2}} |\mathcal{P}(R) - \mathcal{P}^*(R))|^2 + \lambda^4 e^{2\lambda(-R-z_0)^{-2}} |\mathcal{P}(-R) - \mathcal{P}^*(-R)|^2 \\
&\quad + \lambda^4 e^{2\lambda(R-z_0)^{-2}} |\mathcal{Q}(R) - \mathcal{Q}^*(R)|^2 + \lambda^4 e^{2\lambda(-R-z_0)^{-2}} |\mathcal{Q}(-R) - \mathcal{Q}^*(-R)|^2 \\
&\quad + \epsilon \|\mathbf{v}^*\|^2_{H^2(-R,R)^{|\mathbf{N}|}}.
\end{aligned} \tag{4.48}$$

Since B_M is bounded in H, by the Sobolev embedding theorem in 1D, B_M is bounded in $C([-R,R])^{|\mathbf{N}|}$. We can find a number C depending only on M, $\mathcal{F}$ (and hence p, N, R, $[\mathbf{P}_\mathbf{m}]_{\mathbf{m}\leqq\mathbf{N}}$) such that

$$|\mathcal{F}(\mathbf{v}^{(k)}(z)) - \mathcal{F}(\mathbf{v}^*(z))| \leq C|\mathbf{v}^{(k)}(z) - \mathbf{v}^*(z)| \text{ for all } z \in (-R,R). \tag{4.49}$$

Combining (4.48) and (4.49), we can find a constant C depending only on M, p, N,

R, $[\mathbf{P_m}]_{\mathbf{m}\leqq\mathbf{N}}$ such that

$$\begin{aligned}
&\int_{-R}^{R} e^{2\lambda(z-z_0)^{-2}}|\mathbf{h}''(z)|^2dz \\
&\quad+\lambda^4 e^{2\lambda(R-z_0)^{-2}}|\mathbf{h}(R)|^2+\lambda^4 e^{2\lambda(-R-z_0)^{-2}}|\mathbf{h}(-R)|^2 \\
&\quad+\lambda^4 e^{2\lambda(R-z_0)^{-2}}|\mathbf{h}'(R)|^2+\lambda^4 e^{2\lambda(-R-z_0)^{-2}}|\mathbf{h}'(-R)|^2+\epsilon\|\mathbf{h}\|^2_{H^2(-R,R)^{|\mathbf{N}|}} \\
&\quad\leq C\left[\int_{-R}^{R} e^{2\lambda(z-z_0)^{-2}}|\mathbf{h}|^2dz+\int_{-R}^{R} e^{2\lambda(z-z_0)^{-2}}|\mathbf{v}^{(k)}-\mathbf{v}^*|^2dz\right. \\
&\quad+\lambda^4 e^{2\lambda(R-z_0)^{-2}}|\mathcal{P}(R)-\mathcal{P}^*(R))|^2+\lambda^4 e^{2\lambda(-R-z_0)^{-2}}|\mathcal{P}(-R)-\mathcal{P}^*(-R)|^2 \\
&\quad+\lambda^4 e^{2\lambda(R-z_0)^{-2}}|\mathcal{Q}(R)-\mathcal{Q}^*(R)|^2+\lambda^4 e^{2\lambda(-R-z_0)^{-2}}|\mathcal{Q}(-R)-\mathcal{Q}^*(-R)|^2 \\
&\quad\left.+\epsilon\|\mathbf{v}^*\|^2_{H^2(-R,R)^{|\mathbf{N}|}}\right].
\end{aligned}\tag{4.50}$$

Applying the Carleman estimate in Lemma 4.3.1 for each entry of $\mathbf{h}$, we have

$$\begin{aligned}
\int_{-R}^{R} e^{2\lambda(z-z_0)^{-2}}|\mathbf{h}''(z)|^2dz \geq\ & -Ce^{2\lambda(R-z_0)^{-2}}(\lambda^3|\mathbf{h}(R)|^2+\lambda|\mathbf{h}'(R)|^2) \\
& -Ce^{2\lambda(-R-z_0)^{-2}}(\lambda^3|\mathbf{h}(-R)|^2+\lambda|\mathbf{h}'(-R)|^2) \\
& +C\lambda^3\int_{-R}^{R} e^{2\lambda(z-z_0)^{-2}}|\mathbf{h}(z)|^2dz \\
& +C\lambda\int_{-R}^{R} e^{2\lambda(z-z_0)^{-2}}|\mathbf{h}'(z)|^2dz.
\end{aligned}\tag{4.51}$$

Combining (4.50) and (4.51) and noting that $\lambda^4 \gg \lambda^3$, we have

$$\begin{aligned}
&\lambda^3 \int_{-R}^{R} e^{2\lambda(z-z_0)^{-2}} |\mathbf{h}(z)|^2 dz + \lambda \int_{-R}^{R} e^{2\lambda(z-z_0)^{-2}} |\mathbf{h}'(z)|^2 dz \\
&\qquad + \lambda^4 e^{2\lambda(R-z_0)^{-2}} |\mathbf{h}(R)|^2 + \lambda^4 e^{2\lambda(-R-z_0)^{-2}} |\mathbf{h}(-R)|^2 \\
&\qquad + \lambda^4 e^{2\lambda(R-z_0)^{-2}} |\mathbf{h}'(R)|^2 + \lambda^4 e^{2\lambda(-R-z_0)^{-2}} |\mathbf{h}'(-R)|^2 \\
&\qquad \leq C \left[\int_{-R}^{R} e^{2\lambda(z-z_0)^{-2}} \left|\mathbf{h}\right|^2 dz + \int_{-R}^{R} e^{2\lambda(z-z_0)^{-2}} \left|\mathbf{v}^{(k)} - \mathbf{v}^*\right|^2 dz \right. \\
&\qquad + \lambda^4 e^{2\lambda(R-z_0)^{-2}} |\mathcal{P}(R) - \mathcal{P}^*(R))|^2 + \lambda^4 e^{2\lambda(-R-z_0)^{-2}} |\mathcal{P}(-R) - \mathcal{P}^*(-R)|^2 \\
&\qquad + \lambda^4 e^{2\lambda(R-z_0)^{-2}} |\mathcal{Q}(R) - \mathcal{Q}^*(R)|^2 + \lambda^4 e^{2\lambda(-R-z_0)^{-2}} |\mathcal{Q}(-R) - \mathcal{Q}^*(-R)|^2 \\
&\qquad \left. + \epsilon \|\mathbf{v}^*\|^2_{H^2(-R,R)^{|\mathbf{N}|}} \right].
\end{aligned} \tag{4.52}$$

It follows from (4.52) and the fact $\mathbf{h} = \mathbf{v}^{(k+1)} - \mathbf{v}^*$ that

$$\begin{aligned}
&\int_{-R}^{R} e^{2\lambda(z-z_0)^{-2}} |\mathbf{v}^{(k+1)} - \mathbf{v}^*|^2 dz \\
&\qquad \leq \frac{C}{\lambda^3} \Big[\int_{-R}^{R} e^{2\lambda(z-z_0)^{-2}} \left|\mathbf{v}^{(k)} - \mathbf{v}^*\right|^2 dz \\
&\qquad + \lambda^4 e^{2\lambda(R-z_0)^{-2}} |\mathcal{P}(R) - \mathcal{P}^*(R))|^2 + \lambda^4 e^{2\lambda(-R-z_0)^{-2}} |\mathcal{P}(-R) - \mathcal{P}^*(-R)|^2 \\
&\qquad + \lambda^4 e^{2\lambda(R-z_0)^{-2}} |\mathcal{Q}(R) - \mathcal{Q}^*(R)|^2 + \lambda^4 e^{2\lambda(-R-z_0)^{-2}} |\mathcal{Q}(-R) - \mathcal{Q}^*(-R)|^2 \\
&\qquad + \epsilon \|\mathbf{v}^*\|^2_{H^2(-R,R)^{|\mathbf{N}|}} \Big].
\end{aligned} \tag{4.53}$$

Recall once again that $\mathbf{h} = \mathbf{v}^{(k+1)} - \mathbf{v}^*$. Applying (4.53) when $k+1$ is replaced by k

and combining the resulting estimate with (4.53), we have

$$\begin{aligned}
&\int_{-R}^{R} e^{2\lambda(z-z_0)^{-2}}|\mathbf{v}^{(k+1)}-\mathbf{v}^*|^2dz\\
&\quad\le \frac{C}{\lambda^3}\Big[\frac{C}{\lambda^3}\Big[\int_{-R}^{R} e^{2\lambda(z-z_0)^{-2}}\big|\mathbf{v}^{(k-1)}-\mathbf{v}^*\big|^2dz\\
&\quad+\lambda^4e^{2\lambda(R-z_0)^{-2}}|\mathcal{P}(R)-\mathcal{P}^*(R))|^2+\lambda^4e^{2\lambda(-R-z_0)^{-2}}|\mathcal{P}(-R)-\mathcal{P}^*(-R)|^2\\
&\quad+\lambda^4e^{2\lambda(R-z_0)^{-2}}|\mathcal{Q}(R)-\mathcal{Q}^*(R)|^2+\lambda^4e^{2\lambda(-R-z_0)^{-2}}|\mathcal{Q}(-R)-\mathcal{Q}^*(-R)|^2\\
&\quad+\epsilon\|\mathbf{v}^*\|^2_{H^2(-R,R)^{|\mathbf{N}|}}\Big]\\
&\quad+\lambda^4e^{2\lambda(R-z_0)^{-2}}|\mathcal{P}(R)-\mathcal{P}^*(R))|^2+\lambda^4e^{2\lambda(-R-z_0)^{-2}}|\mathcal{P}(-R)-\mathcal{P}^*(-R)|^2\\
&\quad+\lambda^4e^{2\lambda(R-z_0)^{-2}}|\mathcal{Q}(R)-\mathcal{Q}^*(R)|^2+\lambda^4e^{2\lambda(-R-z_0)^{-2}}|\mathcal{Q}(-R)-\mathcal{Q}^*(-R)|^2\\
&\quad+\epsilon\|\mathbf{v}^*\|^2_{H^2(-R,R)^{|\mathbf{N}|}}\Big].
\end{aligned}$$

Continuing the procedure, we obtain

$$\begin{aligned}
\int_{-R}^{R} e^{2\lambda(z-z_0)^{-2}}|\mathbf{v}^{(k+1)}-\mathbf{v}^*|^2dz \le{}& \Big(\frac{C}{\lambda^3}\Big)^{k+1}\int_{-R}^{R} e^{2\lambda(z-z_0)^{-2}}\big|\mathbf{v}^{(0)}-\mathbf{v}^*\big|^2dz\\
&+\sum_{i=1}^{k}\Big(\frac{C}{\lambda^3}\Big)^{k}\Big[\lambda^4e^{2\lambda(R-z_0)^{-2}}|\mathcal{P}(R)-\mathcal{P}^*(R))|^2\\
&+\lambda^4e^{2\lambda(-R-z_0)^{-2}}|\mathcal{P}(-R)-\mathcal{P}^*(-R)|^2\\
&+\lambda^4e^{2\lambda(R-z_0)^{-2}}|\mathcal{Q}(R)-\mathcal{Q}^*(R)|^2\\
&+\lambda^4e^{2\lambda(-R-z_0)^{-2}}|\mathcal{Q}(-R)-\mathcal{Q}^*(-R)|^2\\
&+\epsilon\|\mathbf{v}^*\|^2_{H^2(-R,R)^{|\mathbf{N}|}}\Big].
\end{aligned}\tag{4.54}$$

Choose $\lambda > \lambda_1 > \lambda_0$ such that $C/\lambda^3 \in (0,1)$ for some λ_1 depending only on C and therefore only on M, p, N, R, and $[\mathbf{P}_{\mathbf{m}\leqq\mathbf{N}}]$. Estimate (4.42) is a direct consequence of (4.54). □

Remark 4.4.3. *Estimate* (4.42) *is interesting in the sense that when the data has noise, although the over-determined problem* (4.21) *might have no solution, we are still able to provide a reasonably accurate numerical solution. In fact, the sequence* $\{\mathbf{v}^{(k)}\}_{k\ge0}$ *is well-defined regardless whether or not* (4.21) *is solvable. This sequence is*

defined via minimizing a strictly convex cost functional as in (4.40) *when* $\mathbf{v}$ *is replaced by* $\mathbf{v}^{(k)}$, $k \geq 0$. *Given* (4.37) *and Theorem 4.4.1, estimate* (4.42) *implies that when* $\lambda > \lambda_1$, *we achieve the bound*

$$\|\mathbf{v}^{(k+1)} - \mathbf{v}^*\|_\lambda^2 \leq \Big(\frac{C}{\lambda^3}\Big)^{k+1}\|\mathbf{v}^{(0)} - \mathbf{v}^*\|_\lambda^2 + \frac{C/\lambda^3}{1 - C/\lambda^3}\Big[\lambda^4\big(e^{2\lambda(-R-z_0)^{-2}} + e^{2\lambda(R-z_0)^{-2}}\big)\delta^2 + \epsilon\|\mathbf{v}^*\|_{H^2(-R,R)^{|\mathbf{N}|}}^2\Big] \tag{4.55}$$

where C *is the constant in Theorem 4.4.1 and the norm* $\|\cdot\|_\lambda$ *is given by*

$$\|\varphi\|_\lambda = \Big[\int_{-R}^{R} e^{2\lambda(z-z_0)^{-2}}|\varphi|^2 dz\Big]^{1/2} \quad \textit{for all } \varphi \in L^2(-R,R).$$

In particular, fix $\lambda > \lambda_1$ *such that* $\theta = C/\lambda^3 \in (0,1)$. *In this "fixing* λ*" circumstance, the norm* $\|\cdot\|_\lambda$ *is equivalent to the standard norm in* $L^2(-R,R)$. *Hence, due to* (4.55), *we can find a constant* C_1 *depending only on* λ, z_0, *and* R *such that*

$$\|\mathbf{v}^{(k+1)} - \mathbf{v}^*\|_{L^2(-R,R)}^2 \leq C_1\Big[\theta^{k+1}\|\mathbf{v}^{(0)} - \mathbf{v}^*\|_{L^2(-R,R)}^2 + \delta^2 + \epsilon\|\mathbf{v}^*\|_{H^2(-R,R)^{|\mathbf{N}|}}^2\Big]. \tag{4.56}$$

Estimate (4.56) *guarantees the global convergence. Although* $\mathbf{v}^{(0)}$ *is not a good initial guess of* $\mathbf{v}^*$, *the approximating sequence converges to a numerical solution with the error* $O(\delta + \sqrt{\epsilon}\|\mathbf{v}^*\|_{H^2(-R,R)^{|\mathbf{N}|}})$.

Motivated from (4.9), define

$$v^{(k)}(\mathbf{x}', z, t) = \sum_{n_1=1}^{N_1}\cdots\sum_{n_{d-1}}^{N_{d-1}}\sum_{n_t=1}^{N_t} v_{(n_1,\ldots,n_{d-1},n_t)}(z)\Psi_{n_1}(x_1)\ldots\Psi_{n_{d-1}}(x_{d-1})\psi_{n_t}(t)$$

for all $(\mathbf{x}, t) = (\mathbf{x}', z, t) \in \Omega \times (0, T)$. Due to (4.7), set

$$c^{(k)}(\mathbf{x}) = \frac{v^{(k)}(\mathbf{x}, 0) - \Delta p(\mathbf{x})}{p(\mathbf{x})} \tag{4.57}$$

for all $\mathbf{x} \in \Omega$. By Remark 4.4.3 and Theorem 4.4.1, we can find λ_1 as in Theorem

4.4.1 such that for all $\lambda > \lambda_1$, we have

$$\begin{aligned} &\|c^{(k+1)} - c^*\|^2_{L^2(-R,R)} \\ &\qquad \le C_1\Big[\Big(\frac{C}{\lambda^3}\Big)^{k+1}\|\mathbf{v}^{(0)} - \mathbf{v}^*\|^2_{L^2(-R,R)} + \frac{\delta^2 C/\lambda^3}{1 - C/\lambda^3} + \epsilon\|\mathbf{v}^*\|^2_{H^2(-R,R)^{|\mathbf{N}|}}\Big] \end{aligned} \tag{4.58}$$

where C_1 is a constant depending only on λ, z_0, R, $\mathbf{N}$, and $[\mathbf{P_n}]_{\mathbf{n}\leqq\mathbf{N}}$. Here c^* is the true coefficient defined by

$$c^*(\mathbf{x}) = \frac{v^*(\mathbf{x}, 0) - \Delta p(\mathbf{x})}{p(\mathbf{x})}$$

for all $\mathbf{x} \in \Omega$.

The analysis above leads to Algorithm 1 to solve the inverse problem under consideration. Having the data f and g in hand, we can follow Algorithm 1 to compute a numerical solution to the inverse problem under consideration.

4.5 Numerical study

To illustrate our method, we numerically study the inverse problem, Problem 4.1.1, in 2D. That means, for simplicity, we set $d = 2$. Let $\Omega = (-R, R)^2$ and therefore $\Omega = (-R, R)$. Rather than using the notation $\mathbf{x}'$, we write x for an element of Ω'. In this section, we set $R = 1$.

4.5.1 The forward problem

To generate simulated data, we numerically compute the solution to (4.1). Since we only need the data on Γ, a part of $\partial\Omega$ and $t \in (0, T)$, it is not necessary to solve (4.1) on the whole unbounded domain $\mathbb{R}^d \times (0, \infty)$. Rather, we choose a domain $G = (-R_1, R_1)^2$ for some $R_1 > R$, in which Ω is compactly contained, and a positive number T. We solve

$$\begin{cases} u_t(\mathbf{x}, t) &= \Delta u(\mathbf{x}, t) + c(\mathbf{x})u(\mathbf{x}, t) \quad (\mathbf{x}, t) \in G \times (0, T), \\ u(\mathbf{x}, 0) &= p(\mathbf{x}) \qquad\qquad\qquad\qquad\quad \mathbf{x} \in G \end{cases} \tag{4.60}$$

Algorithm 1 The procedure to compute the numerical solution to (4.21)

1: Choose cut-off numbers $N_1, \dots, N_{d-1}$, and N_t. Set $\mathbf{N} = (N_1, N_2, \dots, N_{d-1}, N_t)$
2: Choose Carleman parameters z_0, and λ, and a regularization parameter ϵ. Choose a large number M.
3: Set $n = 0$. Choose an arbitrary initial solution $\mathbf{v}^{(0)} \in B_M$.
4: Compute $\mathbf{v}^{(k+1)} = \Phi^{(\lambda,\epsilon)}(\mathbf{v}^{(k)})$ where $\Phi^{(\lambda,\epsilon)}$ is defined in (4.40).
5: **if** $\|\mathbf{v}^{(k+1)} - \mathbf{v}^{(k)}\|_{L^2(-R,R)} > \kappa_0$ (for some fixed number $\kappa_0 > 0$) **then**
6: Replace k by $k + 1$.
7: Go back to Step 4.
8: **else**
9: Set the computed solution $\mathbf{v}^{\text{comp}} = \mathbf{v}_{(k+1)}$.
10: **end if**
11: Write $\mathbf{v}^{\text{comp}} = [v_{\mathbf{m}}^{(k+1)}]_{\mathbf{m} \leqq \mathbf{N}}$ and set the desired solution as in (4.21).
12: Due to (4.9), compute

$$\begin{aligned} v^{\text{comp}}(\mathbf{x}, t) &= v(\mathbf{x}', z, t) \\ &= \sum_{n_1=1}^{N_1} \cdots \sum_{n_{d-1}}^{N_{d-1}} \sum_{n_t=1}^{N_t} v^{\text{comp}}_{(n_1,\dots,n_{d-1},n_t)}(z) \Psi_{n_1}(x_1) \dots \Psi_{n_{d-1}}(x_{d-1}) \psi_{n_t}(t) \end{aligned}$$

for $\mathbf{x} \in \Omega$, $t \in (0, T)$.
13: By (4.7), we obtain the reconstructed coefficient c as

$$c^{\text{comp}}(\mathbf{x}) = \frac{v^{\text{comp}}(\mathbf{x}, 0) - \Delta p(\mathbf{x})}{p(\mathbf{x})} \tag{4.59}$$

for all $\mathbf{x} \in \Omega$.

by the explicit method in the finite difference scheme. More precisely, we discretize G by arranging a grid of points

$$\mathcal{G} = \left\{ \mathbf{x}_{i,j} = (x_i = -R_1 + (i-1)d_{\mathbf{x}}, z_j = -R_1 + (j-1)d_{\mathbf{x}}) : i, j = 1, \dots, N^1_{\mathbf{x}} \right\} \subset \overline{G}.$$

where $N^1_{\mathbf{x}}$ is an integer and $d_{\mathbf{x}} = 2R_1/(N^1_{\mathbf{x}} - 1)$. On the time domain, we arrange the partition of $[0, T]$ as

$$\mathcal{T} = \left\{ t_l = (l-1)d_t : l = 1, \dots, N_t \right\}$$

where N_t is an integer and $d_t = T/(N_t - 1)$. We set $R = 1$, $R_1 = 3$, $T = 0.5$, $N_{\mathbf{x}}^1 = 241$, and $N_t = 4001$. The finite difference version of (4.60) is read as

$$\begin{aligned}\frac{u(\mathbf{x}_{i,j}, t_{l+1}) - u(\mathbf{x}_{i,j}, t_l)}{d_t} \\ = \frac{u(\mathbf{x}_{i+1,j}, t_l) + u(\mathbf{x}_{i-1,j}, t_l) + u(\mathbf{x}_{i,j+1}, t_l) + u(\mathbf{x}_{i,j-1}, t_l) - 4u(\mathbf{x}_{i,j}, t_l)}{d_{\mathbf{x}}^2} \\ + c(\mathbf{x}_{i,j})u(\mathbf{x}_{i,j}, t_l)\end{aligned} \tag{4.61}$$

for all $\mathbf{x}_{i,j} \in \mathcal{G}$, $i, j \in \{1, \ldots, N_{\mathbf{x}}^1\}$, and $t_l \in \mathcal{T}$, $l \in \{1, \ldots, N_t\}$. It follows from (4.61) that

$$\begin{aligned}u(\mathbf{x}_{i,j}, t_{l+1}) = u(\mathbf{x}_{i,j}, t_l) \\ + d_t\Big[\frac{u(\mathbf{x}_{i+1,j}, t_l) + u(\mathbf{x}_{i-1,j}, t_l) + u(\mathbf{x}_{i,j+1}, t_l) + u(\mathbf{x}_{i,j-1}, t_l) - 4u(\mathbf{x}_{i,j}, t_l)}{d_{\mathbf{x}}^2} \\ + c(\mathbf{x}_{i,j})u(\mathbf{x}_{i,j}, t_l)\Big].\end{aligned} \tag{4.62}$$

So, given $u(\mathbf{x}_{i,j}, t_1) = p(\mathbf{x}_{i,j})$ for $i, j \in \{1, \ldots, N_{\mathbf{x}}^1\}$, we can compute $u(\mathbf{x}_{i,j}, t_2)$ via (4.62), and then continue get $u(\mathbf{x}_{i,j}, t_{N_t})$. In our computation, we set $p(\mathbf{x}) = 2$ for all $\mathbf{x} \in G$. We then easily extract the noiseless data f^* and g^* on Γ. We pretend not to know f^* and g^*. We only know the noisy version of f^* and g^* as

$$f = f^*(1 + \text{random numbers in } [-\delta, \delta]) \tag{4.63}$$

and

$$g = g^*(1 + \text{random numbers in } [-\delta, \delta]) \tag{4.64}$$

where δ is the noise level. In our computational program, we choose the initial function $u(\mathbf{x}, 0) = p(\mathbf{x}) = 2$, for all $\mathbf{x} \in \Omega$, $R_1 = 3$ and $T = 0.5$.

4.5.2 The implementation of Algorithm 1

Step 1 of Algorithm 1. In 2D, we only need to determine N_1 and N_t. These numbers are chosen by a data-driven procedure. Recall that the data is measured on Γ defined as in (4.2). The measurement set consists of two parts, namely $\Gamma = \Gamma^+ \cup \Gamma^-$ where

$$\Gamma^+ = \{\mathbf{x} = (x, z) : x \in (-R, R) \text{ and } z = R\}$$

and

$$\Gamma^- = \{\mathbf{x} = (x, z) : x \in (-R, R) \text{ and } z = -R\}.$$

One can examine the approximation formula

$$u(x, z, t) \simeq \sum_{n_1=1}^{N_1} \sum_{n_t=1}^{N_t} u_{(n_1,n_t)}(z) \mathbf{P}_{(n_1,n_t)}(x, t) \tag{4.65}$$

for the data $u(\mathbf{x}, t) = u(x, z, t) = f(\mathbf{x}, t)$ on either Γ^+ or Γ^-. Note that (4.65) is an analog of (4.9) where v is replaced by the function u. We do so on Γ^-. Define the mismatch function

$$\varphi_{(N_1,N_t)}(x, t) = \left| u(x, -R, t) - \sum_{n_1=1}^{N_1} \sum_{n_t=1}^{N_t} u_{(n_1,n_t)}(-R) \mathbf{P}_{(n_1,n_t)}(x, t) \right|$$

for $(x, t) \in \Gamma^- \times (0, T)$. Then, we test the smallness of $\varphi_{(N_1,N_t)}$ by manually and gradually increasing N_1 and N_t until $\varphi_{(N_1,N_t)}$ is sufficiently small. For example, we take the data in the numerical test 1 below. We increase those two numbers so that $\|\varphi_{(N_1,N_t)}\|_{L^\infty(\Gamma^- \times (0,T))} < 5 \times 10^{-4}$. By this, we find $N_1 = 15$ and $N_t = 10$. We chose these two numbers for all of our numerical tests. In Figure 4.1, we display the graphs of the function $\varphi_{(N_1,N_t)}$ for some values of N_1 and N_t.

Step 2 of Algorithm 1. In Step 2, we select the parameters through a trial-error procedure involving experimentation and adjustments. To do so, we begin with a reference test where the accurate solution is known. Using this reference, we adjust the parameters until Algorithm 1 produces a satisfactory numerical outcome with

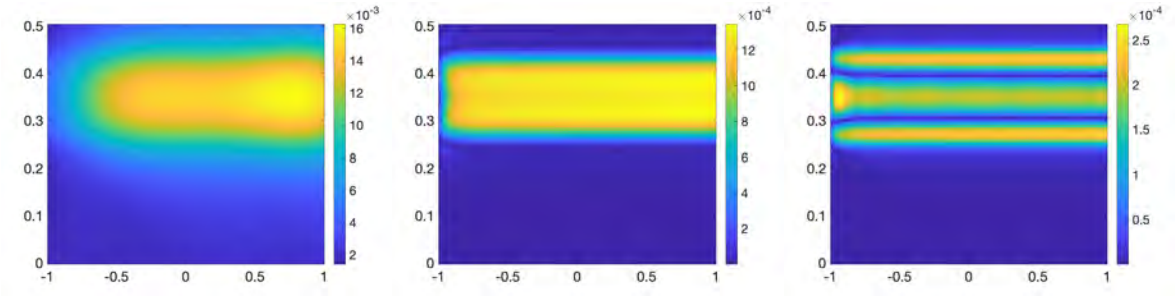

(a) $\varphi_{(5,5)}$ (b) $\varphi_{(15,8)}$ (c) $\varphi_{(15,10)}$

Figure 4.1: The difference $\varphi_{(N_1,N_t)}$ of the data $u(x,-R,t)$ and its truncated Fourier approximation $\sum_{n_1=1}^{N_1}\sum_{n_t=1}^{N_t} u_{(n_1,n_t)}(-R)\mathbf{P}_{(n_1,n_t)}(x,t)$, for some values of (N_1,N_t). The data is taken in Test 1 below. Evidently, for Step 1 in Algorithm 1 during the calculation of the desired coefficient in Test 1, we can choose $N_1 = 15$ and $N_t = 10$.

data free of noise, i.e., $\delta = 0$. These chosen parameters are then applied across all subsequent tests and various noise levels δ. The reference for our adjustments is Test 1, mentioned below. In all our numerical analyses, these values are set as $\epsilon = 10^{-6.5}$, $\kappa_0 = 10^{-3}$, $z_0 = -10$, and $\lambda = 10$.

Step 3 of Algorithm 1. We need to choose a function $\mathbf{v}^{(0)} \in H$. A convenient method to compute this function is solving the linear problem obtained by excluding the nonlinearity $\mathcal{F}$. More precisely, we solve the following problem

$$\begin{cases} \mathbf{v}^{(0)\prime\prime}(z) + \mathcal{S} :: \mathbf{v}^{(0)}(z) = 0 & z \in (-R,R), \\ \mathbf{v}^{(0)}(z) = \mathcal{P}(z) & z = \pm R, \\ \mathbf{v}^{(0)\prime}(z) = \mathcal{Q}(z) & z = \pm R \end{cases} \tag{4.66}$$

for the function $\mathbf{v}^{(0)}$. We can compute the numerical solution to (4.66) by the quasi-reversibility method. We do not present the numerical implementation to solve linear PDEs using the Carleman quasi-reversibility method. The reader can find the details about this in [57, 70, 75].

Step 4 of Algorithm 1. In Step 4, we minimize $J_{\mathbf{v}^{(k)}}$ and set $\mathbf{v}^{(k+1)}$ as its minimizer. The obtained minimizer $\mathbf{v}^{(k+1)}$ is actually the solution to

$$\begin{cases} \mathbf{v}^{(k+1)''}(z) + \mathcal{S} :: \mathbf{v}^{(k+1)}(z) + \mathcal{F}(\mathbf{v}^{(k)}(z)) = 0 & z \in (-R, R), \\ \mathbf{v}^{(k+1)}(z) = \mathcal{P}(z) & z = \pm R, \\ \mathbf{v}^{(k+1)'}(z) = \mathcal{Q}(z) & z = \pm R. \end{cases} \tag{4.67}$$

The details in implementation to compute the regularized solution $\mathbf{v}^{(k+1)}$ to (4.67) were presented in [57, 70, 75], in which we employ the optimization package already built in MATLAB. We do not repeat it here.

Steps 5–13. Executing these steps is direct and not complicated. For brevity, we do not present them here.

4.5.3 Numerical examples

We show in this section three (3) numerical examples computed by Algorithm 1. One can find that that reconstructed images are just acceptable, not perfect, since we only measure the data on $\Gamma \subset \partial\Omega$. For the case of full measurement resulting out of expectation numerical results, we refer the reader to [70, 75].

Test 1. In test 1, the true coefficient c is given by

$$c^{\text{true}}(x, z) = \begin{cases} e^{\frac{0.35x^2 + (z-0.4)^2}{0.55^2 - (0.35x^2 + (z-0.4)^2)}} & 0.35x^2 + (z-0.4)^2 < 0.55^2, \\ 0 & \text{otherwise.} \end{cases}$$

for $(x, z) \in \Omega$. It is characterized by an "ellipse" inclusion. The true and computed coefficient c are displayed in Figure 4.2.

It is evident that Algorithm 1 generates a satisfactory numerical solution. It is evident that the "ellipse inclusion" was successfully detected. The maximum value of the function c inside the inclusion is 1. The constructed value is 0.952 (relative error 4.8%). Due to Figure 4.2c, the stopping criterion of Algorithm 1 is met after only seven iterations.

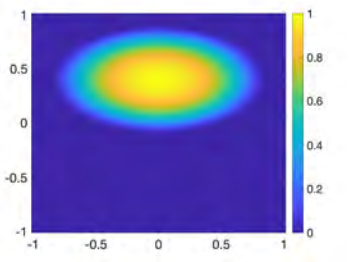

(a) The true coefficient c^{true}

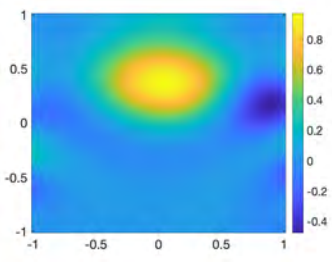

(b) The computed coefficient c^{comp}

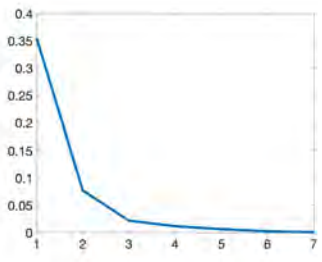

(c) The consecutive relative error $\frac{\|\mathbf{v}^{(k)} - \mathbf{v}^{(k-1)}\|_{L^\infty}}{\|\mathbf{v}^{(k)}\|_{L^\infty}}$.

Figure 4.2: (a) The true coefficient, (b) the computed one from data on Γ corrupted with 5% of noise, and (c) the relative difference of the reconstructed of the solution $\mathbf{v}$ to (4.21) at the k^{th} iteration, $k = 1, \ldots, 7$. Although the data are missing in $\partial\Omega \backslash \Gamma$, the reconstruction is acceptable. The convergence of our method is numerically confirmed.

Test 2. We test the case when the true coefficient is characterized by two horizontal inclusions. More precisely, we set

$$c^{\text{true}}(x,z) = \begin{cases} 1 & \max\{0.25|x|, 4|z-0.6|\} < 0.8, \\ 1 & \max\{0.25|x|, 4|z+0.6|\} < 0.8, \\ 0 & \text{otherwise}, \end{cases} \qquad \text{for all } (x,z) \in \Omega.$$

The true and computed solutions to Problem 4.1.1 are shown in Figure 4.3

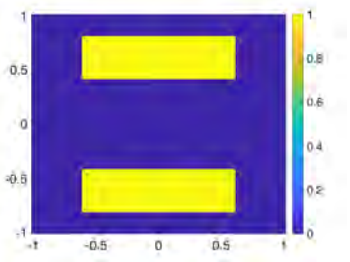

(a) The true coefficient c^{true}

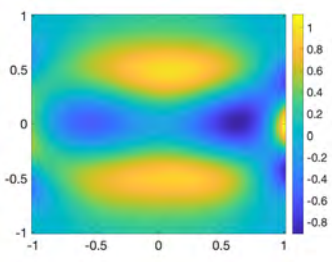

(b) The computed coefficient c^{comp}

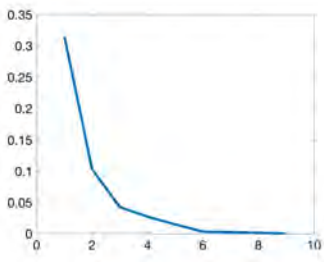

(c) The consecutive relative error $\frac{\|\mathbf{v}^{(k)} - \mathbf{v}^{(k-1)}\|_{L^\infty}}{\|\mathbf{v}^{(k)}\|_{L^\infty}}$.

Figure 4.3: (a) The true coefficient, (b) the computed one from data on Γ corrupted with 5% of noise, and (c) the relative difference of the reconstructed of the solution $\mathbf{v}$ to (4.21) at the k^{th} iteration, $k = 1, \ldots, 9$. Despite the absence of data in $\partial\Omega \setminus \Gamma$, the reconstruction remains satisfactory. Our method's fast convergence has been verified numerically.

As in Test 1, we can see that Algorithm 1 provides a satisfactory numerical solu-

tion. It is evident that both horizontal inclusions were successfully identified. The maximum value of the function c inside each inclusion is 1. The constructed value of c inside the upper inclusion is 0.963 (relative error 3.7%), and the one inside the lower inclusion is 0.875 (relative error 12.4%). Due to Figure 4.3c, Algorithm 1 stops at only nine iterations.

Test 3. Test 3 checks the case when the true coefficient c has a T inclusion. That means the function c^{true} takes the value 1 inside a letter T and 0 otherwise. We refer the reader to Figure 4.4 for the image of the true and computed coefficients.

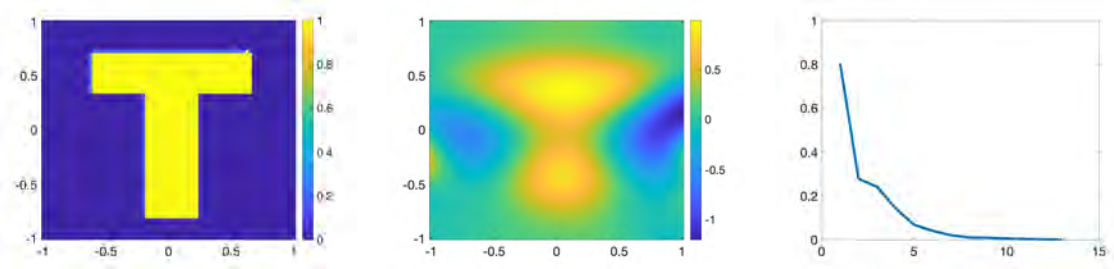

(a) The true coefficient c^{true} (b) The computed coefficient c^{comp} (c) The consecutive relative error $\frac{\|\mathbf{v}^{(k)} - \mathbf{v}^{(k-1)}\|_{L^\infty}}{\|\mathbf{v}^{(k)}\|_{L^\infty}}$.

Figure 4.4: (a) The true coefficient, (b) the computed one from data on Γ corrupted with 5% of noise, and (c) the relative difference of the reconstructed of the solution $\mathbf{v}$ to (4.21) at the k^{th} iteration, $k = 1, \ldots, 13$. Despite the absence of data in $\partial\Omega \setminus \Gamma$, the reconstruction of the letter T is acceptable. Our method's fast convergence has been verified numerically.

As in Test 1 and Test 2, we can see that the T inclusion was successfully found. The maximum value of the function c inside each inclusion is 1. The constructed value of c inside the inclusion is 0.98 (relative error 2%). Due to Figure 4.4c, Algorithm 1 stops at only 13 iterations.

Remark 4.5.1. *The computational cost of Algorithm 1 is not expensive. In fact, we only need to solve several 1D linear over-determined problems in Steps 5-7. We have used a personal computer iMac with a 3.2GHz Intel Core i5 Processor and memory of 24GB, not a professional workstation, to compute the numerical solutions above.*

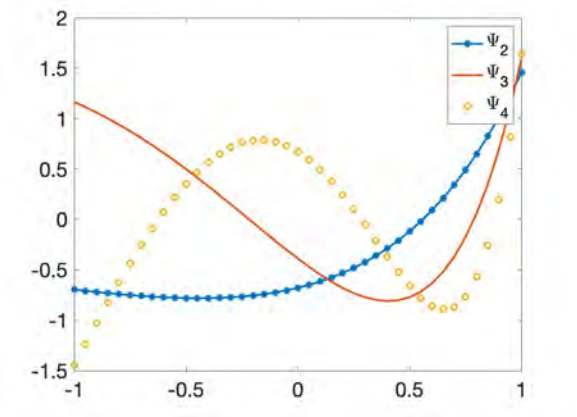

Figure 4.5: Graphs of the basis functions Ψ_2, Ψ_3, and Ψ_4.

It took 46.93, 56.56, and 77.12 seconds to complete all computational tasks for the inverse problem in Test 1, Test 2, and Test 3, respectively.

Remark 4.5.2. *It is worth mentioning that the images of the inclusions in the tests above are not perfect. The numerical results show some artifacts. In particular, readers may notice that the artifacts on the right side of the reconstruction in Figures 4.2b–4.4b are more pronounced than those on the left. This is primarily due to the non-symmetric nature of the basis set* $\{\Psi_{n_1}\}_{n_1\geq 1}$ *used in the computations. Figure 4.5 shows the graphs of three functions,* Ψ_2, Ψ_3, *and* Ψ_4, *where it is visually apparent that these functions oscillate more on the right side and appear more stable on the left. Consequently, the reconstruction on the right is likely more sensitive to noise. However, these errors are acceptable because we solve the inverse problem when the data are given only on the part* Γ *of* $\partial\Omega$.

4.6 Concluding remarks

In this study, we provide a numerical method to solve a nonlinear coefficient inverse problem for parabolic equations. This inverse problem has numerous practical applications. To obtain these solutions, we employ the polynomial-exponential basis, converting the inverse problem into a set of 1D nonlinear equations. Next, we introduce a method to address this nonlinear system. Our method is based on a

combination of the Picard iteration, the quasi-reversibility method, and a Carleman estimate. We provide analytic proof of the method's convergence and demonstrate its effectiveness through some numerical examples.

REFERENCES

[1] A. Abhishek, T. T. Le, L. H. Nguyen, and T. Khan. The Carleman-Newton method to globally reconstruct the initial condition for nonlinear parabolic equations. *Journal of Computational and Applied Mathematics*, 445:115827, 2024.

[2] R. Abney. Nonpropagating excitations in 2-D. Master's thesis, University of North Carolina at Charlotte, Charlotte, NC, May 2020.

[3] R. Abney and G. Gbur. Nonradiating orbital motions. *Physical Review A*, 107(5), May 19 2023.

[4] R. Abney, T. T. Le, L. H. Nguyen, and C. Peters. A Carleman-Picard approach for reconstructing zero-order coefficients in parabolic equations with limited data. *Applied Mathematics and Computation*, 494:129286, 2025.

[5] A. Alù and N. Engheta. Achieving transparency with plasmonic and metamaterial coatings. *Physical Review E*, 72(1):016623, 2005.

[6] A. B. Bakushinskii, M. V. Klibanov, and N. A. Koshev. Carleman weight functions for a globally convergent numerical method for ill-posed Cauchy problems for some quasilinear PDEs. *Nonlinear Anal. Real World Appl.*, 34:201–224, 2017.

[7] E. Bécache, L. Bourgeois, L. Franceschini, and J. Dardé. Application of mixed formulations of quasi-reversibility to solve ill-posed problems for heat and wave equations: The 1d case. *Inverse Problems & Imaging*, 9(4):971–1002, 2015.

[8] L. Beilina and M. V. Klibanov. *Approximate Global Convergence and Adaptivity for Coefficient Inverse Problems*. Springer, New York, 2012.

[9] Norman Bleistein and Jack K. Cohen. Nonuniqueness in the inverse source problem in acoustics and electromagnetics. *Journal of Mathematical Physics*, 18(194):194–201, February 1977.

[10] D. Bohm and M. Weinstein. The self-oscillations of a charged particle. *Physical Review*, 74(12):1789–1798, December 1948.

[11] L. Borcea, V. Druskin, A. V. Mamonov, and M. Zaslavsky. A model reduction approach to numerical inversion for a parabolic partial differential equation. *Inverse Problems*, 30:125011, 2014.

[12] L. Bourgeois. Convergence rates for the quasi-reversibility method to solve the Cauchy problem for Laplace's equation. *Inverse Problems*, 22:413–430, 2006.

[13] L. Bourgeois and J. Dardé. A duality-based method of quasi-reversibility to solve the Cauchy problem in the presence of noisy data. *Inverse Problems*, 26:095016, 2010.

[14] L. Bourgeois, D. Ponomarev, and J. Dardé. An inverse obstacle problem for the wave equation in a finite time domain. *Inverse Probl. Imaging*, 13(2):377–400, 2019.

[15] A. L. Bukhgeim and M. V. Klibanov. Uniqueness in the large of a class of multidimensional inverse problems. *Soviet Math. Doklady*, 17:244–247, 1981.

[16] K. Cao and D. Lesnic. Determination of space-dependent coefficients from temperature measurements using the conjugate gradient method. *Numer Methods Partial Differential Eq.*, 34:1370–1400, 2018.

[17] K. Cao and D. Lesnic. Simultaneous reconstruction of the perfusion coefficient and initial temperature from time-average integral temperature measurements. *Applied Mathematical Modelling*, 68:523–539, 2019.

[18] C. Clason and M. V. Klibanov. The quasi-reversibility method for thermoacoustic tomography in a heterogeneous medium. *SIAM J. Sci. Comput.*, 30:1–23, 2007.

[19] S. A. Cummer and D. Schurig. One path to acoustic cloaking. *New Journal of Physics*, 9(3):45, 2007.

[20] J. Dardé. Iterated quasi-reversibility method applied to elliptic and parabolic data completion problems. *Inverse Problems and Imaging*, 10:379–407, 2016.

[21] A. J. Devaney. Nonuniqueness in the inverse scattering problem. *Journal of Mathematical Physics*, 19(7):1526–1531, 1978.

[22] A J Devaney and E Wolf. Radiating and nonradiating classical current distributions and the fields they generate. *Physical Review*, 8(4):1044–1047, August 1973.

[23] P. Ehrenfest. Asymmetric power movement without magnet or radiation fields. *Physikalische Zeitschrift*, 11:708–709, 1910.

[24] V. A. Fedotov, A. V. Rogacheva, V. Savinov, D. P. Tsai, and N. I. Zheludev. Resonant transparency and non-trivial non-radiating excitations in toroidal metamaterials. *Scientific Reports*, 3, October 17 2013.

[25] F. G. Friedlander. An inverse problem for radiation fields. *Proceedings of the London Mathematical Society*, 27(3):551–576, 1973.

[26] A. Gamliel, K. Kim, A. I. Nachman, and E. Wolf. A new method for specifying nonradiating, monochromatic scalar sources and their fields. *Journal of the Optical Society of America A*, 6(9):1388–1393, September 1989.

[27] G. Gbur. *Nonradiating Sources and the Inverse Source Problem*. PhD thesis, University of Rochester, 2001.

[28] G. Gbur. Invisibility physics: Past, present, and future. In E. Wolf, editor, *Progress in Optics*, volume 58 of *Progress in Optics*, pages 65–114. Elsevier, 2013.

[29] G. Gbur. Designing directional cloaks form localized fields. *Optics Letters*, 40(6):986–989, March 2015.

[30] G. Gbur. Visions of invisibility in optics: retrospective. *J. Opt. Soc. Am. A Opt. Image Sci. Vis.*, 41(3):435–443, 2024.

[31] G. H. Goedecke. Classically radiationless motions and possible implications for quantum theory. *Physical Review*, 135(1B):B281–B288, July 1964.

[32] A. Greenleaf, M. Lassas, and G. Uhlmann. On nonuniqueness for Calderón's inverse problem. *Communications in Mathematical Physics*, 247(3):543–572, 2003.

[33] F. Guevara Vasquez, G. W. Milton, and D. Onofrei. Active exterior cloaking for the 2d laplace and helmholtz equations. *Physical Review Letters*, 103(7):073901, 2009.

[34] J. Hadamard. Sur les problèmes aux dérivés partielles et leur signification physique. *Princeton University Bulletin*, 13:49–52, 1902.

[35] D. N. Hào, T. T. Le, and L. H. Nguyen. The Fourier-based dimensional reduction method for solving a nonlinear inverse heat conduction problem with limited boundary data. *Communications in Nonlinear Science and Numerical Simulation*, 128:107679, 2024.

[36] C. M. Ho and R. J. Scherrer. Anapole dark matter. *Physics Letters B*, 722(4-5):341–346, May 24 2013.

[37] V. Isakov. Some inverse problems for the diffusion equation. *Inverse Problems*, 15(1):3–10, 1999.

[38] M. Kaku. *Physics of the Impossible: A Scientific Exploration into the World of Phasers, Force Fields, Teleportation, and Time Travel*. Anchor Books, 2008.

[39] B. Kaltenbacher and W. Rundell. Regularization of a backwards parabolic equation by fractional operators. *Inverse Probl. Imaging*, 13(2):401–430, 2019.

[40] M. Kerker. Invisible bodies. *Journal of the Optical Society of America*, 65(4):376–379, April 1975.

[41] Y. L. Keung and J. Zou. Numerical identifications of parameters in parabolic systems. *Inverse Problems*, 14:83–100, 1998.

[42] V. A. Khoa, G. W. Bidney, M. V. Klibanov, L. H. Nguyen, L. Nguyen, A. Sullivan, and V. N. Astratov. Convexification and experimental data for a 3D inverse scattering problem with the moving point source. *Inverse Problems*, 36:085007, 2020.

[43] V. A. Khoa, G. W. Bidney, M. V. Klibanov, L. H. Nguyen, L. Nguyen, A. Sullivan, and V. N. Astratov. An inverse problem of a simultaneous reconstruction of the dielectric constant and conductivity from experimental backscattering data. *Inverse Problems in Science and Engineering*, 29(5):712–735, 2021.

[44] V. A. Khoa, M. V. Klibanov, and L. H. Nguyen. Convexification for a 3D inverse scattering problem with the moving point source. *SIAM J. Imaging Sci.*, 13(2):871–904, 2020.

[45] M. V. Klibanov. Carleman estimates for global uniqueness, stability and numerical methods for coefficient inverse problems. *J. Inverse and Ill-Posed Problems*, 21:477–560, 2013.

[46] M. V. Klibanov. Carleman estimates for the regularization of ill-posed Cauchy problems. *Applied Numerical Mathematics*, 94:46–74, 2015.

[47] M. V. Klibanov. Carleman weight functions for solving ill-posed Cauchy problems for quasilinear PDEs. *Inverse Problems*, 31:125007, 2015.

[48] M. V. Klibanov. Convexification of restricted Dirichlet to Neumann map. *J. Inverse and Ill-Posed Problems*, 25(5):669–685, 2017.

[49] M. V. Klibanov and O. V. Ioussoupova. Uniform strict convexity of a cost functional for three-dimensional inverse scattering problem. *SIAM J. Math. Anal.*, 26:147–179, 1995.

[50] M. V. Klibanov, L. H. Nguyen, and H. V. Tran. Numerical viscosity solutions to Hamilton-Jacobi equations via a Carleman estimate and the convexification method. *Journal of Computational Physics*, 451:110828, 2022.

[51] M. V. Klibanov and F. Santosa. A computational quasi-reversibility method for Cauchy problems for Laplace's equation. *SIAM J. Appl. Math.*, 51:1653–1675, 1991.

[52] M. V. Klibanov and A. G. Yagola. Convergent numerical methods for parabolic equations with reversed time via a new Carleman estimate. *preprint*, 2019.

[53] R. Lattès and J. L. Lions. *The Method of Quasireversibility: Applications to Partial Differential Equations.* Elsevier, New York, 1969.

[54] P. N. H. Le, T. T. Le, and L. H. Nguyen. The Carleman convexification method for Hamilton-Jacobi equations. *Computers and Mathematics with Applications*, 159:173–185, 2024.

[55] T. T. Le. Global reconstruction of initial conditions of nonlinear parabolic equations via the Carleman-contraction method. In D-L. Nguyen, L. H. Nguyen, and T-P. Nguyen, editors, *Advances in Inverse problems for Partial Differential Equations*, volume 784 of *Contemporary Mathematics*, pages 23–42. American Mathematical Society, 2023.

[56] T. T. Le, V. A. Khoa, M. V. Klibanov, L. H. Nguyen, G. W. Bidney, and V. N. Astratov. Numerical verification of the convexification method for a frequency-dependent inverse scattering problem with experimental data. *Journal of Applied and Industrial Mathematics*, 17:908–927, 2023.

[57] T. T. Le and L. H. Nguyen. A convergent numerical method to recover the initial condition of nonlinear parabolic equations from lateral Cauchy data. *Journal of Inverse and Ill-posed Problems*, 30(2):265–286, 2022.

[58] T. T. Le and L. H. Nguyen. The gradient descent method for the convexification to solve boundary value problems of quasi-linear PDEs and a coefficient inverse problem. *Journal of Scientific Computing*, 91(3):74, 2022.

[59] T. T. Le, L. H. Nguyen, T-P. Nguyen, and W. Powell. The quasi-reversibility method to numerically solve an inverse source problem for hyperbolic equations. *Journal of Scientific Computing*, 87:90, 2021.

[60] T. T. Le, L. H. Nguyen, and H. V. Tran. A Carleman-based numerical method for quasilinear elliptic equations with over-determined boundary data and applications. *Computers and Mathematics with Applications*, 125:13–24, 2022.

[61] Q. Li and L. H. Nguyen. Recovering the initial condition of parabolic equations from lateral Cauchy data via the quasi-reversibility method. *Inverse Problems in Science and Engineering*, 28:580–598, 2020.

[62] E. A. Marengo and R. W. Ziolkowski. On the radiating and nonradiating components of scalar, electromagnetic, and weak gravitational sources. *Physical Review Letters*, 83(17):3345–3349, October 25 1999.

[63] D. A. B. Miller. On perfect cloaking. *Optics Express*, 14(25):12457–12466, 2006.

[64] A. E. Miroshnichenko, A. B. Evlyukhin, Y. F. Yu, R. M. Bakker, A. Chipouline, A. I. Kuznetsov, B. Luk'yanchuk, B. N. Chichkov, and Y. S. Kivshar. Nonradiating anapole modes in dielectric nanoparticles. *Nature Communications*, 6, August 2015.

[65] F. Monticone and A. Alù. Invisibility exposed: Physical bounds on passive cloaking. *Optica*, 3(7):718–724, 2013.

[66] Dylan Moses, Choon How Gan, and Greg Gbur. Directional, nonpropagating, and polychromatic excitations in one-dimensional wave systems. *Physical Review E*, 79(2):026606, February 2009.

[67] H. M. Nguyen and L. H. Nguyen. Cloaking using complementary media for the Helmholtz equation and a three spheres inequality for second order elliptic equations. *Transaction of the American Mathematical Society*, 2:93–112, 2015.

[68] H. T. Nguyen, V. A. Khoa, and V. A. Vo. Analysis of a quasi-reversibility method for a terminal value quasi-linear parabolic problem with measurements. *SIAM Journal on Mathematical Analysis*, 51:60–85, 2019.

[69] L. H. Nguyen. An inverse space-dependent source problem for hyperbolic equations and the Lipschitz-like convergence of the quasi-reversibility method. *Inverse Problems*, 35:035007, 2019.

[70] L. H. Nguyen. A new algorithm to determine the creation or depletion term of parabolic equations from boundary measurements. *Computers and Mathematics with Applications*, 80:2135–2149, 2020.

[71] L. H. Nguyen. The Carleman contraction mapping method for quasilinear elliptic equations with over-determined boundary data. *Acta Mathematica Vietnamica*, 48:401–422, 2023.

[72] L. H. Nguyen and M. V. Klibanov. Carleman estimates and the contraction principle for an inverse source problem for nonlinear hyperbolic equations. *Inverse Problems*, 38:035009, 2022.

[73] L. H. Nguyen, Q. Li, and M. V. Klibanov. A convergent numerical method for a multi-frequency inverse source problem in inhomogenous media. *Inverse Problems and Imaging*, 13:1067–1094, 2019.

[74] P. M. Nguyen, T. T. Le, L. H. Nguyen, and M. V. Klibanov. Numerical differentiation by the polynomial-exponential basis. *Journal of Applied and Industrial Mathematics*, 17:928–942, 2023.

[75] P. M. Nguyen and L. H. Nguyen. A numerical method for an inverse source problem for parabolic equations and its application to a coefficient inverse problem. *Journal of Inverse and Ill-posed Problems*, 38:232–339, 2020.

[76] A. N. Norris. Acoustic cloaking. *Journal of the Acoustical Society of America*, 130(3):1664–1673, 2011.

[77] J. B. Pendry, D. Schurig, and D. R. Smith. Controlling electromagnetic fields. *Science*, 312(5781):1780–1782, 2006.

[78] A. I. Prilepko and A. B. Kostin. On certain inverse problems for parabolic equations with final and integral observation. *Russ. Acad. Sci. Sb. Math.*, 75:473–490, 1993.

[79] A. I. Prilepko, D. G. Orlovsky, and I. A. Vasin. *Methods for solving inverse problems in mathematical physics*, volume 321. Pure and Applied Mathematics, Marcel Dekker, New York, 2000.

[80] G. A. Schott. The electromagnetic field of a moving uniformly and rigidly electrified sphere and its radiationless orbits. *Philosophical Magazine*, 15(100):752–761, April 1933.

[81] G. A. Schott. The electromagnetic field due to a uniformly and rigidly electrified sphere in spinless accelerated motion and its mechanical reaction on the sphere, i. *Proceedings of the Royal Society of London. Series A, Mathematical and physical sciences*, 156(889):471–486, 1936.

[82] G. A. Schott. On the spinless rectilinear motion of a uniformly and rigidly electrified sphere, ii. *Proceedings of the Royal Society of London. Series A, Mathematical and physical sciences*, 156(889):487–503, 1936.

[83] G. A. Schott. The general motion of a spinning uniformly and rigidly electrifield sphere, iii. *Proceedings of the Royal Society of London. Series A, Mathematical and physical sciences*, 159(899):548–570, 1937.

[84] G. A. Schott. The uniform circular motion with invariable normal spin of a rigidly and uniformly electrified sphere, iv. *Proceedings of the Royal Society of London. Series A, Mathematical and physical sciences*, 159(899):570–591, 1937.

[85] A. V. Smirnov, M. V. Klibanov, and L. H. Nguyen. On an inverse source problem for the full radiative transfer equation with incomplete data. *SIAM Journal on Scientific Computing*, 41:B929–B952, 2019.

[86] A. N. Tikhonov. On the stability of inverse problems. *Proceedings of the USSR Academy of Sciences*, 39:195–198, 1943.

[87] N. H. Tuan, V. V. Au, V. A. Khoa, and D. Lesnic. Identification of the population density of a species model with nonlocal diffusion and nonlinear reaction. *Inverse Problems*, 33:055019, 2017.

[88] E. Wolf and T. Habashy. Invisible bodies and the uniqueness of the inverse scattering problem. *Journal of Modern Optics*, 40(5):785–792, 1993.

[89] L. Yang, J-N. Yu, and Y-C. Deng. An inverse problem of identifying the coefficient of parabolic equation. *Applied Mathematical Modelling*, 32:1984–1995, 2008.

[90] S. Zhang, D. A. Genov, C. Sun, and X. Zhang. Cloaking of matter waves. *Physical Review Letters*, 100(12):123002, 2008.